Università degli Studi di Firenze

Dipartimento di Chimica

Dottorato di Ricerca in Scienze Chimiche

XXIII Ciclo

CHIM/02 – Chimica Fisica

Magnetoliposomes for controlled drug release

Magnetoliposomi per il rilascio controllato di farmaci

Ph.D. Thesis by

Silvia Nappini

Tutor *Coordinator*

Prof. Piero Baglioni Prof. Andrea Goti

A chi ha creduto in me

"La teoria è quando si sa tutto ma non funziona niente. La pratica è quando funziona tutto ma non si sa il perché. In ogni caso si finisce sempre a coniugare la teoria con la pratica: non funziona niente e non si sa il perché."

Albert Einstein

Index

1 - Introduction

This thesis is the result of a work that has the purpose of employing innovative transport vectors for drug delivery based on "*magnetoliposomes"*, which are liposomes loaded with magnetic nanoparticles.

Since their discovery[1], lipid vesicles have attracted growing interest for their potential application as nanometer-scaled drug delivery vectors[2-5]. The interest is mainly related to their biocompatibility, their flexibility in composition and size, and their ability to encapsulate both hydrophilic and hydrophobic molecules into the aqueous pool[6] or in the lipid bilayer[7], respectively.

Magnetic nanoparticles can be efficiently encapsulated in lipid vesicles and used for targeting drugs to a specific location, i.e. diseased cells, using an external magnetic force[8,9].

The leakage of the embedded drug can be activated through destabilization of the carrier system by an *external stimulus;* in this case the presence of magnetic nanoparticles in the aqueous pool or in the lipid bilayer of magnetoliposomes allows to enhance the drug leakage by applying an alternating magnetic field (AMF)[9]. In this work a low frequency alternating magnetic field (LF-AMF), 0.1-6 kHz, was applied to study drug release from magnetic vesicles in order to minimize the hyperthermic contribution and investigate only the field effect. Detailed information about the magnetic drug-carrier systems, prepared and studied in this work, is given in paragraph 1.4, where the aim of the project is deeply discussed after a brief introduction to Nanotechnology.

A general description about the syntheses and the characterization methods of magnetoliposomes is reported in Chapter 2 (Methods), while the magnetic vesicle preparation and their release behaviour have been widely discussed in Chapters 3 and 4, respectively.
Considering that "*drug delivery*" is one of the most promising applications of "*Nanotechnology*" in medicine, a general introduction about the main applications of "*nanomedicine*" is given in the following paragraphs. Moreover the properties of lipid vesicles and magnetic nanoparticles were discussed in order to understand magnetoliposome behaviour and their drug release properties.

1.1 Nanotechnology

Although Nanotechnology is a relatively recent field in scientific research, the development of its central concepts happened over a longer period of time. The first use of the term "Nanotechnolgy" was in "*There's Plenty of Room at the Bottom*" a talk given by physicist Richard Feynman at an American Physical Society meeting in 1959: "The principles of physics, as far as I can see, do not speak against the possibility of manoeuvring things atom by atom". Feynman described the possibility of manipulating individual atoms and molecules, using one set of precise tools to build and operate another proportionally smaller set, and so on down to the needed scale. In the course of this, he noted, scaling issues would arise from the changing magnitude of various physical phenomena: gravity would become less important, surface tension and van der Waals attraction would become increasingly more significant, etc. In the 1980s the basic idea of this definition was explored in much more depth by Dr. K. Eric Drexler, who promoted the technological significance of nano-scale phenomena and devices through speeches and the books *Engines of Creation: The Coming Era of Nanotechnology (1986)* and *Nanosystems:*

Molecular Machinery, Manufacturing, and Computation (1991). Dexter expanded the term nanotechnology giving it a more practical and applicative sense, indicating nanotechnology as a broad range of science and technology working at the length scale of approximately 1 to 100 nanometers, including the more specific goal it originally denoted (Figure 1.1). Nanotechnology and nanoscience got started in the early 1980s with two major developments: the birth of cluster science and the invention of the scanning tunneling microscope (STM). This development led to the discovery of fullerenes in 1985 and carbon nanotubes a few years later. In another development, the synthesis and properties of semiconductor nanocrystals were studied; this led to a fast increasing number of metal and metal oxide nanoparticles and quantum dots.

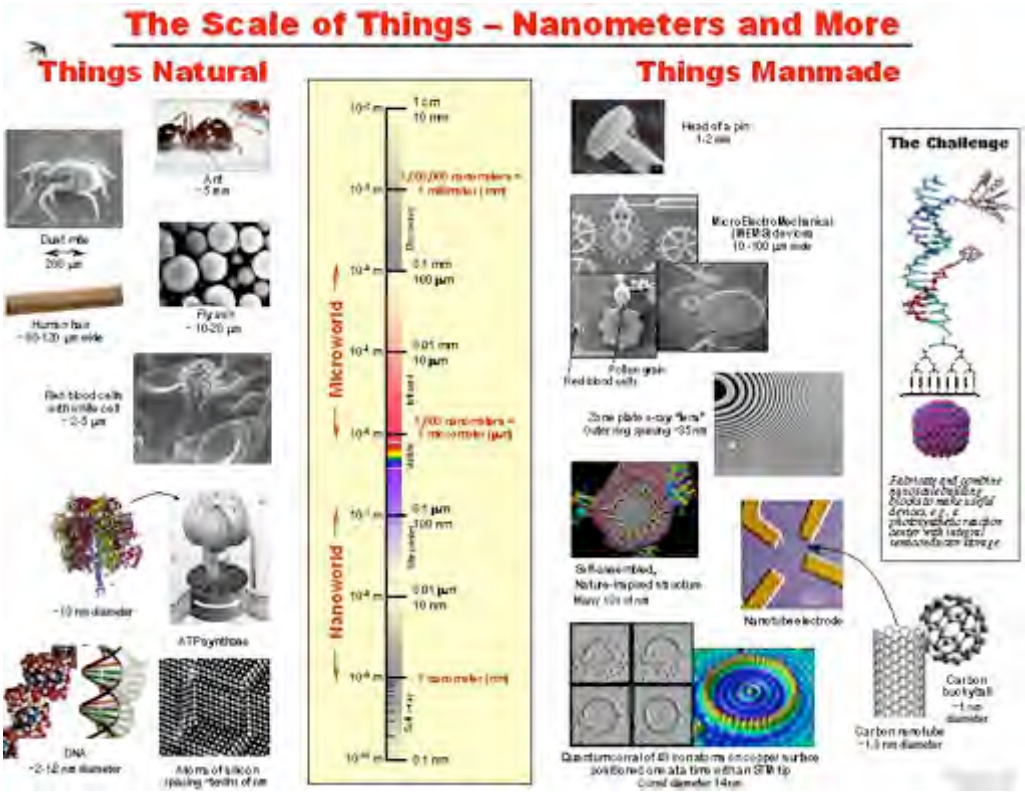

Figure 1.1 The Nanometer Scale: the size comparison of nanoparticles with biological objects

Generally Nanotechnology deals with structures sized between 1 and 100 nm, also are sometimes included materials smaller than 1 μm. Current nanotechnology progresses in chemistry, physics, materials science and biotechnology have created novel materials that have unique properties because their structures are determined on the nanometer scale. Some of these materials have already found their ways into consumer products, such as sun-screen, bathroom or windows cleaner and stain-resistant paints. Others are being intensively researched for solutions to humanity's greatest problems, i.e. diseases, clean energy, clean water, land and air etc.

Other works are aimed by the desire to develop nano-electronic devices and computer chips capable to store a large amount of information in smaller and smaller space.

The products of advanced nanotechnology that will become available in coming decades promise even more revolutionary applications than the products of current and near-term nanotechnology.

Nanotechnology has also found important applications in the area of healthcare and disease diagnosis and treatment, giving rise to the specific branch of Nanomedicine.

1.1.1 Nanomedicine

Nanomedicine has been an important part of nanotechnology from the very beginning and it is based on molecular knowledge of the human body and the involvement of molecular tools for the diagnosis and treatment of disease (Nanomedicine, www.nanobio-raise.org). Living organisms are built of cells that are typically 10 μm across. However, the cell parts are much smaller and are in the sub-micron size domain. Even smaller are the proteins with a typical size of just 5 nm, which is comparable with the dimensions of the smallest manmade nanoparticles.

This simple size comparison gives an idea of using nanoparticles as

very small probes that would allow us to spy at the cellular machinery without introducing too much interference. Understanding of biological processes on the nanoscale level is a strong driving force behind development of nanotechnology.

Today artificial bone implants already benefit from nanotechnological materials, nanostructures surfaces are used for controlled tissue-growth[10,11], antibacterial surfaces incorporating photocatalytic or biocidal nanoparticles[12] have reduced the risk of infections. Moreover, all kinds of medical devices profit from the miniaturization of electronic components as they move beyond micro to nano. Nanoparticulate pharmaceutical agents can penetrate cells more effectively and, stimulated from outside the body, they can destroy the tumor cells. New contrast agents (MRI, Magnetic Resonance Imaging) and visualization tools provide a closer look at cellular processes by using nanoparticles[13]. Portable testing kits allow for self-monitoring and speedy diagnosis[14]. Nanoparticles can be used for separation and purification of biological molecules and cells or for protein detection[15,16].

These are only some examples of nanomaterial applications to medicine and biology, and many others can be found in various reports on the prospects and promises of nanomedicine.

As mentioned above, the fact that nanoparticles exist in the same size domain as proteins makes nanomaterials suitable for biomedical applications. However, size is just one of the many characteristics that itself is rarely sufficient for their medical use. Generally, a biological or molecular layer acting as bioinorganic and inert interface is required for nanoparticle coatings, such as polymers, lipids, gel or silica, in a way to have biocompatible and stable particles.

The distribution of nanoparticles and their loads throughout the body depends on many physico-chemical factors: size, toxicity, surface charge, capacity for protein adsorption, drug loading and release kinetics, stability, degeneration of carrier systems, hydration

behaviour, electrophoretic mobility, porosity, surface characteristics, density and molecular weight. The increase of *therapeutic index*, that is the margin between the doses resulting in a therapeutic efficacy (i.e. tumor cell death) and toxicity to the other organs of the body, is needed for the preparation of long-lived and target-specific nanoparticles[17]: in fact, one of the problems in the use of particulate drug carriers is their entrapment in the reticuloendothelial system (RES), mainly in the liver and spleen, which can drastically reduce the time of permanence in the bloodstream[18,19]. Circulating mononuclear phagocytes (monocytes) clear the nanoparticles to the liver, spleen and bone where residence cells (e.g. Kupffer cells in the liver) capture and expel nanoparticles by feces. Smaller nanoparticles (< 50 nm) may be filtered by the kidneys and subject to rapid renal elimination, while larger ones (> 200 nm) can be removed by macrophages or dendritic cells. In general, the larger the particles are, the shorter their plasma half-life-period is. According to their size and their composition, different nanoparticle systems are used to target specific area of the body, as reported in the scheme in Figure 1.2. In addition, surface coatings play an essential role in retarding clearance by the RES. The most widely used coating for this purpose is PEG (polyethylene glycol) that inhibits recognition and phagocytosis by the RES because of its protein-resistant character. However, the “immunostealthing” function provided by PEG is frequently concurrent with the loss of biomolecular targeting capabilities. The nature of the coating is also important where the surface functionalization might cause hydrogen bonding and agglomeration of nanoparticles, reducing their stability in body fluids. Nevertheless, the fate and the toxicity of nanoparticles also depend strongly on the dose and administration route (oral, intravenous, pulmonary, transdermal, ocular).

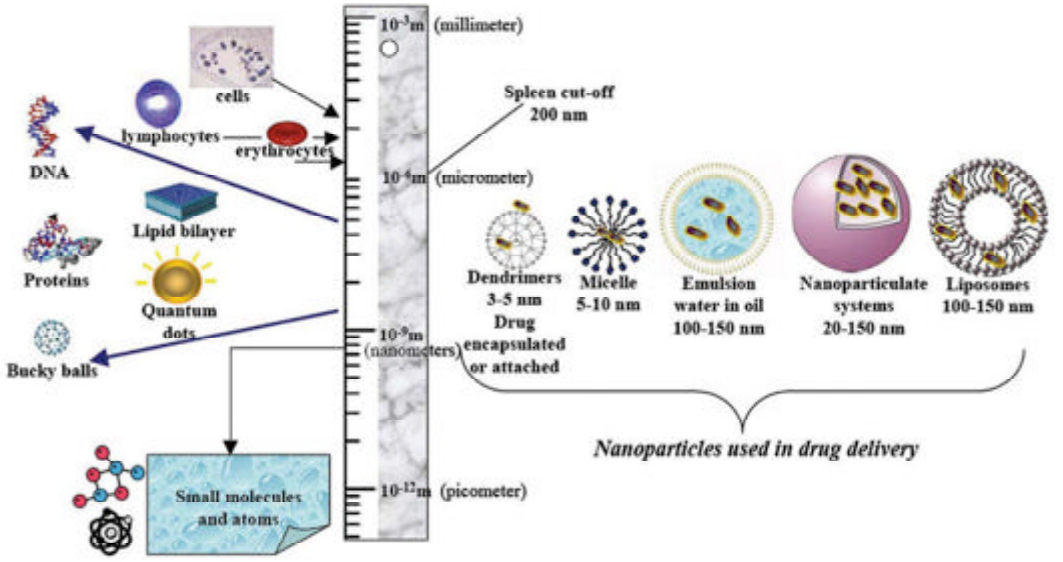

Figure 1.2. Nanoparticle systems for drug delivery applications and their biodistribution.

1.1.2 Magnetic nanoparticles for biomedical applications

The history of magnetism in medicine is old and is punctuated with amazing anecdotes about the pioneering work of physicians (*U. Hafeli, Magnetism in medicine: A handbook, 1998*). The first medical uses of magnetite powder were reported by Egyptians in the 10th century A.D. The magnetite was believed to render inert the poisonous iron by attracting it and speeding up its excretion. More recently, miniaturization of electromagnets, development of superconducting electromagnets and introduction of permanent magnets (Sm-Co and Nd-Fe-B) have stimulated the medical use of magnets in different fields (cardiology, oncology, radiology). In particular magnetic particles have found numerous medical applications, see the scheme in Figure 1.3, thanks to their small size and to their magnetic properties: in fact, the ability to distally control the position of particles in a given media to induce their

accumulation or separation from similar structures has found a spectrum of powerful applications in innovative medicines[20]. Generally, magnetic iron oxide nanoparticles are used because their low toxicity and their suitability for *in vivo* applications: in fact, iron-based particles do not cause oxidative stress or long-term changes in the levels of liver enzymes in rat models (an indicator of biosafety), and indeed good tolerances to high doses of such materials have been reported[21].

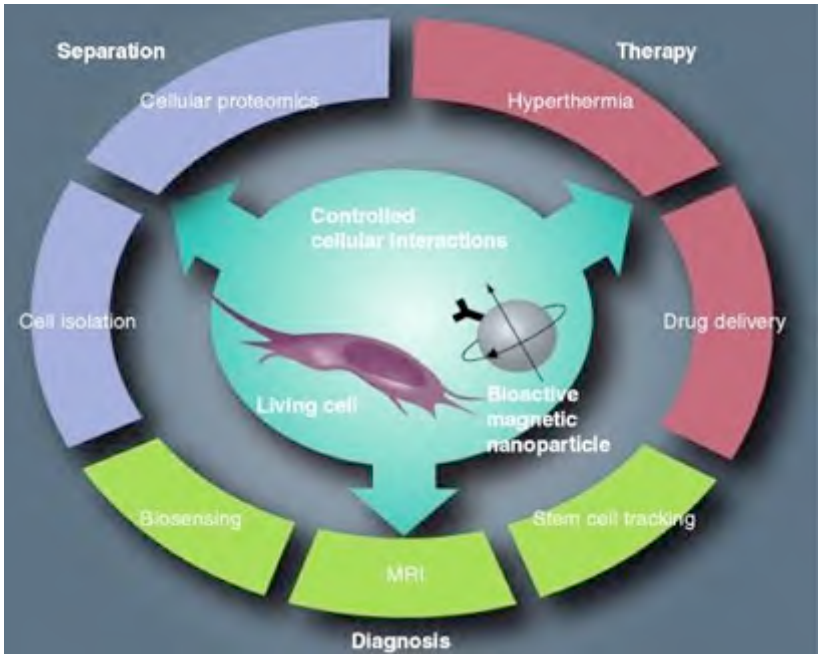

Figure 1.3. Magnetic nanoparticles applications in medicine

Although these iron-based materials are often referred to as "magnetic", the more accurate term "superparamagnetic" designates their ability to become magnetized upon exposure to a magnetic field but have no permanent magnetization (remanence) once the field is turned off. In addition, the application of inorganic or polymeric coating layers to magnetic particles minimizes hydrophobic interactions, thus enhancing desirable properties, such as colloid dispersion and biocompatibility (Figure 1.4). Strategies for the preparation of magnetic particles and their surface coating have been

recently summarized[8] and widely discussed in Chapter 3 about Drug-carriers preparation.

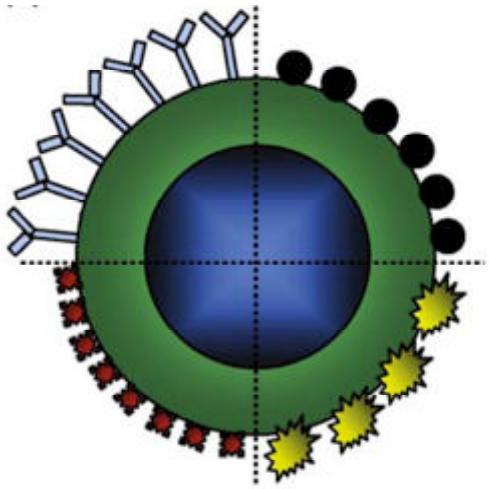

Figure 1.4. Architecture of magnetic particles (a) comprise the magnetic core (blue) usually made of ferromagnetic magnetite, and a polymeric coating layer (green). Depending on the intended function, additional elements can be incorporated, including antibodies (pale blue), drugs (black), imaging agents (yellow) or diverse chemical groups for specific or unspecific ligand binding (red).

The main applications of magnetic nanoparticles in medicine have been reported and described in the following paragraphs.

Magnetic Resonance Imaging (MRI)

Magnetic resonance imaging (MRI) is one of the most powerful non-invasive imaging modalities utilized in clinical medicine today. MRI is based on the property that hydrogen protons will align and process around an applied magnetic field, B_0. Upon application of a transverse radiofrequency (rf) pulse, these protons are perturbed from B_0. The subsequent process through which these protons return to their original state is referred to as the relaxation phenomenon. Two independent processes, longitudinal relaxation (T_1-recovery) and transverse relaxation (T_2-decay), can be monitored to generate an MRI. Local variation in relaxation, corresponding to image contrast, arises from proton density as well as the chemical and physical

nature of the tissues within the specimen.

Upon accumulation in tissues, magnetic nanoparticles provide magnetic resonance contrast enhancement (i.e., changes in signal intensity) by shortening both the longitudinal and transverse relaxation of surrounding protons. However, T_1 shortening processes require a close interaction between protons and T_1-agents, which can be hindered by the thickness of the coating on the magnetic nanoparticles (MNP). The effect of MNP on T_2 shortening is caused by the large susceptibility difference between the particles and surrounding medium resulting in microscopic magnetic field gradients. As described above, we can state that the effectiveness of a contrast agent can be described by its relaxivity, which is the proportionality constant of the measured rate of relaxation, or R_1 ($1/T_1$) and R_2 ($1/T_2$), over a range of contrast agent concentrations. The relaxivity of a sample is affected not only by the magnetic properties of the contrast agent, but also by experimental variables such as field strength, temperature, and the medium in which the measurements are made.

Some SPIO (superparamagnetic iron oxide nanoparticles) as bowel contrast agents (i.e., Lumiren® and Gastromark®) and liver/spleen imaging (i.e., Endorem® and Feridex IV®) are already on the market[22]. Several forms of ultrasmall superparamagnetic iron oxides (USPIO) have undergone clinical trials with one of the most notable being Combidex® which is in late stage clinical trials for use in the detection of lymph node metastases[23].

Molecular imaging has been defined as the non-invasive in vivo visual representation, characterization, and quantification of biological processes at the cellular and molecular levels. For instance, molecular imaging allows sensitive and specific monitoring of key molecular targets and host responses associated with early events in carcinogenesis. By coupling advances in medical imaging technology with those in molecular and cell biology, this growing research

discipline offers the potential to have a major impact on early disease detection, individualized treatment, and drug development. Due to their ability to serve as molecularly targeted imaging agents, MNP are now and will continue to play an integral role in this developing field.

Bioseparation and protein purification

The isolation of molecules, proteins and nucleic acids from natural samples requires that these macromolecules are separated from complex samples to be highly purified. Furthermore, emerging medical applications require the isolation of specific cell types from human samples, or alternatively, the depletion of undesired types from clinical material, such as the removal of cancer cells. These objectives can be achieved with the use of magnetically controlled particles, thus skipping the multiple-step approaches of conventional separation approaches.

Chromatographic protein purifications provide high-resolution separations, but these methods cannot handle “dirty” samples because colloidal contaminants frequently plug the packed-bed columns. By contrast, functionalized MNP allow for quick and efficient purification, eliminating the need for most of the pre-treatment steps, including centrifugation, filtration and membrane separation (Figure 1.5). To achieve this, magnetic particles can be decorated either with specificity ligands or with specific recognition groups, including monoclonal or polyclonal antibodies.

Among the existing protocols, magnetic separation and purification is a convenient method for selective and reliable capture of specific proteins, genetic materials, organelles and cells[24]. The high surface-to-volume ratio and the good dispersity of the nanoparticles also increase the protein binding capacity. The specificity of the MNP exhibited in protein separation suggests that MNP, as a general and versatile system, should selectively bind with other biological targets at low concentrations if proper anchors and ligands are used.

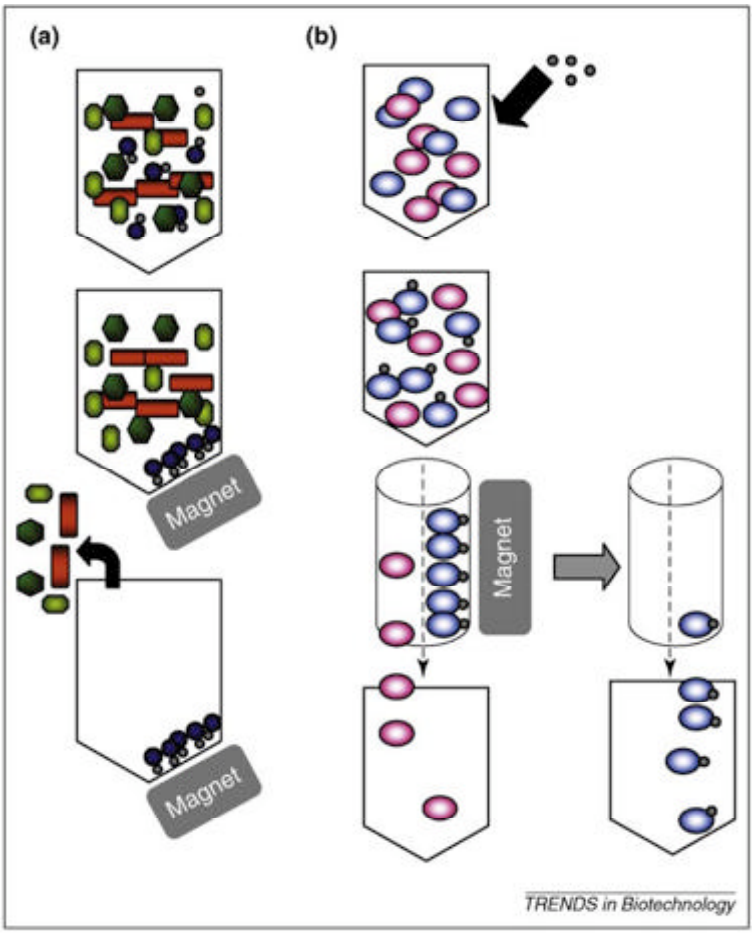

Figure 1.5. Schematic representation of magnetically driven separations (a) Target macromolecular species, usually proteins or nucleic acids (blue spheres), can be separated from potentially similar molecular species (green and orange symbols) by magnetic particles (gray spheres) that have been functionalized with specific ligands. After washing and elution, the target molecule can be recovered. (b) In magnetically assisted cell sorting (MACS), specific cell types are isolated from complex samples. Magnetic particles (gray spheres) are functionalized with ligands of surface receptors present in a single cell type (here in the blue cells), which permits their separation in a chromatographic column to which a magnet has been applied.

Tissue engineering

Tissue engineering exploits biology and engineering principles for the development of functional substitutes of lost or damaged tissues. Typically, tissue engineering has been based on the expansion of cells in vitro before seeding them onto three-dimensional (3D) biodegradable scaffolds to mimic their native organization and

differentiation, followed by the introduction of the colonized scaffold into the cell donor. An emerging tissue engineering strategy, so-called "*magnetic-force based tissue engineering*" (Mag-TE), employs cells that have been magnetically labeled with magnetoliposomes (liposomes embedded with MNP) which might also be further modified with integrin-binding peptides to facilitate cellular uptake. Magnetoliposomes labelled-cells can then be organized by magnetic force, as shown in Figure 1.6a[25].

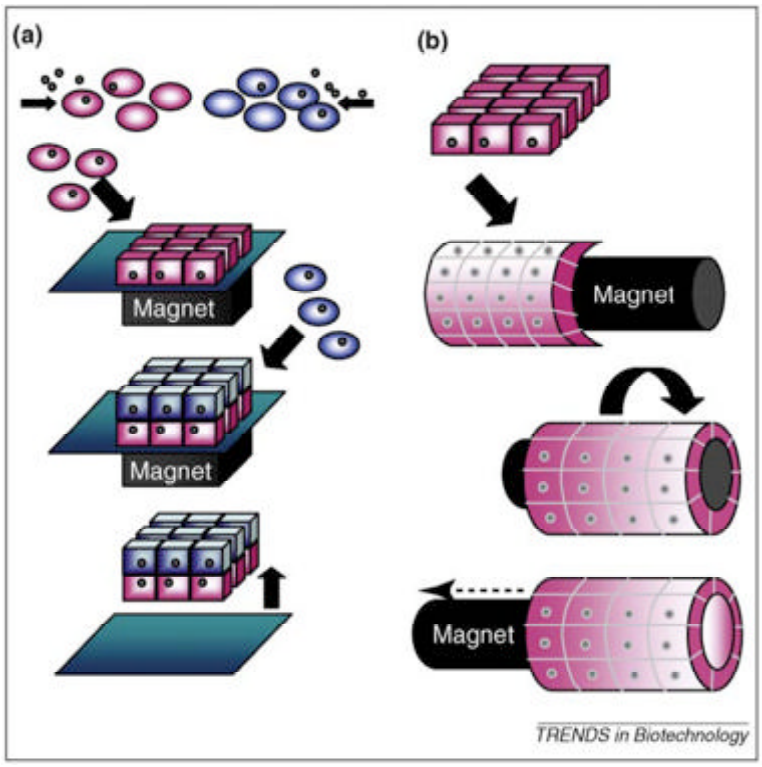

Figure 1.6. Magnetic particles in tissue engineering. (a) Different cell types (in purple and blue) are separately labeled by magnetoliposomes and sequentially seeded onto an ultra-low attachment plate under which a magnet is placed. This leads to the generation of 3D multilayered cell sheets by magnetic-force-based tissue engineering (Mag-TE). Removal of the magnet allows the recovery of the construct for use. (b) Tubular structures can be generated by folding preformed cell layers, obtained as shown in panel (a), around rod-shaped magnetic models. Such tubular constructs are recovered after removal of the magnet.

In this approach, a magnet is applied to the underside of ultra-low-attachment well plates, which attract and accumulate magnetically labeled cells. In this way, populations of magnetoliposome-labeled cells can be sequentially driven to the surface to create 2D patterned or even 3D multilayered structures[25,26].
Tubular structures have also been created using the Mag-TE method. In this approach, magnetically labeled cells formed a cell sheet onto which a cylindrical magnet was rolled, which was removed after the tubular structure had been formed (Figure 1.6b).

Drug delivery and gene delivery (transfection)

One of the most promising applications of nanotechnology in medicine is *drug delivery*, which has the purpose to deliver pharmaceutical agents directly to a specific site of the body, i.e. disease or cancer cells. The development of drug delivery started with the idea of Paul Ehrlich (1854-1915), who proposed the use of a "*magic bullet*" capable to target specificity disease cells in the body. The concept of using magnetic micro and nano-particles for *drug delivery* was proposed in the late 1970s by Widder et al, who described the targeting of magnetic albumin microsphere encapsulating an anticancer drug (doxorubicin) in animal models[27]. Ideally, magnetic particles could bear on their surface or in their bulk a pharmaceutical drug that could be easily directed to a specific site of the body by an external magnetic force, and once they have reached the target organ, they can release the bounded bioactive molecules. As result, a functional magnetic drug carrier consists of: a magnetic core, a protective coating and an active drug (chemo or radio-therapeutic agents). Analogously, magnetic nanoparticles could be use for *gene delivery* or *magnetofection:* in fact, magnetic particles associated with vector DNA could be transfected into cells by the influence of an external magnetic field. Generally high magnetic fields and high gradients are required to allow the particles to target the

specific site. While this may be effective for targets close to the body's surface, as the magnetic field strength falls off rapidly with distance, sites deeper within the body become more difficult to reach. For this reason some groups have recently proposed a way around this problem by implanting magnets near a target site, within the body[28,29].

The development of magnetically controlled drug release is due to the limitations of conventional treatments, including surgery, radiation, chemotherapy and biologic therapy (immunotherapy); i.e., because of their difficult accessibility to the tumor, the risk of operating on a vital organ, the spread of cancer cells throughout the body, and the lack of selectivity toward cancer cells.

The potential advantages of drug delivery systems based on the use of nano and micro-particles are:

- The ability to target specific location of the body
- The reduction of the quantity of drug needed to attain a particular concentration in the vicinity of the target
- The reduction of the drug concentration at non-target sites minimizing severe side effects
- Reduction in toxicity while maintaining therapeutic effects

The reason why nanoparticles are attractive for biomedical purposes is based on their high surface to mass ratio, their possibility to be functionalized and their ability to adsorb and carry other compounds. Generally, relatively large vectors (size > 100 nm) may be needed for loading larger amounts of drugs and the material of their composition may be of biological origin like phospholipids, lactic acid, dextran, chitosan, or may have more "chemical" characteristics like polymers, carbon, silica and surfactants[30]. The main characteristics that nanoparticles should have are biocompatibility, biodegradability and stability in order to prevent aggregation or toxicity.

Vectors sensitive to physical stimuli have been developed and conjugated to drugs. Nanoparticles must be endowed with specific

characteristics needed to reach a specific target, which means attaining a suitable combination of nature, size, way of drug conjugation (adsorbtion, encapsulation, attachment), and physical response properties at different external stimuli. Recently, the most common methods to favor drug leakage from nanoparticle-carriers (polymer, gel, liposomes) are based on the destabilization of the system by an external *stimulus* such as pH changes[31], temperature increase (hyperthemia)[32-35], magnetic exposure[36,37], ultrasounds application[38,39] and ionic strength changes[40].

Magnetically mediated hyperthermia is a particular application of magnetic nanoparticles in drug delivery (Figure 1.7a). Magnetite particles exposed to an external alternating magnetic field (AMF) are heated through either hysteresis loss or relaxation loss depending on their size and properties. Because cancer cells are killed at temperature over 44°C, whereas normal cells survive at these higher temperatures, magnetically mediated hyperthermia induced by AMF can be used to selectively destroy cancer cells in which magnetic particles have been accumulated (Figure 1.7b).

Nucleic acid transfer and gene therapy have been areas of intense research in recent years due to their potential to generate a significant impact in medicine. However, the delivery of genes and their resulting transfections efficiency are often limited by their short half-life in vivo, lack of specificity and poor diffusion across cell membranes. The use of MNP as carriers for DNA or gene vectors overcomes many of the problems associated with the delivery of these therapeutic agents. *Magnetofection*, the magnetically enhanced nucleic acid delivery method, uses magnetic force to direct nucleic acids attached to magnetic nanoparticles towards and into target cells (by placing a magnet under the cell culture plate[41].

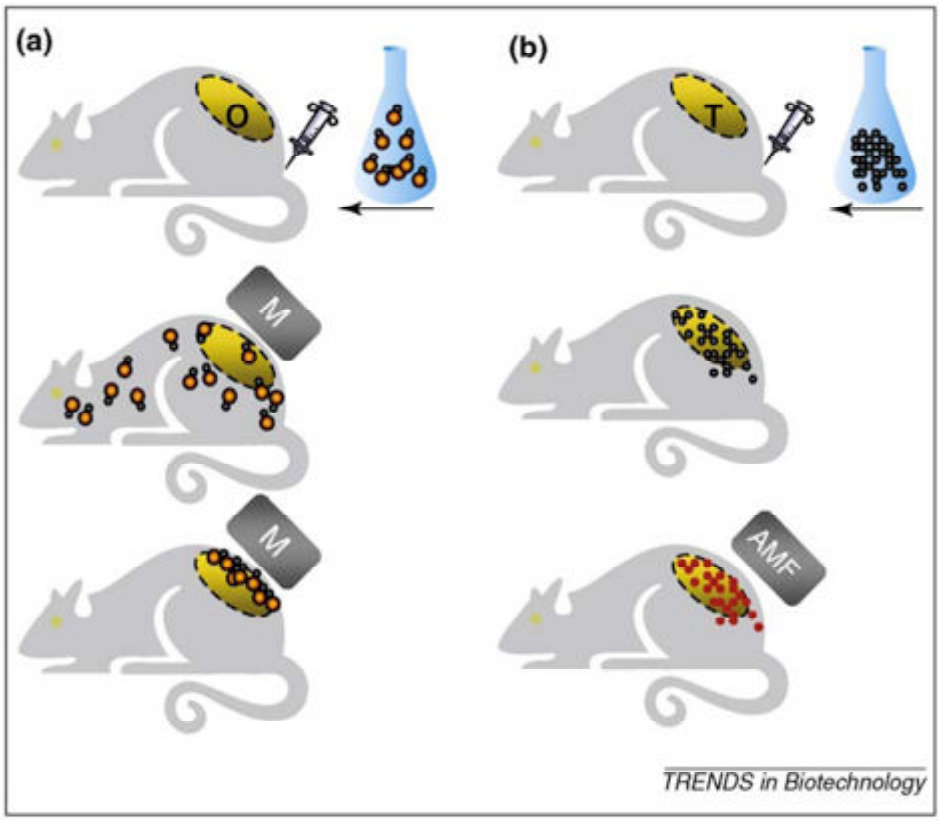

Figure 1.7. In vivo therapeutic applications of distally controlled magnetic nanoparticles. (a) Magnetic particles (gray spheres) associated to therapeutic molecules (shown as orange spheres) act as vehicles for drug delivery, and after systemic administration they are concentrated to the target organ (O) with the help of a magnet (M). (b) In magnetically mediated hyperthermia (MMH), systemically administered magnetic particles (gray spheres) accumulate in a tumor (T). Particles in the tumor are then heated (illustrated by the change to red spheres) through the external application of an alternating magnetic field (AMF), and this results in the death of the tumor cells.

As described above, an external magnetic field is generally required for MNP applications in biomedicine. Although all the components of the body are either dia-, para-, superpara-, ferri- or ferromagnetic, the magnetic fields must be very large. Even red blood cells, which each contains micrograms of the Fe protein haemoglobin, show a relatively low response to large fields or field gradients. Many studies have shown that also magnetic field of 10 T could be achieved for human imaging[42]. However, strong static magnetic field of 8 T have shown to reduce the flow rate of human blood by 30% in vitro tests

and it has been reported that magnetic fields above 3 T might effect the normal behaviour of erythrocytes[43].

1.2 Magnetic Nanoparticles

Magnetic nanoparticles (MNP) are of great interest for researchers from a wide range of disciplines, as described above. In most of the envisaged applications, the particles perform best when the size of the nanoparticles is below a critical value, which is dependent on the material, but is typically around 10–20 nm. Then each nanoparticle becomes a single magnetic domain and shows *superparamagnetic* behaviour when the temperature is above the so-called blocking temperature. Such individual nanoparticles have a large constant magnetic moment and behave like a giant paramagnetic atom with a fast response to applied magnetic fields with negligible remanence (residual magnetism) and coercivity (the field required to bring the magnetization to zero). These features make superparamagnetic nanoparticles very attractive for a broad range of biomedical applications because the risk of forming agglomerates is negligible at room temperature.

However, an unavoidable problem associated with particles in this size range is their intrinsic instability over longer periods of time. Such small particles tend to form agglomerates to reduce the energy associated with the high surface area to volume ratio of the nanosized particles. Moreover, naked metallic nanoparticles are chemically highly active, and are easily oxidized in air, resulting generally in loss of magnetism and dispersibility.

For many applications it is thus crucial to develop protection strategies to chemically stabilize the naked magnetic nanoparticles against degradation during or after the synthesis. These strategies comprise grafting of or coating with organic species, including surfactants or polymers, or coating with an inorganic layer, such as silica, citrate or oleic acid.

A brief description of magnetism and magnetic properties of materials is reported below to better understand the magnetic behaviour of superparamagnetic nanoparticles.

1.2.1 Magnetic properties of nanoparticles

Magnetism is the result of charge movements, and therefore the magnetic properties of matter are related to both the orbital and spin motions of electrons. Other contributions, such as nuclear magnetic moment, are usually negligible. Depending on the electronic structure, materials are characterized by different magnetic properties and different interactions with external magnetic fields. The magnetic susceptibility, χ, is an estimate of the magnetization M response to an external magnetic field H and it is defined as $\chi = \delta M / \delta H$.

Diamagnetism appears in all materials, and is the tendency of a material to oppose an applied magnetic field, and therefore, to be repelled by a magnetic field.

In a diamagnetic material, there are no unpaired electrons, so the intrinsic electron magnetic moments cannot produce any bulk effect.

Paramagnetism appears when materials have unpaired electrons, so that an external magnetic field induces a net magnetization, which is not preserved after the external magnetic field removal.

Ferromagnetism appears when materials possess all unpaired electrons, and therefore a high magnetic susceptibility. Ferromagnetic materials are permanent magnets and they remain magnetized even after a magnetic field removal.

Superparamagnetism is a form of magnetism, which appears in small ferromagnetic nanoparticles. In small enough nanoparticles, magnetization can randomly flip direction under the influence of temperature. Two key issues dominate the magnetic properties of nanoparticles: finite-size effects and surface effects. In large magnetic particles, it is well known that there is a multi-domain structure,

where regions of uniform magnetization are separated by domain-walls. If the sample size is reduced, there is a critical volume below which it costs more energy to create a domain wall than to support the external magnetostatic energy of the single-domain state. This critical diameter typically lies in the range of a few tens of nanometers and depends on the material. A single-domain particle is uniformly magnetized with all the spins aligned in the same direction. The magnetic anisotropy per particle, which is responsible for holding the magnetic moments along a certain direction, is proportional to the energy barrier (KV, where K is the anisotropy constant and V the particle volume) between two energetically equivalent easy directions of magnetization. With decreasing particle size, the thermal energy, k_BT, exceeds the energy barrier and the magnetization is easily flipped. For $k_BT>KV$ the system behaves like a paramagnet and the system is named *superparamagnet* because of the presence of a single giant moment inside each particle[44].

Normally, any ferromagnetic material undergoes a transition to a paramagnetic state above its *Curie temperature*, which is the temperature at which a ferromagnetic material becomes paramagnetic on heating.

Superparamagnetism is different from this standard transition since it occurs below the Curie temperature of the material. Superparamagnetism occurs in nanoparticles composed of a single magnetic domain. This is possible when their diameter is below a critical diameter, which depends on the materials and the shape. In this condition, it is considered that the magnetization of the nanoparticles is a single giant magnetic moment (one magnetic domain), sum of all the individual magnetic moments carried by the atoms of the nanoparticle. In this state, there is a finite probability for the magnetization (the giant moment) of the nanoparticle to flip and reverse its direction. The global relaxation rate of the magnetic colloid is the sum of two different contributions: the Néel relaxation

and the Brown relaxation.

The Néel relaxation time, τ_N, is given by the following Néel-Arrhenius equation:

$$\tau_N = \tau_0 \exp\left(\frac{KV}{k_B T}\right) \quad (1.1)$$

where:

- τ_N is the average length of time that it takes for the nanoparticle magnetization to randomly flip as a result of thermal fluctuations.
- τ_0 is a length of time, characteristic of the material, called the *attempt time* or *attempt period*; its typical value is 10^{-9} second.
- K is the nanoparticle magnetic anisotropy and V its volume. KV can be thought of as the energy barrier associated with the magnetization moving from its initial "easy axis" direction, through a "hard axis", ending at another easy axis.
- k_B is the Boltzmann constant.
- T is the temperature.

This length of time can be anywhere from a few nanoseconds to years or much longer. In particular, it can be seen that the Néel relaxation time is a function of the exponential of the grain volume, which explains why the flipping probability becomes rapidly negligible for bulk materials or large nanoparticles.

The Brown relaxation (τ_B) is the viscous rotation of the entire nanoparticle and is given by the following equation:

$$\tau_B = \frac{3V\eta}{kT} \quad (1.2)$$

where V is the volume of the particle, η is the viscosity of the solvent, k is the Boltzman constant and T the temperature.

Nèel and Brown relaxations are schematized in Figure 1.8.

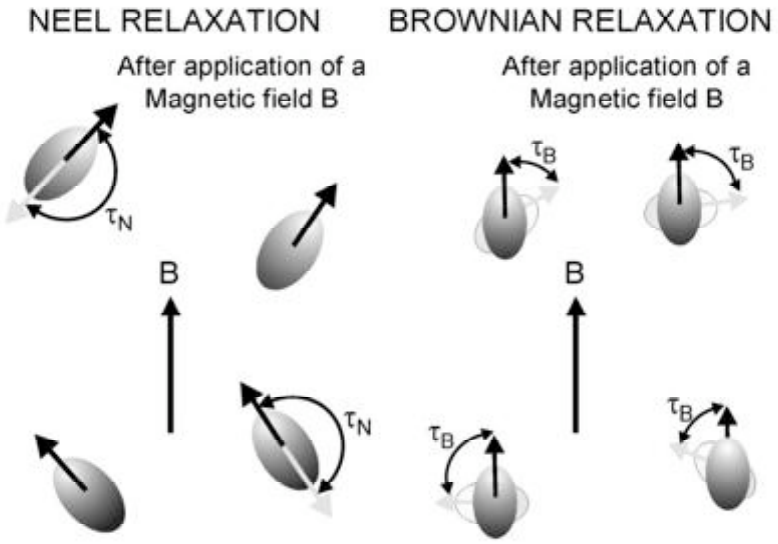

Figure 1.8. Illustration of the two components of the magnetic relaxion of a magnetic fluid.

If the magnetization of a single superparamagnetic nanoparticle could be measured, and τ_m considered the measurement time, τ_m could be compared to τ_N. If $\tau_m >> \tau_N$, the nanoparticle magnetization will flip several times during the measurement so the magnetization measured will be zero. If $\tau_m << \tau_N$, its magnetization will not flip during the measurement so the magnetization measured will be the magnetic moment carried by the nanoparticle. In the first case, the nanoparticle will appear to be in the *superparamagnetic* state whereas in the second case it will appear to be *ferromagnetic*. The state of the nanoparticle (superparamagnetic or ferromagnetic) depends on the measurement time. In several experiments, the measurement time is kept constant but the temperature is varied so the transition between superparamagnetism and ferromagnetism is seen as a function of the temperature. The temperature for which $\tau_m = \tau_N$ is called the ***blocking temperature*** because, below this temperature, the magnetization is seen "blocked" on the time scale of the measurement.

1.3 Lipid vesicles

Lipid vesicles are hollow microspheres, formed by self-assembly in water of phospholipids. Their membrane consists of one or more lipid bilayers, which entrap the aqueous medium in which they are suspended.

Lipid vesicles can be classified in function of their size and physical structure. Multilamellar lipid vesicles (MLV) are usually larger than 500 nm and consist of several concentric bilayers; unilamellar vesicles, formed by a single bilayer, are classified as: small (SUV) when size range between 20 and 100 nm, large (LUV) when diameter range from 100 nm to 1 μm, and giant (GUV) when they are larger than 1 μm (Figure 1.9).

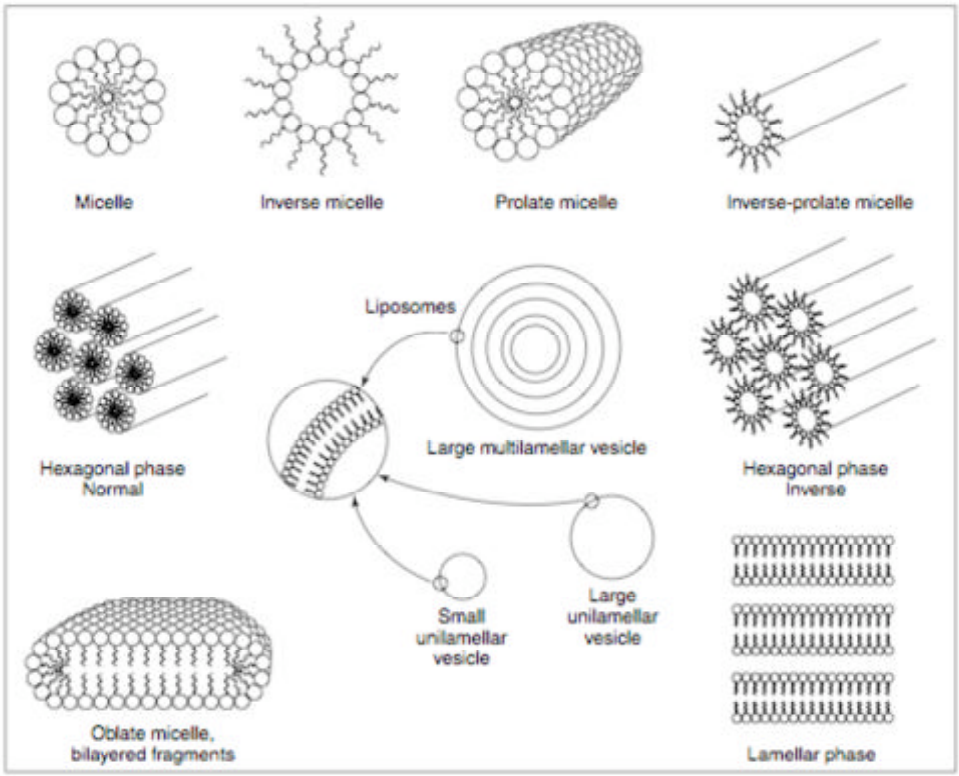

Figure 1.9. Molecular shape of lipids and vesicle classification

Because of the amphiphilic character of the phospholipids, liposomes can encapsulate both hydrophobic molecules in the bilayer membrane and hydrophilic molecules in the aqueous internal pool. These properties have led to a lot of applications of lipid vesicles as models for biological membranes, as drug delivery vectors for in vivo applications and for gene-therapy. Drugs, vaccines, DNA, antibodies and other molecules can interact with liposomes in several different ways depending on their chemical and physical properties. They can be inserted in the lipid chain bilayer region, intercalated in the polar head group region, adsorbed on the membrane surface, anchored by hydrophobic tail or entrapped in the inner aqueous pool. The large use of liposomes for biomedical applications is related, in addition to their amphiphilic properties, to their attractive biological properties:

- They are biocompatible
- Size, charge and surface properties can be easily changed by adding new ingredients to the lipid mixture before liposomes preparation and/or by variation of preparation methods.
- They protect pharmaceuticals from the inactivating effect of external conditions.
- They can deliver pharmaceuticals into cells or even inside individual cell compartments.

An important requisite for the use of liposomes as drug delivery vehicles is to develop methods allowing to control liposome preparation, including particle size, stability, encapsulation rates and to determine the leakage kinetics of the entrapped substances.
In order to better understand liposome behaviour, some general features of amphiphiles and phospholipids are presented below.

1.3.1 Amphiphiles and phospholipids

Amphiphiles, also referred to as surfactants, are molecules that contain both hydrophobic (non-polar tail) and hydrophilic (polar

head) part. Because of this dual character and the energetically unfavourable contact between the non-polar part and water, amphiphiles spontaneously aggregate. There is a wide variability of aggregates of different sizes and geometries depending on both hydrophobic tail and polar head properties. The tail length, consisting of multiple chains, the polar head charge and size, temperature, pH and concentration influence the geometry of the aggregate.

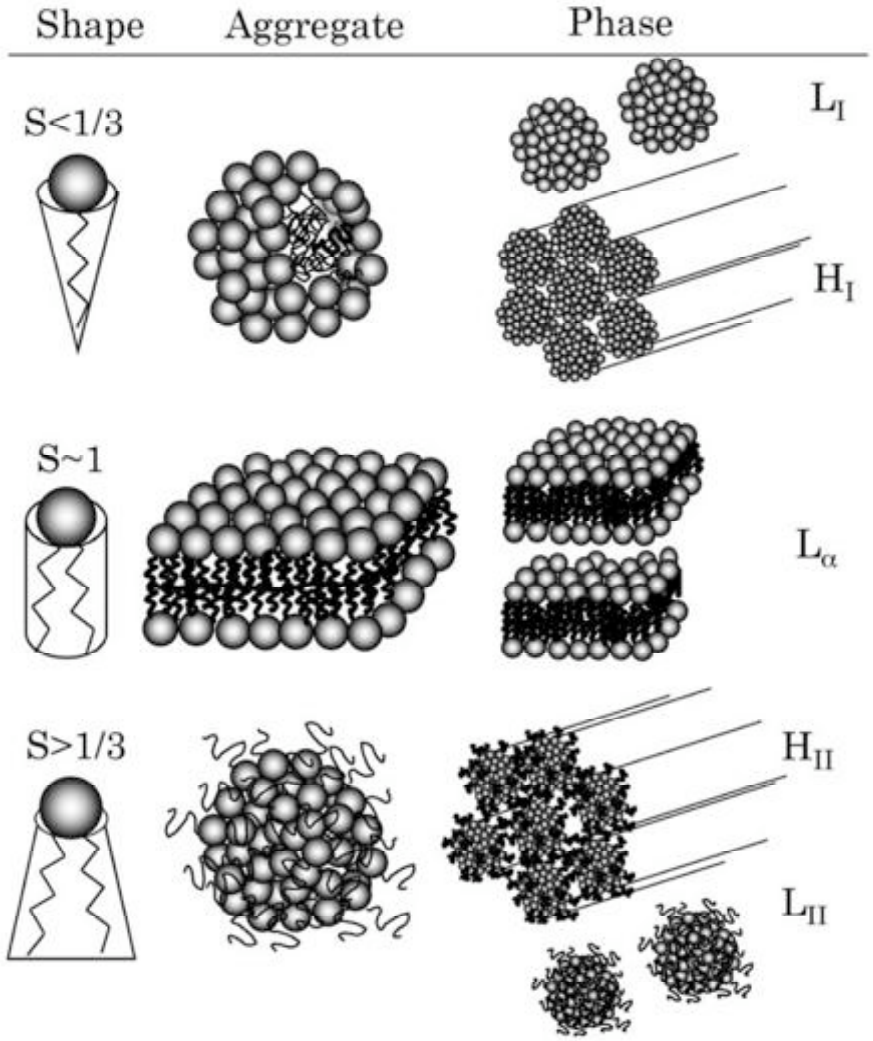

Figure 1.10. The surfactant parameter S and the corresponding geometrical packing of amphiphilic molecules. L: micellar solution, H: hexagonal phase, L_α: lamellar phase. Subscripts I and II denote normal and reversed phase, respectively.

A surfactant parameter, S, contains information about the geometrical shape and curvature of the aggregate obtained from a certain surfactant.

The surfactant parameter, S, is defined by $S = \frac{v}{la_0}$, where ν stands for the volume of the hydrophobic portion, l, is the length of the hydrocarbon chains and a_o is the effective area per head group. The value of S relates the properties of the molecule to the mean curvature of the formed aggregates. By convention the curvature is positive (micelles) if the aggregate is curved around the hydrophobic part and negative (reversed micelles) if it is curved towards the polar part. The relationship between the value of the surfactant parameter and the optimal aggregate structure is shown in Figure 1.10.

Although the surfactant parameter can only be considered to be a crude and approximate model for predicting self-assembly, it provides valuable insight into how changes of molecular structure affect the shape of the formed aggregate.

A class of amphiphilic molecules is phospholipids, which are the major component of all cell membranes in the form of lipid bilayer. A phospholipid has two acyl chains, usually consist of saturated or unsaturated long fatty acids, linked to a head group (coline, serine, ethanolamine) by means of a phosphoglycerol-backbone. Figure 1.11 shows the structural formula of a phospholipid. Phosphatidylcholines or PC-lipids are the most widely used lipids in liposomes work. PC-lipids are zwitterionic at all relevant pH and can therefore form lamellar structures independently of the pH in the solution.

Phospholipid lamellar phases may exist in different physical states in function of temperature and lipid composition. Low temperature or a high degree of saturation forces the bilayer into a gel state, in which hydrocarbon chains exhibit close packing and more or less frozen conformation. Increasing the temperature or introducing unsaturated acyl chains results in a bilayer of a liquid crystalline

state, where the chains are disordered and have high mobility. The temperature at which the gel-to-liquid crystalline phase transition occurs is the melting temperature (T_m). Comparing an unsaturated phospholipid with the saturated analogue, the T_m of the last one will be significantly higher.

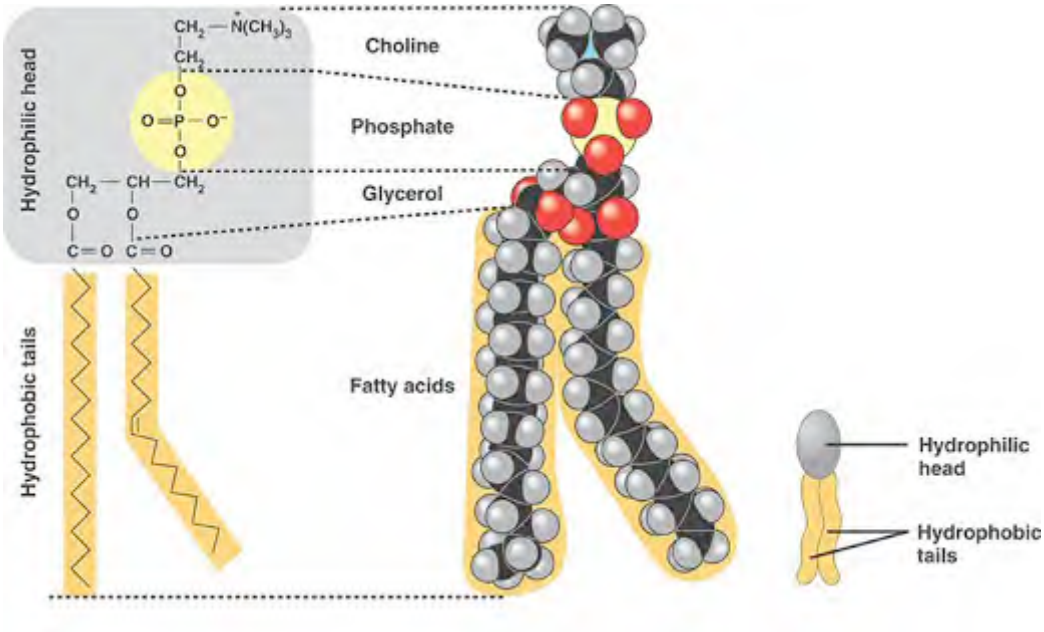

Figure 1.11. Structure of a phospholipid (in this case phosphatidylcholine).

The molecular geometry of most phospholipids can be approximated as cylinders and according to the geometrical packing concept, they prefer to self-assemble into bilayers. The formation of liposomes from bilayer structures by self-closing is in competition with the bending (curavature energy) and the edge energy of a bilayer.

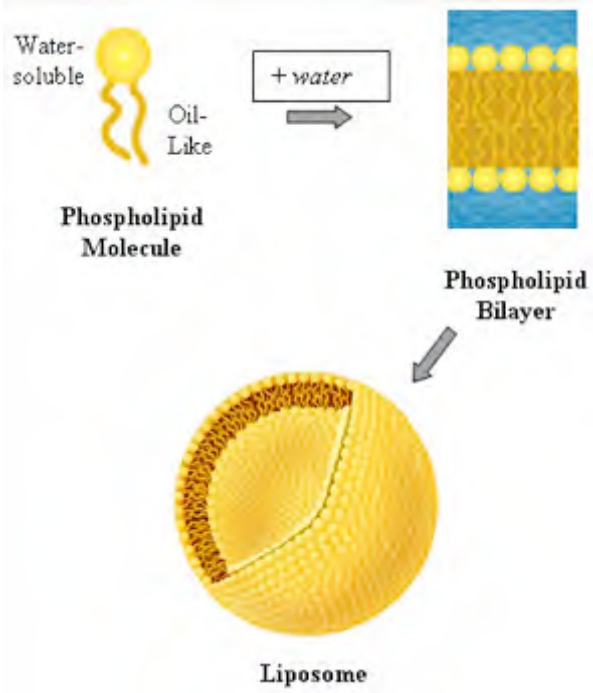

Figure 1.12. Liposome formation

The bilayer bending can reduce the edge energy, and when the increase of the curvature lead to a closed sphere, the edge energy is reduced to zero, while the bending energy is at its maximum. Generally larger liposomes are energetically favoured. A scheme of the liposome formation is reported in Figure 1.12.

1.3.2 Stability and applications of liposomes

The nature of lipids and the special properties of liposomes have generated many applications in medicine, in particular they have found application as vaccine and drug carriers, model membranes and in cell physiology studies.

Liposome use in drug delivery depends on their physicochemical properties (i.e. size, surface charge) and on their biological interactions with the cells. Biological stability includes control over the rate of clearance of liposomes from circulatory system or compartments of the body. The rate of clearance is dose-dependent and varies according to the size and surface charge of the liposomes.

In addition, biological stability also comprises retention of the drug by the carrier en route to its destination (sustained release). For example, lipoproteins in the plasma were found to remove phospholipids rapidly from the bilayers of the vesicles, leading to their disintegration and premature drug loss. Moreover lipids, like most biomolecules, undergo different degradation processes and the most common are oxidation and hydrolysis. In the case of phosphatidylcholine, which is the most commonly used lipid in medicine applications, the hydrocarbon chains and especially the unsaturated ones are subject to oxidation. The oxidation is a radical reaction, which finally results in the cleavage of the hydrocarbon chains or in the formation of cyclic peroxides. The use of lipids with high purity, the protection from light and oxygen, and the storage at low temperature can minimize lipid oxidation.

The ester bonds present in phospholipids may be subject to hydrolysis in water, in particular the carboxyl esters are hydrolysed faster than the phosphate esters. The hydrolysis rate is both pH and temperature dependent, and by selecting low temperature and neutral pH the hydrolysis can be largely avoided.

However oxidation and hydrolysis of liposomes occur, in vivo, concomitant with their interaction with blood components. An approach to avoid lipid degradation and to prolonging the circulation time of liposomes involves making their surface highly hydrophilic by covalently attaching polymers or PEG to them.

Liposomes functionalized with cell-specific ligands can be loaded with different drugs in order to promote cell recognition and transport the drug to a specific target[17,45] minimizing the distribution of drugs to non-targeted tissues. Drug molecules can interact with liposomes in several different ways depending on the drug's solubility and polarity characteristics. Water-soluble drugs are usually entrapped into the aqueous pool, while water-insoluble drugs can be solubilized in the hydrophobic bilayer of liposomes. Hydrophilic drugs are most simply

encapsulated automatically upon hydration of the lipids with a corresponding drug solution. Hydrophobic drugs are generally mixed with the lipid solution in an organic solvent and entrapped in the lipid bilayer during the formation of phospholipid films. The non-encapsulated drug molecules can be then removed by size exclusion chromatography (SEC) or dialysis. Once drug-loaded liposomes have reached the target site, the drug must to be released with an efficient rate. This can be obtained through the destabilization of the delivery system by an external *stimulus,* followed by the leakage of the drug. On this basis, although trans-membrane diffusion of the embedded drug takes place spontaneously in liposomes, in many cases a controlled, fast and complete release of the drug is required.

Many factors have been shown to affect liposome permeability[46], such as a temperature increase especially when close to the lipid melting temperature (T_m)[47], the doping with large headgroup amphiphiles[48], etc. In general, the permeability is correlated to the lateral compressibility consistently with the formation of defects and/or pores promoting the diffusion. Enhanced drug release has been achieved by using pH-sensitive lipids[31], by stimulating temperature-sensitive liposomes via local hyperthermia[32,36], and by mechanical disruption with low frequency ultrasounds[38,39].

1.4 The project aim

Aim of this project is to study the effect of a low-frequency magnetic field (LF-AMF) on the permeability and release properties of magnetic nanoparticles-embedded liposomes (magnetoliposomes). Large (LUVs) and giant (GUVs) unilamellar vesicles loaded with three different Cobalt Ferrite Nanoparticles ($CoFe_2O_4$ NPs): uncoated, citrate and oleic acid coated Nps were prepared and characterized. The hydrophilic nanoparticles (uncoated and citrate coated NPs) were embedded in the aqueous pool of liposomes, while the hydrophobic ones (coated with oleic acid) were entrapped in the lipid bilayer of liposomes. According to their sub-micrometer diameter, LUVs or liposomes are used for in vivo applications, while GUVs are used as cellular models to study membrane perturbations in the presence of an external *stimulus*[49,50].

A number of investigations have been reported on exploiting superparamagnetic NPs in targeted and controlled release of drugs[33,37,51]: in fact, magnetic NPs can be efficiently encapsulated inside lipid vesicles and used for targeting a specific location of the body by an external magnetic force[9]. A way to promote drug release and to tune magnetoliposome permeability is the application of an alternating magnetic field. In most cases a high-frequency alternating magnetic field (HF-AMF) was used to promote local heating, or magnetic fluid hyperthermia (MFH) of Nps, which are located in the targeted tumor cells, causing their thermal ablation without damaging the healthy tissues[36]. In this thesis, for the first time, a low frequency alternating magnetic field (LF-AMF, frequency < 10 kHz) was used in order to minimize the temperature contribution and investigate mainly the field effect. Cobalt Ferrite NPs were produced introducing some modifications to the method originally proposed by Massart (see Methods and Drug-carriers) and they were then used to

load the pool of lipid vesicles. The increase of magnetoliposome permeability upon exposure to LF-AMF was evaluated as the self-quenching decrease of the fluorescent molecule Carboxyfluorescein (CF) entrapped in the liposome pool. Liposome leakage was monitored as a function of field frequency, time of exposure, size, charge, concentration and different coatings of NPs. To gain further knowledge into the leakage mechanism induced by LF-AMF, Confocal Laser Sanning Microscopy (CLSM) experiments were performed on magnetic GUVs labeled with the fluorescent probe $DiIC_{18}$ and filled with the water-soluble fluorescent dye Alexa 488-maleimide. Moreover fluorescent and magnetic particles were also prepared and used as a system for locating their position in GUVs and to study the effect of a LF-AMF on the permeability of magnetic vesicles by Confocal Laser Scanning Microscopy (CLSM). Silica-coated Cobalt ferrite nanoparticles incorporating Rhodamine B isothiocyanate MP@SiO_2(RITC) were synthesized by a sol-gel method[52-54] and incorporated on GUVs. Drug release experiments were carried out by CLSM-time series acquisition, measuring the change in fluorescence intensity of the Alexa 488-C5-maleimide fluorescent dye loaded in the aqueous pool of GUVs, in order to check the vesicle permeability changes or their structure deformations during and after the LF-AMF exposure.

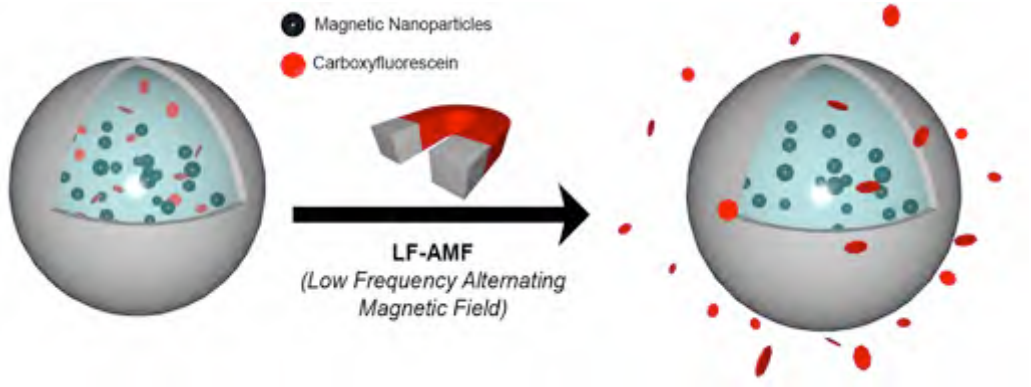

Figure 1.13. Sketch of $CoFe_2O_4$ nanoparticles-embedded liposomes containing carboxyfluorescein (CF) and subsequent CF release upon application of low frequency alternating magnetic field (LF-AMF).

1.5 References

(1) Bagham, A. D.; Flemans, R.; Heard, D. H.; Seaman, G. V. F. *Nature* **1958**, *182*, 682-684.
(2) Allen, T. M.; Cullis, P. R. *Science* **2004**, *303*, 1818-1821.
(3) Lasic, D. D. *Trends in Biotechnology* **1998**, *16*, 307-321.
(4) Torchilin, V. P. *Nature Reviews* **2005**, *4*, 145-160.
(5) Woodle, M. C. *Adv.Drug Delivery Rev.* **1995**, *16*, 249-265.
(6) Al-Jamal, W. T.; Al-Jamal, K. T.; Bomans, P. H.; Frederik, P. M.; Kostarelos, K. *SMALL* **2008**, *4*, 1406-1415.
(7) Kloepfer, J. A.; Cohen, N.; Nadeau, J. L. *J. Phys. Chem. B* **2004**, *108*, 17042-17048.
(8) Laurent, S.; Forge, D.; Port, M.; Roch, A.; Robic, C.; Elst, L. V.; Muller, R. N. *Chemical Reviews* **2008**, *108*, 2064-2110.
(9) Lesieur, S.; Grabielle-Madelmont, C.; Menager, C.; Cabuil, V.; Dadhi, D.; Pierrot, P.; Edwards, K. *J. Am. Chem. Soc.* **2003**, *125*, 5266-5267.
(10) de la Isla, A.; Brostow, W.; Bujard, B.; Estevez, M.; Rodriguez, J. R.; Vargas, S.; Castano, V. M. *Materials Research Innovations* **2003**, *7*, 110-114.
(11) Ma, J.; Wong, H. F.; Kong, L. B.; Peng, K. W. *Nanotechnology* **2003**, *14*, 619-623.
(12) Falletta, E.; Bonini, M.; Fratini, E.; Lo Nostro, A.; Pesavento, G.; Becheri, A.; Lo Nostro, P.; Canton, P.; Baglioni, P. *Journal of Physical Chemistry C* **2008**, *112*, 11758-11766.
(13) Weissleder, R.; Elizondo, G.; Wittenberg, J.; Rabito, C. A.; Bengele, H. H.; Josephson, L. *Radiology* **1990**, *175*, 489-493.
(14) Chen *Current opinion in chemical biology* **2006**.
(15) Molday *J. Immunol. Methods* **1982**.
(16) Nam, J. M.; Thaxton, C. S.; Mirkin, C. A. *Science* **2003**, *301*, 1884-1886.
(17) Mastrobattista **1999**.
(18) Vonarbourg, A.; Passirani, C.; Saulnier, P.; Benoit, J. P. *Biomaterials* **2006**, *27*, 4356-4373.
(19) Could *Nano today* **2006**.
(20) Corchero, J.; Villaverde, A. *Trends in Biotechnology* **2009**, *27*, 468-476.
(21) Lubbe, A. S.; Bergemann, C.; Riess, H.; Schriever, F.; Reichardt, P.; Possinger, K.; Matthias, M.; Dorken, B.; Herrmann, F.; Gurtler, R.; Hohenberger, P.; Haas, N.; Sohr, R.; Sander, B.; Lemke, A. J.; Ohlendorf, D.; Huhnt, W.; Huhn, D. *Cancer Research* **1996**, *56*, 4686-4693.
(22) Wang, Y. X. J.; Hussain, S. M.; Krestin, G. P. *European Radiology* **2001**, *11*, 2319-2331.
(23) Harisinghani, M.; Barentsz, J.; Weissleder, R. *New England*

Journal of Medicine **2003**, *349*, 1186-1186.
(24) Safarik *BioMagnetic Research and Technology* **2004**.
(25) Ito *Tissue Enginnering Journal* **2004**.
(26) Akiyama *Biomedical Microdevices* **2009**, *11*.
(27) Rettenmaier, M. A.; Stratton, J. A.; Berman, M. L.; Senyei, A.; Widder, K.; White, D. B.; Disaia, P. J. *Gynecologic Oncology* **1987**, *27*, 34-43.
(28) Kubo, T.; Sugita, T.; Shimose, S.; Nitta, Y.; Ikuta, Y.; Murakami, T. *International Journal of Oncology* **2000**, *17*, 309-315.
(29) Yellen, B. B.; Forbes, Z. G.; Halverson, D. S.; Fridman, G.; Barbee, K. A.; Chorny, M.; Levy, R.; Friedman, G. *Journal of Magnetism and Magnetic Materials* **2005**, *293*, 647-654.
(30) Gupta, A. K.; Gupta, M. *Biomaterials* **2005**, *26*, 3995-4021.
(31) Mills, J. K.; Eichenbaum, N.; Case, N.; Needham, D. *J. Liposome Res.* **1999**, *9*, 275-290.
(32) Needham, D.; Dewhirstb, M. W. *Adv.Drug Delivery Rev.* **2001**, *53*, 285-305.
(33) Hsu, M.-H.; Su, Y.-C. *Biomed. Microdevices* **2008**, *10*, 785-793.
(34) Ito, A.; Kuga, Y.; Honda, H.; Kikkawa, H.; Horiuschi, A.; Watanabe, Y.; Kobayashi, T. *Cancer Letters* **2004**, *212*, 167-175.
(35) Viroonchatapan, e.; Sato, H.; Ueno, M.; Adachi, I.; Tazawa, K.; Horikoshi, I. *J. Control Release* **1997**, *46*, 263-271.
(36) Babincova, M.; Cicmanec, P.; Altanerova, V.; Altaner, C.; Babinec, P. *Bioelectrochemistry* **2002**, *55*, 17-19.
(37) Hu, S.-H.; Liu, T.-H.; Huang, H.-Y.; Liu, D.-M.; Chen, S.-Y. *Langmuir* **2008**, *24*, 239-244.
(38) Lin, H.-Y.; Thomas, J. L. *Langmuir* **2003**, *19*, 1098-1105.
(39) Schroeder, A.; Avnir, Y.; Weisman, S.; Najajreh, Y.; Gabizon, A.; Talmon, Y.; Kost, J.; Barenholz, Y. *Langmuir* **2007**, *23*, 4019-4025.
(40) Beaune, G.; Menager, C.; Cabuil, V. *J. Phys. Chem. B* **2008**, *112*, 7424-7429.
(41) Plank, C.; Schillinger, U.; Scherer, F.; Bergemann, C.; Remy, J. S.; Krotz, F.; Anton, M.; Lausier, J.; Rosenecker, J. *Biological Chemistry* **2003**, *384*, 737-747.
(42) Kangarlu, A.; Robitaille, P. M. L. *Concepts in Magnetic Resonance* **2000**, *12*, 321-359.
(43) Haik, Y.; Pai, V. N.; Chen, C. J. *Journal of Magnetism and Magnetic Materials* **2001**, *225*, 180-186.
(44) Lu, Y. W.; Ou, Y. Y.; Liu, F. X. *Rare Metals* **2006**, *25*, 493-497.
(45) Drummond, D. C.; Meyer, O.; Hong, K.; Kirpotin, D. B.; Papahadjopoulos, B. *Pharmacol. Rev.* **1999**, *51*, 691-743.
(46) Exerowa, D.; Kaschiev, D.; Platikanov, D. *Adv.Colloid Interface Sci.* **1992**, *40*, 201-256.
(47) Marsh, D.; Watts, A.; Knowles, P. F. *Biochemistry* **1976**, *15*, 3570-3578.

(48) Papahadjopoulos, D.; Jacobson, K.; Nir, S.; Isac, T. *Biochim. Biophys. Acta.* **1973**, *311*, 330-348.
(49) Tamba, Y.; Yamazaki, M. *Biochemistry* **2005**, *44*, 15823-15833.
(50) Inaoka, Y.; Yamazaki, M. *Langmuir* **2007**, *23*, 720-728.
(51) Kohler, N.; Sun, C.; Wang, J.; Zhang, M. *Langmuir* **2005**, *21*, 8858-8864.
(52) Lu, Y.; Yin, Y. D.; Mayers, B. T.; Xia, Y. N. *Nano Letters* **2002**, *2*, 183-186.
(53) Park, K. S.; Tae, J.; Choi, B.; Kim, Y. S.; Moon, C.; Kim, S. H.; Lee, H. S.; Kim, J.; Kim, J.; Park, J.; Lee, J. H.; Lee, J. E.; Joh, J. W.; Kim, S. *Nanomedicine-Nanotechnology Biology and Medicine* **2010**, *6*, 263-276.
(54) Abou-Hassan, A.; Bazzi, R.; Cabuil, V. *Angewandte Chemie-International Edition* **2009**, *48*, 7180-7183.

2 - Methods

2.1 Syntheses of magnetic nanoparticles

Numerous chemical methods can be used to synthesize magnetic nanoparticles: co-precipitation reactions, microemulsions, sol-gel syntheses, sonochemical reactions, hydrothermal and high-temperature reactions, flow injection syntheses and electro-spray syntheses[1].

The first main chemical challenge consists of defining experimental conditions, leading to a monodisperse population of magnetic grains of suitable size. The second critical point is to select a reproducible process that can be industrialized without any complex purification procedure, such as ultracentrifugation, size-exclusion chromatography or magnetic filtration. These methods have been used to prepare particles with homogeneous composition and narrow size distribution.

In this work Cobalt ferrite ($CoFe_2O_4$) NPs stabilized with different coatings were prepared by co-precipitation and sol-gel methods. More details about the syntheses were reported in Chapter 3 about Drug-carriers preparation.

2.1.1 Synthesis by co-precipitation

The co-precipitation technique is probably the simplest and most efficient chemical pathway to obtain magnetic particles.

Metal oxides, such as iron oxide (magnetite, Fe_3O_4) or Cobalt ferrite ($CoFe_2O_4$), have found a high number of applications. Metal oxides

are usually prepared by a stoichiometric mixture of metal salts in aqueous medium, i.e. Fe_3O_4 nanoparticles are prepared by mixing ferrous and ferric salt solutions.

The size, the shape and the composition of the nanoparticles depend on the reaction temperature, the pH value and ionic strength of the media.

The main advantage of the co-precipitation process is that a large amount of nanoparticles can be synthesized. However, the control of particle size distribution is limited, because mainly kinetic factors are controlling the growth of the crystal: in fact, the co-precipitation process consists of two stages, a short burst of nucleation followed by a slow growth of the nuclei by diffusion of the solutes to the surface of the crystal.

Nanoparticles prepared by co-precipitation unfortunately tend to be rather polydisperse. It is well known that short burst nucleation and subsequent slow controlled growth is crucial to produce monodisperse nanoparticles. Controlling these processes is therefore the key in the production of monodisperse metal oxide magnetic nanoparticles. The addition of chelating anions (carboxylate ions, such as citric, gluconic or oleic acid) or polymer surface complexing agents (dextran or polyvinyl alcohol) during the formation of magnetic cores can help to control the size of the nanoparticles. According to the molar ratio between the organic ions and the iron salts, the chelation of these organic ions on the metal oxide surface can either prevent nucleation and then lead to larger particles or inhibit the growth of the crystal nuclei, leading to small nanoparticles.

The first controlled preparation of superparamagnetic iron oxide particles using alkaline precipitation of $FeCl_3$ and $FeCl_2$ was performed by Massart[2]. The parameters of this process were carefully studied to demonstrate the influence of the base (ammonia and NaOH) of the pH value, of cations ($N(CH3)^{4+}$, $CH_3NH_3^+$,Na^+, K^+ and NH_4^+)[3] and the temperature effect[4,5]. When all of these parameters are

modulated, it is possible to obtain particles with a size ranging from 2 to 20 nm. The shape variation is related to the variation of the electrostatic surface density of the nanoparticles.

2.1.2 Synthesis in microemulsion

A microemulsion is a thermodynamically stable isotropic dispersion of two immiscible liquids, where the microdomain of either or both liquids is stabilized by an interfacial film of surfactant molecules[6]. Surfactant molecules may spontaneously form nanodroplets of different sizes, micelles (oil-in-water emulsions, 1-10 nm) or reverse micelle (water-in-oil emulsions, 10-100 nm). Generally reverse micelle are used as nanoreactors for nanoparticle synthesis. In particular, the size of the reverse micelle is determined by the molar ratio of water to surfactant[7] and by the concentration of reactants. By mixing two identical water-in-oil microemulsions containing the desired reactants, the microdroplets will continuously collide, coalesce, and break again, and finally a precipitate forms in the micelles[8]. By the addition of a solvent, such as acetone or ethanol, to the microemulsions, the precipitate can be extracted by filtering or centrifuging the mixture. In this sense, a microemulsion can be used as a nanoreactor for the formation of nanoparticles. The surfactant-stabilized nanoreactor provides a confinement that limits particle nucleation and growth. For this reason the main advantage of microemulsion reaction is the possibility to control the nanoparticle sizes.

Using the microemulsion technique, metal oxide MFe_2O_4 (M: Mn, Co, Ni, Cu, Zn, Mg, or Cd, etc) nanoparticles have been synthesized in reverse micelles of cetyl-trimethylammonium bromide (CTAB), using 1-butanol as co-surfactant and octane as the oil phase.

2.1.3 Sol-Gel synthesis

The sol-gel process is a wet-chemical technique used for the synthesis of nanostructured metal oxides[9]. In this process, the sol (or solution) evolves gradually towards the formation of a gel-like network containing both a liquid phase and a solid phase. Typical precursors are metal alkoxides and metal chlorides, which undergo hydrolysis and polycondensation reactions to form a colloid. The basic structure or morphology of the solid phase can range anywhere from discrete colloidal particles to continuous chain-like polymer networks. The sol-gel approach is a cheap and low-temperature technique that allows for the fine control of the product's chemical composition.

A typical sol-gel process is the hydrolysis of tetraethyl orthosilicate (TEOS) that lead to the formation of SiO_2 in the form of fibers. For this reason, silica shells have been widely used to protect magnetic cores, also preventing the direct contact of the magnetic core with additional agents linked to the silica surface thus avoiding unwanted interactions[10,11]. For instance, the direct attachment of dye molecules to magnetic nanoparticles often results in luminescence quenching. To avoid this problem, a silica shell was first coated on the magnetic core, and then dye molecules were grafted on the silica shell[12]. Silica coatings have several advantages arising from their stability under aqueous conditions (at least if the pH value is sufficiently low), easy surface modification, and easy control of interparticle interactions, both in solution and within structures, through variation of the shell thickness.

2.1.4 Hydrothermal and high temperature synthesis

Hydrothermal syntheses are performed in reactors or autoclaves where the pressure can be higher than 140 bar and the temperature

can be above 200°C[13]. There are two main steps for the formation of metal oxides nanoparticles: hydrolysis and oxidation or neutralization of mixed metal hydroxides. This strategy is based on a general phase transfer and separation mechanism occurring at the interfaces of the liquid, solid and solution phases present during the synthesis. In this process, the reaction conditions, such as solvent, temperature and time have important effects on the products[14]. In the hydrothermal process, the particle size in crystallization is controlled mainly through the rate processes of nucleation and grain growth. Nucleation might be faster than grain growth at higher temperatures and results in a decrease in particle size. On the other hand, prolonging the reaction time would favor grain growth.

Nanoparticles with a high level of monodispersity and size control can be obtained by high temperature decomposition of iron organic precursor in the presence of high boiling organic solvents and stabilizing surfactants[15]. The organometallic precursor include metal acetylacetonates, $(M(acac)_n$, where M = Fe, Mn, Co, Ni, Cr; n = 2 o 3; acac = acetylacetonate), metal cupferronates ($M^x cup_x$, where M= metal ion; cup = N-nitrosophenylhydroxylamine) or carbonyls. Fatty acids, oleic acid and hexadecylammine are often used as surfactants. The size and the morphology of the nanoparticles can be controlled by controlling the reaction times and the temperature, as well as the concentration and ratios of the reactants, nature of the solvent, precursors and complexing strength[16].

2.1.5 Sonochemical and flow-injection syntheses

The sonolysis of aqueous solution of metal salts in the presence of surfactants leads to the formation of stable hydrosol of amorphous metal oxides nanoparticles[17].

The flow-injection synthesis techinque (FIS) consisted of a continuos or segmented mixing of reagents under a laminar flow regime in a capillary reactor[18]. The FIS technique has a high reproducibility

because of the laminar conditions of the flow, a high mixing omogenity and the opportunity for precise and external control of the process.

2.1.6 Stabilization of magnetic nanoparticles

The stabilization of the metal oxide nanoparticles is crucial to obtain magnetic colloidal ferrofluids that are stable against aggregation in both biological medium and a magnetic field. The stability of a magnetic fluid results from the equilibrium between attractive and repulsive forces. Theoretically electrostatic charges and steric repulsion (in the case of non-naked nanoparticles) induce repulsive forces, while van der Waals and magnetic dipolar forces induce, respectively, strong short-range isotropic and anisotropic attractions. Stabilization of magnetic nanoparticles can be achieved by playing on one or both of the two repulsive forces: electrostatic and steric repulsion (Figure 2.1).

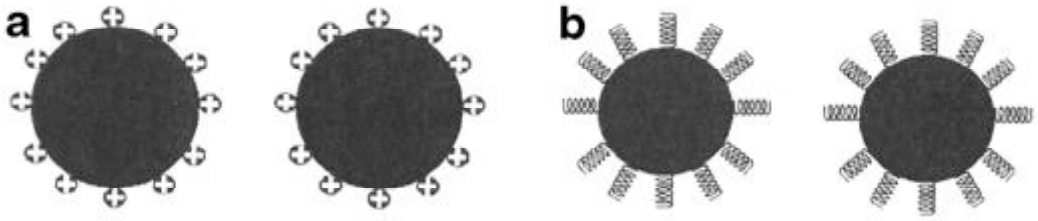

Figure 2.1. (a) Nanoparticles stabilized by electrostatic repulsion; (b) nanoparticles stabilized by steric repulsion.

The electrostatic repulsion can be followed through the knowledge of the diffusion potential, that may close to the zeta potential, and the ionic strength and pH of the solution. In iron oxide, the surface iron atoms act as Lewis acids and coordinate with molecules that donate lone-pair electrons. Therefore, in aqueous solutions, the Fe atoms coordinate with water, which dissociates to leave the iron oxide surface hydroxyl functionalized. These hydroxyl groups may react

with acids or bases. Depending upon the pH of the solution, the surface of the magnetite will be positive or negative. The isoelectric point is observed at pH 6.8. Around this point, point of zero charge (PZC), the surface charge density is too small and the particles are no longer stable in water and flocculate.

The steric force depends upon the coating shell (organic or inorganic compounds, polymer or surfactants) and it is difficult to predict and quantify. It is quite well described for polymers and it depends, among other parameters, upon molecular weight and density[19,20]. Moreover, metal oxide or pure metal nanoparticles are very sensitive to air, therefore it is necessary to develop efficient strategies to improve the chemical stability of magnetic nanoparticles. Generally core-shell structures are used to isolate the magnetic core against the environment and to create repulsive (mainly steric) forces to balance the magnetic and van der Waals attractive forces.

The applied coating strategies can be divided in: coatings with organic shells, including surfactants and polymers, carboxylates, phosphates, sulfates or coatings with inorganic compounds, including silica, carbon or precious metals (Ag or Au).

Some of the main coating stabilizers are reported below:

Monomeric stabilizers (carboxylates, phosphates and sulfates)[21].

In the case of carboxylates, the surface of metal oxide nanoparticles can be stabilized in an aqueous dispersion by the adsorption of citric acid[22]. This acid may be adsorbed on the surface of nanoparticles by coordinating via one or two of the carboxylate functionalities, depending upon steric necessity and the curvature surface. Carboxylates have important effects on the growth of iron oxide nanoparticles and their magnetic properties. Increasing concentration of citric acid caused significant decreases in the cristallinity of the metal oxides and changes in their surface geometry[23]. Similar results have been obtained with other monomeric stabilizers, such as gluconic acid, dimercaptosuccinic acid, oleic acid, lauric acid and

phosphates. According to the used monomeric stabilizer, nanoparticles could be dispersed in aqueous or organic solvents.

Surfactants and Polymers are often employed to passivate the surface of the nanoparticles during and after the synthesis to avoid agglomeration. In general, they can be chemically anchored or physical adsorbed on magnetic nanoparticles to form a single or a double layer. Surfactants, such as tetramethylammonium hydroxide (TMAOH), sodium dodecyl sulfate (SDS), cetyltrimethylammonium bromide (CTAB), are used to achieve stable colloids[24,25]. Polymers containing functional groups, such as carboxylic acids, phosphates and sulfates can bind to the surface of nanoparticles. The common polymer coatings are: dextran, carboxymethylated dextran, carboxydextran, polyvinyl alchol (PVA), polyethylene glycol (PEG), polyoaxamines, alginate, chitosan[26,27].

Inorganic materials (silica or precious metals)[10,11,28]. These coatings provide stabily and help in binding various biological ligands to the surface of nanoparticles. Silica coating, previously discussed in sol-gel synthesis, stabilizes nanoparticles in two different ways. One is by shielding the magnetic dipole interaction with the silica shell; on the other hand, silica is negative charged and can enhance the Coloumb repulsion of the magnetic nanoparticles.

Precious metals can be deposited on magnetic nanoparticles through reactions in microemulsion, redox transmetallation or other methods[29]. Gold seems to be an ideal coating owing to its low reactivity. However it was found that the direct coating of magnetic nanoparticles with gold is very difficult.

2.2 Preparation of lipid vesicles

Various types of phospholipid vesicles (MLV, SUV, LUV, GUV) can be prepared by different methods implying different mechanisms in the liposome formation. The most common methods are:

- Hydration for multilamellar vesicles (MLV)
- Sonication for small unilamellar vesicles (SUV)
- Extrusion for large unilamellar vesicles (LUV)
- Electroformation for giant unilamellar vesicles (GUV)

Lipid vesicles are formed when thin phospholipid films are hydrated and stacks of liquid crystalline bilayers become fluid and swell. The hydrated lipid sheets detach during agitation and self-close to form large, multilamellar vesicles (MLV) which prevents interaction of water with the hydrocarbon core of the bilayer at the edges. Once MLV have formed, SUV and LUV can be produced reducing the vesicle sizes as reported in Figure 2.2.

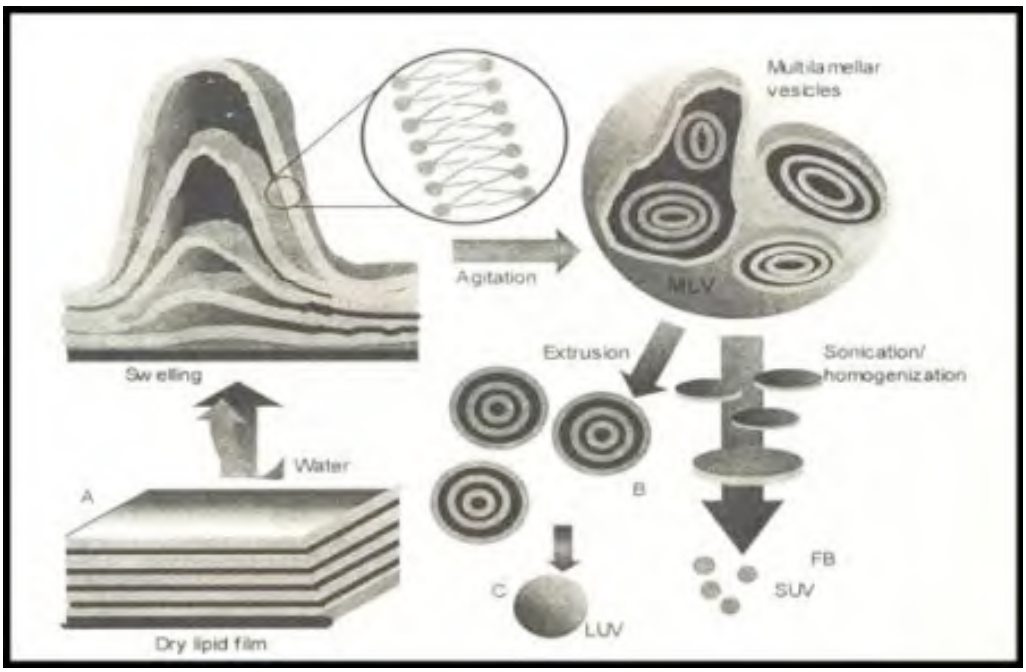

Figure 2.2. Schematic of liposome preparation

Hydration for MLV preparation consists on lipid dissolution in an organic solvent (generally chloroform or chloroform:methanol mixtures) to assure a homogeneous mixture of lipids. Once the lipids are mixed in the organic solvent, the solvent is removed to yield a lipid film. For small volumes of organic solvent (<1mL), the solvent may be evaporated using a dry nitrogen or argon stream; for larger volumes, the organic solvent should be removed by rotary evaporation yielding a thin lipid. The lipid film is dried to remove residual organic solvent under vacuum and then hydrated with an aqueous solution. The temperature of the hydrating medium should be above the gel-liquid crystal transition temperature (Tm) of the lipid and should be maintained during the entire hydration period. Swelling of the lipid film under vigorous agitation lead to the formation of a milky suspension of heterogeneous large MLV (the size distribution of this vesicle population is around several microns). MLV are structures analogous to onions, with each lipid bilayer separated by a water layer. The spacing between lipid layers is dictated by composition and charge of the lipid.
Once these multilamellar vesicles have formed, reducing the size of the vesicles (SUV and LUV) requires energy input in the form of sonic energy (sonication) or mechanical energy (extrusion).

Sonication causes the disruption of MLV suspensions producing small, unilamellar vesicles (SUV) with diameters in the range of 15-50nm. The most common instrumentations for preparation of sonicated vesicles are bath and probe tip sonicators. Probe tip sonicators deliver high-energy input to the lipid suspension but suffer from overheating of the solution causing phospholipid degradation, the sonication tips also tend to release titanium particles into the lipid suspension, which must be removed by centrifugation. For these reasons, bath sonicators are the most

widely used. Since it is nearly impossible to reproduce the conditions of sonication, size variation between batches produced at different times is not uncommon. Also, due to the high degree of curvature of these membranes, SUV are unstable and will spontaneously fuse to form larger vesicles when stored below their phase transition temperature.

Extrusion is a technique in which a lipid suspension is forced through a polycarbonate filter with a defined pore size to yield particles having a diameter near the pore size of the filter used. Prior to extrusion through the final pore size, MLV suspensions are disrupted either by several freeze-thaw cycles or by prefiltering the suspension through a large pore size filter. As with all procedures for downsizing vesicle dispersions, the extrusion should be done at a temperature above the T_m of the lipid. Extrusion through filters with 100nm pores typically yields large unilamellar vesicles (LUV) with a mean diameter of 120-140nm. Mean particle size also depends on lipid composition and it is quite monodisperse and reproducible from batch to batch.

Electroformation is a useful method for the formation of cell-size lipid membrane vesicles or GUV with diameters between 1 and 100 μm, used as model in studies of the basic properties of the cell membrane and the functions of biomolecules. This method was first developed by Angelova and Dimitrov and has become widely used for preparing GUV[30,31].

In the conventional electroformation method a lipid film is dried on the conductive surface of one or both electrodes of Indium Tin Oxide (ITO)-coated coverslips positioned parallel to each other. The reason for using ITO as an electrode is its transparency, so that the formation of giant vesicles could be easily observed using a microscope. The application of a low-voltage AC electric field

(generally a sinusoidal wave with a frequency of 10 Hz and amplitude of 2 V) induces the formation of GUV upon swelling of a lipid hydrated with an aqueous buffer. The disadvantage of this method is that GUV yield and size decrease strongly when ions (salt) are present in the aqueous solution.

In this work GUVs were prepared by using a homemade chamber (see Figure 2.3) obtained by assembling two Indium Tin Oxide (ITO)-coated microscope slides separated by an O-ring spacer. The electrical connection with either side of the capacitor was obtained by directly attaching two Cu stickers on the conducting faces.

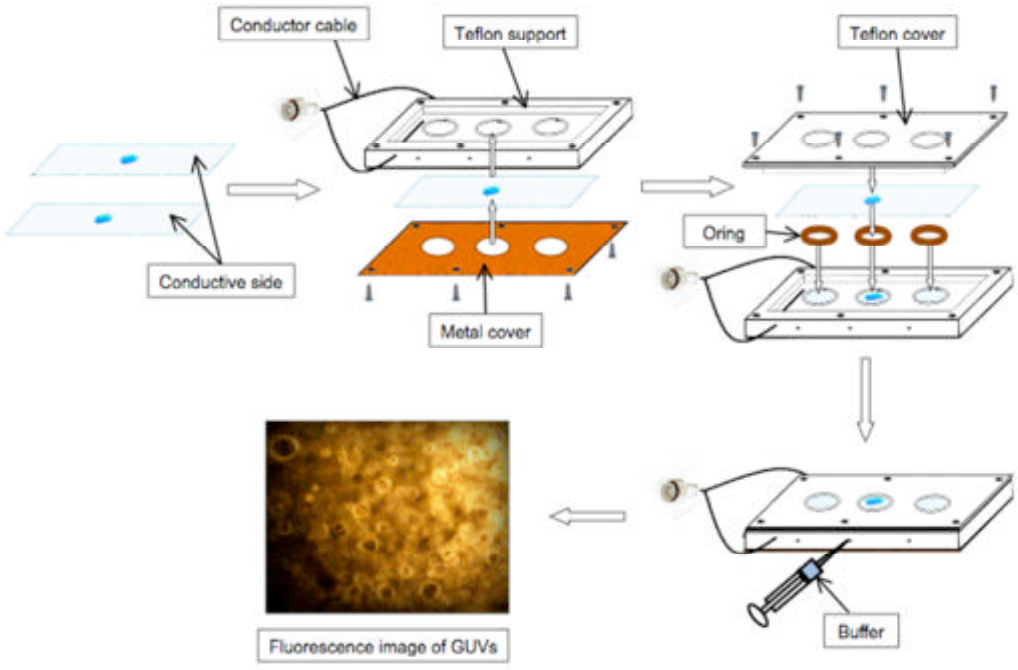

Figure 2.3. Home-made chamber for GUVs preparation by electroformation method.

2.3 Small Angle Scattering (SAS)

Small angle scattering (SAS) is the collective name given to the techniques of small angle neutron (SANS), X-Ray (SAXS) and light (LS) scattering. In each of these techniques radiation is elastically scattered by a sample and the resulting scattering pattern is analyzed to provide information about the size and shape of some component of the sample. The type of sample that can be studied by SAS, the sample environment, the length scale and the information that can ultimately be obtained, all depend on the nature of the radiation employed. For example, LS cannot be used to study optically opaque samples and SAXS cannot be employed to study large particles or complexes samples. However, these techniques have some similarities, for example the fact that, with minor adjustments to account for the different types of radiation, the same basic equations or "laws" can be used to analyse data. In Table 2.1 I have summarized the main features of these techniques, and we can see that they are sensible to different aspects of the investigated molecules, therefore they investigate different sizes of matter.

Table 2.1 Small Angle Scattering techniques

Radiation	***X-Rays***	***Neutron***	***Light (laser)***
Wavelength	1-50 nm	10-150 nm	100-1000 nm
Sensible to	Electron density	Nuclear density	Refractive index
Technique	SAXS	SANS	LS
Sample thick	1-2 mm	1-2 mm	1-10 mm

In any SAS experiment, a beam of collimated radiation is directed at a sample, illuminating a small volume, V. Some of the incident

radiation is transmitted by the sample, some is adsorbed and some is scattered. In SAS experiments, the detector measures the intensity of the radiation, I(Q), scattered by a collection of uniform particle.

The quantity colloquially referred to as “the scattering vector”, Q, is the modulus of the resultant between the incident, ki, and the scattered, ks, wavevectors, see Figure 2.4, and is given by:

$$|Q| = |k_f - k_i| = \frac{4\pi n}{\lambda}\sin(\theta/2) \qquad (2.1)$$

where Q is normally quoted in $Å^{-1}$, θ/2 is the scattering angle, n is the refractive index.

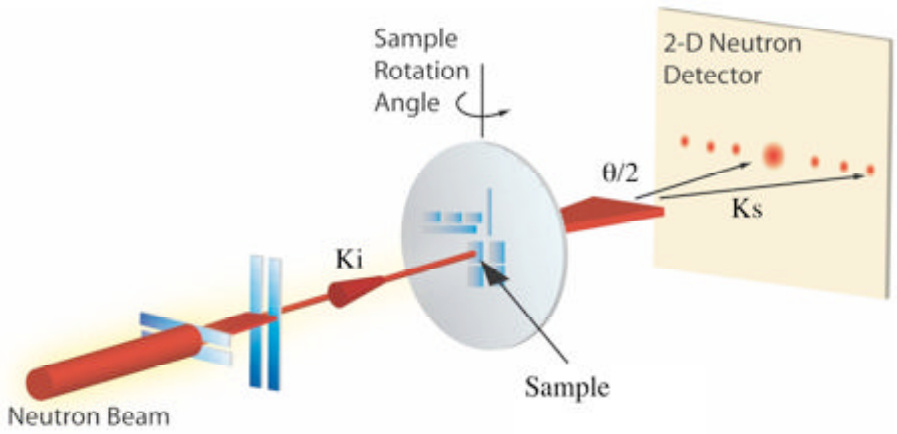

Figure 2.4. Scheme of a SAS experiment

In this section the SAS techniques used for the particles characterization are outlined: Small Angle X-Rays Scattering (SAXS) and Dynamic Light Scattering (DLS).

2.3.1 Small Angle X-Rays Scattering (SAXS)

SAXS is a small angle scattering technique where the elastic scattering of X-rays by a sample is recorded at very low angles (typically 0.1-10°). In this angular range, information about the averaged particle sizes, shapes, distributions and orientation of samples are contained. The analyzed materials can be solid or liquid and include colloids of all types, metals, cements, oil, polymers, proteins etc. The method is accurate, non-destructive and requires only a minimum of sample preparation.

In a SAXS instrument a monochromatic beam of X-rays is brought to a sample from which some of the X-rays scatter, while most simply go through the sample without interacting with it. The scattered X-rays form a scattering pattern detected at a detector situated behind the sample perpendicular to the direction of the primary beam that initially hit the sample. The scattering pattern contains the information on the structure of the sample. The major problem that must be overcome in SAXS instrumentation is the separation of the weak scattered intensity from the strong main beam. The smaller the desired angle, the more difficult this becomes. The problem is comparable to one encountered when trying to observe a weakly radiant object close to the sun, like the sun's corona. Likewise, in SAXS the non-scattered beam that merely travels through the sample must be blocked, without blocking the closely adjacent scattered radiation. Most available X-ray sources produce divergent beams and this compounds the problem. In principle the problem could be overcome by focusing the beam, but this is not easy when dealing with X-rays and was previously not done except on synchrotrons where large bent mirrors can be used. This is why most laboratory small angle devices rely on collimation instead.

In SAXS experiments, the measured intensity of the radiation, I(Q), scattered by a collection of uniform particles is given by[32]:

$$I(Q) = A \cdot \phi \cdot P(Q) \cdot S(Q) + I_{bkg} \qquad (2.2)$$

where A is the amplitude accounting for the instrumental factor, ϕ is the particle volume fraction, P(Q) is the particles form factor, S(Q) is the interparticle structure factor accounting for the interparticle correlations, I_{bkg} is the incoherent background and Q is the scattering vector.

The *contrast term* is the difference of scattering lenght density (SLD) values between the part of the sample and the surrounding medium, and in SAXS it arises out of the differences in electron density.

The *form factor,* P(Q), is a function that describes how the scattering vector, Q, is modulated by interference effects between radiation scattered by different parts of the same scattering body; consequently it is very dependent on the shape of the scattering body. Fortunately analytic expressions exist for most common shapes and expressions for more complexes topologies can usually be deduced from these.

The *interparticle structure factor,* S(Q), is a function that describes how Q is modulated by interference effects between radiation scattered by different scattering bodies; consequently it dependent on the degree of local order in the sample and on the sample concentration. Generally, for diluted system, S(Q) can be discarded and considered equal to 1.

SAXS measurements were carried out with a HECUS SWAX-camera (Kratky) equipped with a position-sensitive detector (OED 50 M) containing 1024 channels of width 54 μm. CuK_α radiation of wavelength 1.542 Å has been obtained using a X-ray generator (Seifert ID-3003), operating at a maximum power of 2 kW. A 10 μm thick nickel filter was used to remove CuK_α radiation. The volume between the sample and the detector was kept under vacuum (P < 1 mBar) during measurements to minimize scattering from air. The liquid samples were filled into 1 mm quartz capillary and then sealed. Measurements were done at 25°C and temperature was controlled by a Peltier element, with an accuracy of ± 0.1 °C. All scattering curves

were corrected for the solvent contribution. The data were slit desmeared by a linear method[33].

2.3.2 Dynamic Light Scattering (DLS)

DLS is one of the most popular methods used to determine the size of particles. When light hits small particles, the light scatters in all directions (Rayleigh scattering) so long as the particles are small compared to the wavelength. If the light source is a laser, and thus is monochromatic and coherent, then one observes a time-dependent fluctuation in the scattering intensity. These fluctuations are due to the fact that the small molecules in solutions are undergoing Brownian motion and so the distance between the scatterers in the solution is constantly changing with time. This scattered light then undergoes either constructive or destructive interference by the surrounding particles and within this intensity fluctuation.

There are several ways to derive dynamic information about particles' movement in solution by Brownian motion. One such method is dynamic light scattering (DLS), also known as quasi-elastic laser light scattering (QELS). The dynamic information of the particles is derived from an autocorrelation of the intensity trace recorded during the experiment. The second order autocorrelation curve is generated from the intensity trace as follows:

$$g^2(q,t) = \frac{\langle I(t)I(t+\tau)\rangle}{\langle I(t)\rangle^2} \qquad (2.3)$$

where $g^2(q, \tau)$ is the autocorrelation function at a particular wave vector, q, and delay time, τ, and I is the intensity. At short time delays, the correlation is high because the particles do not have a chance to move to a great extent from the initial state that they were in. The two signals are thus essentially unchanged when compared after only a very short time interval. As the time delays become

longer, the correlation starts to exponentially decay to zero, meaning that after a long time period has elapsed, there is no correlation between the scattered intensity of the initial and final states. This exponential decay is related to the motion of the particles, specifically to the diffusion coefficient. To fit the decay (i.e., the autocorrelation function), numerical methods are used, based on calculations of assumed distributions. If the sample is monodisperse then the decay is simply a single exponential. The Siegert equation relates the second order autocorrelation function with the first order autocorrelation function $g^1(q;\tau)$ as follows:

$$g^2(q,\tau) = 1 + \beta\left[g^1(q,t)\right]^2 \qquad (2.4)$$

where the parameter β is a correction factor that depends on the geometry and alignment of the laser beam in the light scattering setup.

Once the autocorrelation data have been generated, different mathematical approaches can be employed to determine size and polydispersity of particles from it. Analysis of the scattering is facilitated when particles do not interact through collisions or electrostatic forces between ions. Particle-particle collisions can be suppressed by dilution, and charge effects are reduced by the use of salts to collapse the electrical double layer.

The simplest approach is to treat the first order autocorrelation function as a single exponential decay. This is appropriate for a monodisperse population.

$$g^1(q,\tau) = \exp(-\Gamma\tau) \qquad (2.5)$$

where Γ is the decay rate. The translational diffusion coefficient D_t may be derived at a single angle or at a range of angles depending on the scattering wave vector q (defined in equation 2.1).

$$\Gamma = q^2 D_t \qquad (2.6)$$

The diffusion coefficient D_t provide access to the hydrodynamic correlation lengths R_H for isotropic particles through the Stokes-

Einstein relationship:

$$D_t = \frac{k_B T}{6\pi\eta_s R_H} \qquad (2.7)$$

where η_S is the solvent viscosity and k_B the Boltzmann constant.

It is important to note that the size determined by dynamic light scattering is the size of a sphere that moves in the same manner as the scatterer. So, for example, if the scatterer is a random coil polymer, the determined size is not the same as the radius of gyration determined by static light scattering. It is also useful to point out that the obtained size will include any other molecules or solvent molecules that move with the particle. In most cases, samples are polydisperse. Thus, the autocorrelation function is a sum of the exponential decays corresponding to each of the species in the population.

One of the most common methods to fit DLS autocorrelation functions is the *Cumulant method,* from which in addition to the sum of the exponentials above, more information can be derived about the polidispersity of the system as follows:

$$g^1(q,\tau) = \exp(-\Gamma\tau)(1 + \frac{\mu_2}{2!}\tau^2 - \frac{\mu^3}{3!}\tau^3 + ...) \qquad (2.8)$$

where $\frac{\mu_2}{2!}\tau^2$ is the second order polydispersity index.

An alternative method for analyzing the autocorrelation function can be achieved through an inverse Laplace transform known as CONTIN[34].The CONTIN analysis is ideal for polydisperse and multimodal systems.

DLS experiments were carried out on a Brookhaven Instrument apparatus, New York, USA (BI 9000 AT correlator card and BI 200 SM goniometer). The signal is detected by an EMI 9863B/350 photomultiplier. The light source was the doubled frequency of a Coherent Innova diode pumped Nd-YAG laser, (λ=532 nm, 20 mW), or

alternatively a JDS Uniphase He-Ne (λ=633 nm, 5 mW). The laser long term power stability was ± 0.5%. Self-beating detection was recorded using decahydronaphthalene (thermostated by a water circulating system) as index matching liquid. A temperature probe was inserted in the sample while simultaneously recording autocorrelation functions. Measurements have been performed at 25°C on 0.5 ml samples previously transferred into cylindrical Hellma scattering cells. For each sample at least three separate measurements were performed at the scattering angle θ = 90° corresponding to the scattering vector q. Data analysis has been performed according to standard procedures, and interpreted through a cumulant expansion of the field autocorrelation function, arrested to the second order. Moreover, in order to obtain a distribution w(Γ) of decay rates, a constrained regularization method, CONTIN, developed by Provencher, was used to invert the experimental data.

2.4 Microscopy

Microscopy is the technical field of using microscopes to view samples or objects that cannot be seen with the unaided eye (objects that are not within the resolution range of the normal eye). There are three well-known branches of microscopy: optical, electron, and scanning probe microscopy. Optical and electron microscopy involve the diffraction, reflection, or refraction of electromagnetic radiation/electron beams interacting with the subject of study, and the subsequent collection of this scattered radiation in order to build up an image. This process may be carried out by wide-field irradiation of the sample (for example standard light microscopy and transmission electron microscopy) or by scanning of a fine beam over the sample (for example confocal laser scanning microscopy and scanning electron microscopy).

In the following paragraphs the principles of Confocal Laser Scanning Microscopy (CLSM) are reported, because this technique was widely used for the experiments performed in this work. Moreover some information about Transmission Electron Microscopy (TEM) are reported.

2.4.1 Confocal Laser Scanning Microscopy (CLSM)

Laser scanning confocal microscopy has become an invaluable tool for a wide range of investigations in the biological and medical sciences for imaging thin optical sections in living and fixed specimens ranging in thickness up to 100 micrometers. CLSM is a technique for obtaining high-resolution optical images with depth selectivity. The key feature of confocal microscopy is its ability to

acquire in-focus images from selected depths, a process known as optical sectioning. Images are acquired point-by-point and reconstructed with a computer, allowing three-dimensional reconstructions of topologically-complex objects. The principle of CLSM was developed by Marvin Minsky in 1957, but it took another thirty years and the development of lasers for CLSM to become a standard technique toward the end of the 1980s. In 1978, Thomas and Christoph Cremer designed a laser scanning process, which scans the three dimensional surface of an object point-by-point by means of a focused laser beam, and creates the over-all picture by electronic means similar to those used in scanning electron microscopes. This CLSM design combined the laser scanning method with the 3D detection of biological objects labeled with fluorescent markers for the first time.

In a conventional light microscope, object-to-image transformation takes place simultaneously and parallel for all object points. By contrast, the specimen in a CLSM is irradiated in a point-wise fashion, i.e. serially, and the physical interaction between the laser light and the specimen detail irradiated (e.g. fluorescence) is measured point by point. To obtain information about the entire specimen, it is necessary to guide the laser beam across the specimen, or to move the specimen relative to the laser beam, a process known as scanning. To obtain images of microscopic resolution from a CLSM, a computer and dedicated software are indispensable.

The principle of CLSM is diagrammatically presented in Figure 2.5. Coherent light emitted by the laser system (excitation source) passes through a pinhole aperture that is situated in a conjugate plane (confocal) with a scanning point on the specimen and a second pinhole aperture positioned in front of the detector (a photomultiplier tube). As the laser is reflected by a dichromatic mirror and scanned across the specimen in a defined focal plane, secondary fluorescence

emitted from points on the specimen (in the same focal plane) pass back through the dichromatic mirror and are focused as a confocal point at the detector pinhole aperture.

Only a small fraction of the out-of-focus fluorescence emission is delivered through the pinhole aperture, most of this extraneous light is not detected by the photomultiplier and does not contribute to the resulting image. Refocusing the objective in a confocal microscope shifts the excitation and emission points on a specimen to a new plane that becomes confocal with the pinhole apertures of the light source and detector.

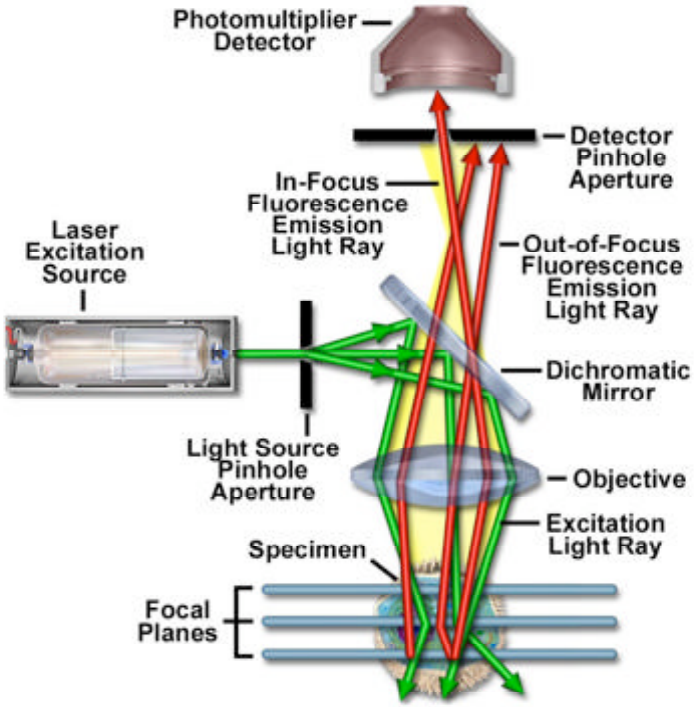

Figure 2.5. Schematic diagram of the optical pathway and principal components of CLSM.

With a CLSM it is possible to exclusively image a thin optical slice out of a thick specimen (typically, up to 100 μm), a method known as optical sectioning. Under suitable conditions, the thickness (Z dimension) of such a slice may be less than 500 nm.

A CLSM can therefore be used to advantage especially where thick

specimens (such as biological cells in tissue) have to be examined by fluorescence. The possibility of optical sectioning eliminates the drawbacks attached to the observation of such specimens by conventional fluorescence microscopy.

In addition to the possibility to observe a single plane (or slice) of a thick specimen in good contrast, optical sectioning allows a great number of slices to be cut and recorded at different planes of the specimen, with the specimen being moved along the optical axis (Z) by controlled increments.

The result is a 3D data set, which provides information about the spatial structure of the object. The quality and accuracy of this information depend on the thickness of the slice and on the spacing between successive slices.

Another field of growing importance is the investigation of living specimens that show dynamic changes even in the range of microseconds. Here, the acquisition of time-resolved confocal image series (known as time series) provides a possibility of visualizing and quantifying the changes.

In this work confocal images of fluorescent GUVs were acquired using a DMIRE2 Confocal Microscope (Leica TCS SP2) with argon ion lasers (λ=488 nm and 514 nm, 30mW at 30% of maximum power) and a water immersion objective 63x/1.2W (Zeiss). The samples were placed in home-made cells, where the bottom plate was a microscopy coverglass (LAB-TEC, 8 Well) and the cell wall was a cylinder of glass (diameter 8 mm, height 1.5 cm). All leakage experiments were quantitatively analyzed by measuring the change in fluorescence intensity of the probe (Alexa 488-maleimide) in the aqueous pool inside the GUVs during the exposure to an AC-magnetic field.

2.4.2 Transmission Electron Microscopy (TEM)

The transmission electron microscope (TEM) operates on the same basic principles as the light microscope but uses electrons instead of

light. What you can see with a light microscope is limited by the wavelength of light. TEM use electrons as "light source" and their much lower wavelength makes it possible to get a resolution a thousand times better than with a light microscope. It is possible to see objects to the order of a few Angstrom (10^{-10} m). For example, one can study small details in the cell or different materials down to near atomic levels, making TEM a valuable tool in both medical, biological and materials research. A "light source" at the top of the microscope emits the electrons that travel through vacuum in the column of the microscope. Instead of glass lenses focusing the light in the light microscope, TEM uses electromagnetic lenses to focus the electrons into a very thin beam. The electron beam then travels through the specimen you want to study. Depending on the density of the material present, some of the electrons are scattered and disappear from the beam. At the bottom of the microscope the unscattered electrons hit a fluorescent screen, which gives rise to a "shadow image" of the specimen with its different parts displayed in varied darkness according to their density. The image can be studied directly by the operator or photographed with a camera.

TEM investigations have been carried out using a Philips CM 12 operating at acceleration voltages up to 120 kV, equipped with an Olympus MegaViewG2 side-mounted CCD camera. Magnetic nanoparticle samples were prepared by placing a drop of the suspension on a carbon-coated copper grid with a carbon membrane film and removing the excess solvent with a filter paper.

2.5 Fluorescence Spectroscopy

Fluorescence is a spectrochemical method of analysis where the molecules of the analyte are excited by irradiation at a certain wavelength and emit radiation of a different wavelength. The emission spectrum provides information for both qualitative and quantitative analysis.

In this work, fluorescence spectroscopy was used to investigate the release behaviour of the fluorescent molecule Carboxyfluorescein (CF) embedded in magnetoliposomes. Steady-state fluorescence was measured with a LS50B spectrofluorimeter (Perkin Elmer, Italy). The emission fluorescence spectra of CF were recorded between 500 and 610 nm in the corrected spectrum mode with excitation wavelength set at 492 nm and 2.5 nm slit. At least 5 scans were averaged for each spectrum. Magnetoliposomes and control solutions (diluted 1:150 with the isotonic buffer) were measured, before and after LF-AMF exposure, at regular time intervals. The release behaviour was checked in time-drive modality by measuring the fluorescence intensity every 10 min during 15 hours. Fluorescence experiments were also performed on magnetoliposomes and control liposomes kept at the highest temperature reached during the treatment, for the same exposure time. All samples were diluted to the measurement concentration with a solution of Triton X-100 to achieve complete release of CF through vesicles disruption. The release percentage was calculated from the fluorescence intensity as:

$$\%\mathrm{Re}\,lease = \frac{I_{ML}(t) - I_{ML}(0)}{I_{MAX} - I_{ML}(0)} \times 100 \qquad (2.9)$$

where $I_{ML}(t)$ is the measured fluorescence intensity, $I_{ML}(0)$ is the fluorescence intensity of the untreated sample, and I_{MAX} is the maximum fluorescence emission with Triton X-100 addition.

2.6 Differential Scanning Calorimetry (DSC)

Differential scanning calorimetry (DSC) is a thermo-analytical technique in which the difference in the amount of heat required to increase the temperature of a sample and reference is measured as a function of temperature. Both the sample and reference are maintained at nearly the same temperature throughout the experiment. The reference sample should have a well-defined heat capacity over the range of temperatures to be scanned. DSC has been of primary importance in studies of lipid phase transitions in model and biological membranes. The basic principle underlying this technique is that, when the sample undergoes a physical transformation such as phase transitions, more or less heat will need to flow to it than the reference to maintain both at the same temperature. Whether less or more heat must flow to the sample depends on whether the process is exothermic or endothermic. For example, as a solid sample melts to a liquid it will require more heat flowing to the sample to increase its temperature at the same rate as the reference. This is due to the absorption of heat by the sample as it undergoes the endothermic phase transition from solid to liquid. Likewise, as the sample undergoes exothermic processes (such as crystallization) less heat is required to raise the sample temperature. By observing the difference in heat flow between the sample and reference, differential scanning calorimeters are able to measure the amount of heat absorbed or released during such transitions. DSC curves can be used to calculate enthalpies of transitions by integrating the peak corresponding to a given transition. It can be shown that the enthalpy of transition can be expressed using the following equation:

$$\Delta H = KA \qquad (2.10)$$

where ΔH is the enthalpy of transition, K is the calorimetric constant, and A is the area under the curve. The calorimetric constant will vary from instrument to instrument, and can be determined by analyzing a well-characterized sample with known enthalpies of transition.

The transition temperature, associated to gel/fluid transition of the lipid bilayer of liposomes, was determined by differential scanning calorimetry measurements performed using a DSC Q2000 from TA Instruments. Heating scans were performed on both liposomes and magnetoliposomes solutions (25 mg/L of lipid) in hermetically closed aluminum pans, in the temperature range from –40 to 25°C at 1°C/min, in order to detect possible differences associated to different lipid packing and bilayer viscosity due to the presence of nanoparticles. Moreover the liposomes and magnetoliposomes solutions, previously exposed to LF-AMF, have been analyzed every two hours with the same heating scan in order to clarify the effect of the nanoparticles on the lipid bilayers upon the application of a magnetic field.

2.7 Attenuated Total Reflection Infrared Spectroscopy (ATR-FTIR)

An ATR-FTIR apparatus operates by measuring the changes that occur in a totally internally reflected infrared beam when the beam comes into contact with a sample. An infrared beam is directed onto an optically dense crystal with a high refractive index at a certain angle. This internal reflectance creates an evanescent wave that extends beyond the surface of the crystal into the sample held in contact with the crystal. It can be easier to think of this evanescent wave as bubble of infrared that sits on the surface of the crystal. This evanescent wave protrudes only a few microns beyond the crystal surface and into the sample. Consequently, there must be good contact between the sample and the crystal surface. In regions of the infrared spectrum where the sample absorbs energy, the evanescent wave will be attenuated or altered. The attenuated energy from each evanescent wave is passed back to the IR beam, which then exits the opposite end of the crystal and is passed to the detector in the IR spectrometer. The system then generates an infrared spectrum. Generally diamond is by far the best ATR crystal material because of its robustness and durability.

In this work IR spectra were collected with a Nexus 870 spectrophotometer (Thermo Nicolet, Paris, France) equipped with a liquid nitrogen-cooled Mercury Cadmium Telluride detector and a single reflection diamond crystal ATR unit (Golden Gate, Specac, UK). All spectra were performed at room temperature with 4 cm^{-1} resolution and averaging 256 scans. The reference spectra, in this case water, were subtracted from the absorbance spectra of the investigated samples.

2.8 Magnetic field generator

A sinusoidal adjustable magnetic field was generated in the gap of a broken ferrite ring carrying a solenoid through which an alternating electric current (AC) from a tone generator was led (Figure 2.6). Samples to be treated with LF-AMF were placed in the middle of the gap within 1 cm cylindrical quartz cells. Due to the design of the experimental apparatus, the magnetic field inside the cell is not isotropic. In fact magnetic field values at different positions of the broken toroidal magnet used to apply the LF-AMF were measured by means of a GM-07 Gaussmeter (HIRST Magnetic Instruments Ltd, UK). Since the measured magnetic fields are different, the sample undergoes magnetic field gradients that cannot be avoided.

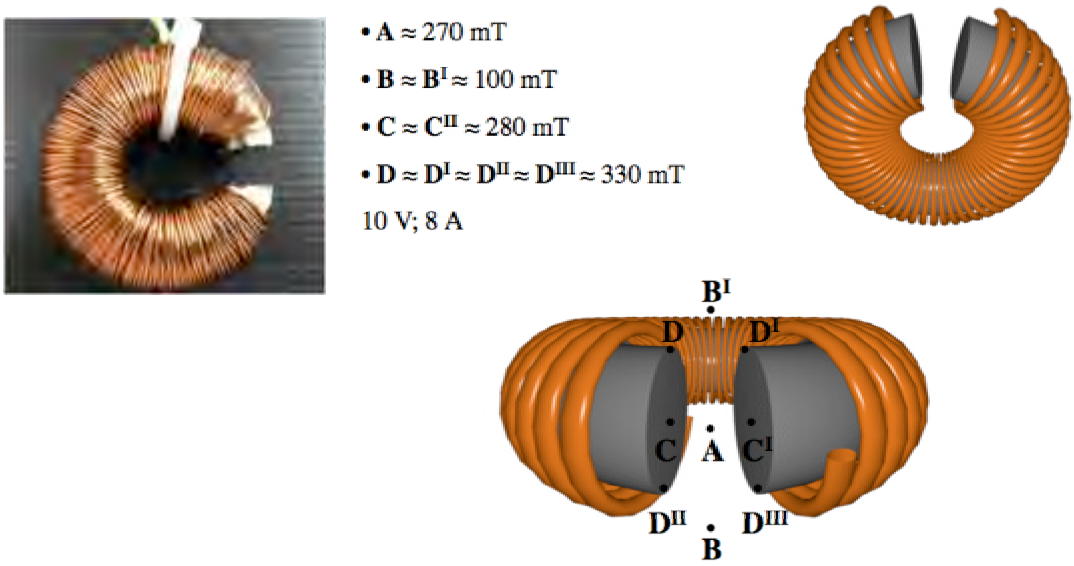

Figure 2.6. Picture of the broken toroidal magnet used to apply the LF-AMF. Magnetic field values at different positions of the broken toroidal magnet.

2.9 Magnetic measurements: SQUID

Magnetic properties of the investigated samples where determined by SQUID (Superconducting Quantum Interference Device), which is a very sensitive magnetometer used to measure extremely weak magnetic fields. SQUID is a simple and rapid way to estimate the *blocking temperature* and the *magnetism* of a sample.

The *blocking temperature* is determined by a zero field cooled/field cooled procedure: the sample is cooled from room temperature in a zero magnetic field (ZFC) and in a magnetic field (FC). Then a small magnetic field is applied (about 100 Oe) and the magnetization is recorded on warming. As temperature increases, the thermal energy disturbs the system and more moments acquire the energy to be aligned with the external field direction. The number of unblocked, aligned moments reaches a maximum at the blocking temperature. Above the blocking temperature the thermal energy is strong enough to randomize the magnetic moments leading to a decrease in magnetization. The blocking temperature is the temperature corresponding to the contact point between the ZFC and FC curves.

The *magnetic properties* of a material can be determined from its hysteresis loop. A hysteresis loop shows the relationship between the induced magnetic flux density (B) and the magnetizing force (H). An example hysteresis loop is shown in Figure 2.7.

The loop is generated by measuring the magnetic flux of a material while the magnetizing force is changed. As the line demonstrates, the greater the amount of current applied (H+), the stronger the magnetic field in the component (B+). At point **a** almost all of the magnetic domains are aligned and an additional increase in the magnetizing force will produce very little increase in magnetic flux. The material has reached the point of magnetic saturation. When H is reduced to

zero, the curve will move from point **a** to point **b.** At this point, it can be seen that some magnetic flux remains in the material even though the magnetizing force is zero. This is referred to as the point of *retentivity* on the graph and indicates the remanence or level of residual magnetism in the material. As the magnetizing force is reversed, the curve moves to point **c**, where the flux has been reduced to zero. This is called the point of *coercivity* on the curve. The force required to remove the residual magnetism from the material is called the coercive force or coercivity of the material.

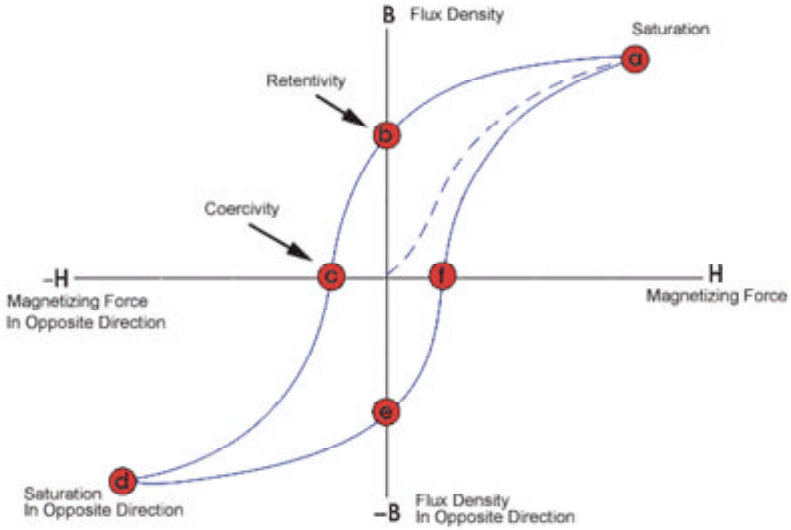

Figure 2.7. Hysteresis loop of a magnetic material

As the magnetizing force is increased in the negative direction, the material will again become magnetically saturated but in the opposite direction (point **d**). Reducing H to zero brings the curve to point **e**. It will have a level of residual magnetism equal to that achieved in the other direction. Increasing H back in the positive direction will return B to zero. Notice that the curve did not return to the origin of the

graph because some force is required to remove the residual magnetism. The curve will take a different path from point **f** back to the saturation point where it completes the loop.

AC susceptibility measurements give information about magnetization dynamics in function of temperature and at different magnetic field oscillating frequencies. In AC magnetic measurements, a small AC drive magnetic field is superimposed on the DC field, causing a time-dependent moment in the sample. The field of the time-dependent moment induces a current in the pickup coils, allowing measurement without sample motion. The detection circuitry is configured to detect only in a narrow frequency band, normally at the fundamental frequency (that of the AC drive field).

The AC magnetic susceptibility measurement yields two quantities: the magnitude of the susceptibility, χ, and the phase shift, φ (relative to the drive signal). Alternately, one can think of the susceptibility as having an in-phase, or real, component χ', and an out-of-phase, or imaginary, component χ''. The two representations are related by:

$$\chi' = \chi \cos\varphi \qquad (2.11)$$

$$\chi'' = \chi \sin\varphi \qquad (2.12)$$

The imaginary component, χ'', indicates dissipative processes in the sample.

In conductive samples, the dissipation is due to eddy currents.

Relaxation and irreversibility in spin-glasses give rise to a nonzero χ''.

In ferromagnets, a nonzero imaginary susceptibility can indicate irreversible domain wall movement or absorption due to a permanent moment. Also, both χ' and χ'' are very sensitive to thermodynamic phase changes, and are often used to measure transition temperatures.

Magnetic measurements on nanoparticles and magnetoliposomes were performed with a MPMS SQUID magnetometer (Quantum Design, San Diego, USA) mounting a liquid helium cryostat able to

cool the sample down to 1.8 K and a superconducting coil magnet capable of reaching 6 T static magnetic field. All static magnetization measurements were carried out on water dispersions of the samples; magnetization curves were recorded at 2.5 K and 300 K. The data were corrected for the diamagnetic contribution of the solvent and of the sample holder, which were separately measured.

AC susceptibility measurements were carried out in the 1-1000 Hz frequency range and performed both on pressed pellets of solid Cobalt ferrite NPs and on water solution of magnetoliposomes.

2.10 Inductively coupled plasma–atomic emission spectrometry (ICP-AES)

A VARIAN 720 OES inductively coupled plasma optical emission spectrometer (ICP-AES) was used for the determination of iron and Cobalt content (ppm) inside magnetoliposomes. The samples were diluted from 0.1 ml to 5.0 ml in 0.1% nitric acid. Calibration curves of standard solutions of iron and Cobalt have been used. The ICP-AES was programmed to detect Co (238.892; 228.615; 230.786 nm) and Fe (238.204; 259.940; 234.350 nm) and to give the average value of the obtained results for each metal. An internal standard of Ge 5 ppm (209.426 nm) has been used to correct for matrix effects.

2.11 References

(1) Laurent, S.; Forge, D.; Port, M.; Roch, A.; Robic, C.; Elst, L. V.; Muller, R. N. *Chemical Reviews* **2008**, *108*, 2064-2110.
(2) Massart, C. R. *IEEE Trans. Magn.* **1981**, *17*, 1247-1248.
(3) Massart, R.; Cabuil, V. *Journal De Chimie Physique Et De Physico-Chimie Biologique* **1987**, *84*, 967-973.
(4) Boistelle, R.; Astier, J. P. *Journal of Crystal Growth* **1988**, *90*, 14-30.
(5) Shouheng Sun, H. Z. *Journal of American Chemical Society* **2002**, *124*, 8204-8205.
(6) Langevin, D. *Annual Review of Physical Chemistry* **1992**, *43*, 341-369.
(7) Paul, B. K.; Moulik, S. P. *Current Science* **2001**, *80*, 990-1001.
(8) Gupta, A. K.; Gupta, M. *Biomaterials* **2005**, *26*, 3995-4021.
(9) Duraes, L.; Costa, B. F. O.; Vasques, J.; Campos, J.; Portugal, A. *Materials Letters* **2005**, *59*, 859-863.
(10) Zhang, C.; Wangler, B.; Morgenstern, B.; Zentgraf, H.; Eisenhut, M.; Untenecker, H.; Kruger, R.; Huss, R.; Seliger, C.; Semmler, W.; Kiessling, F. *Langmuir* **2007**, *23*, 1427-1434.
(11) Tartaj, P.; Gonzalez-Carreno, T.; Serna, C. J. *Langmuir* **2002**, *18*, 4556-4558.
(12) Lu, Y.; Yin, Y. D.; Mayers, B. T.; Xia, Y. N. *Nano Letters* **2002**, *2*, 183-186.
(13) Butter, K.; Kassapidou, K.; Vroege, G. J.; Philipse, A. P. *Journal of Colloid and Interface Science* **2005**, *287*, 485-495.
(14) Chen, D.; Xu, R. *Materials Research Bulletin* **1998**, *33*, 1015-1021.
(15) Murray, C. B.; Norris, D. J.; Bawendi, M. G. *Journal of the American Chemical Society* **1993**, *115*, 8706-8715.
(16) Sato, S.; Murakata, T.; Yanagi, H.; Miyasaka, F.; Iwaya, S. *Journal of Materials Science* **1994**, *29*, 5657-5663.
(17) Mukh-Qasem, A. *Journal Colloid Interface Science* **2005**.
(18) Alvarez, G. S. *Chemical Engineering Science* **2006**, *61*, 4625.
(19) Napper, N. H. *J. Colloid Interface Sci.* **1970**, *32*.
(20) Fritz, G.; Schadler, V.; Willenbacher, N.; Wagner, N. J. *Langmuir* **2002**, *18*, 6381-6390.
(21) Sahoo, Y.; Pizem, H.; Fried, T.; Golodnitsky, D.; Burstein, L.; Sukenik, C. N.; Markovich, G. *Langmuir* **2001**, *17*, 7907-7911.
(22) Sahoo, Y.; Goodarzi, A.; Swihart, M. T.; Ohulchanskyy, T. Y.; Kaur, N.; Furlani, E. P.; Prasad, P. N. *Journal of Physical Chemistry B* **2005**, *109*, 3879-3885.
(23) Kandori, K.; Kawashima, Y.; Ishikawa, T. *Journal of Colloid and Interface Science* **1992**, *152*, 284-288.
(24) Decuyper, M.; Joniau, M. *Langmuir* **1991**, *7*, 647-652.

(25) Wooding, A.; Kilner, M.; Lambrick, D. B. *Journal of Colloid and Interface Science* **1992**, *149*, 98-104.
(26) Zhang, Y.; Kohler, N.; Zhang, M. Q. *Biomaterials* **2002**, *23*, 1553-1561.
(27) Butterworth, M. D. J. *J. Magn. Magn. Mater.* **2005**, *28*.
(28) Santra, S.; Tapec, R.; Theodoropoulou, N.; Dobson, J.; Hebard, A.; Tan, W. H. *Langmuir* **2001**, *17*, 2900-2906.
(29) Shon, Y. S.; Dawson, G. B.; Porter, M.; Murray, R. W. *Langmuir* **2002**, *18*, 3880-3885.
(30) Angelova, M.; Dimitrov, D. S. *Biophysics of Membrane Transport, Vols 1 & 2* **1988**, 305-305
760.
(31) Angelova, M. I.; Soleau, S.; Meleard, P.; Faucon, J. F.; Bothorel, P. *Trends in Colloid and Interface Science Vi* **1992**, *89*, 127-131
340.
(32) Chen, S. H.; Teixeira, J. *Phys. Rev. Lett.* **1986**, *57*, 2583.
(33) Singh, M. A.; Ghosh, S. S.; Shannon, R. F. *J. Appl. Crysallogr* **1993**, *26*, 787.
(34) Provencher, S. W. *Comput. Phys. Commun.* **1982**, *27*, 213.

3 - Drug carriers

3.1 Uncoated Cobalt Ferrite nanoparticles

Materials: Iron(III) chloride hexahydrate (97%), Cobalt(II) nitrate hexahydrate (98%), Sodium hydroxide (minimum 98%), tetramethylammonium hydroxide 25%wt solution in water (TMAOH), Sodium chloride (minimum 99.5%) from Sigma-Aldrich, and concentrated nitric acid (90%) from Fluka.

Cobalt Ferrite nanoparticles were prepared by the co-precipitation method, introducing minor modifications to the Massart's method[1,2]. Briefly, aqueous solutions of 1 M $FeCl_3$ (64 ml) and $Co(NO_3)_2$ (32 ml) were added to concentrated nitric acid (2 ml). The mixture was heated to the boiling point and then, as fast as possible, mixed under vigorous agitation with 1 M NaOH solution (400 ml) warmed up till boiling. The boiling temperature and the stirring were maintained for 90 minutes. The particles obtained were separated by magnetic decantation, washed with water and added to 2 M HNO_3 (40 ml). The precipitate was again separated by magnetic decantation, dispersed in a boiling solution obtained by dissolving 0.5 M $FeCl_3$ (56 ml) and 0.5 M $Co(NO_3)_2$ (28 ml) and kept under vigorous agitation for 30 minutes. The precipitate obtained after this treatment was isolated and washed with water[3,4] .

To prepare larger nanoparticles the same synthetic procedure was used, but the Co(II), Fe(III), NaOH mixture was kept to the boiling

temperature during 120 minutes. For negatively charged $CoFe_2O_4$ nanoparticles, the precipitate was dispersed in 0.25 M TMAOH solution. For positively charged $CoFe_2O_4$ nanoparticles, the precipitate was washed with HNO_3 1 M (30 ml) and then dispersed in water. The concentration of the nanoparticles was checked by inductively coupled plasma atomic mission spectrometer (ICP-AES) and eventually adjusted by dilution or increased by means of an ultrafiltration cell (Amicon, Millipore corporation).

Characterization

Uncoated cobalt–ferrite nanoparticle dispersions were characterized by SAXS and DLS.

SAXS spectra of these solutions, corrected for the solvent, are reported in figure 3.1a and 3.1b.

The scattering intensity due to small $CoFe_2O_4$ nanoparticles (negatively and positively charged) was modelled according to the formalism introduced by Bartlett and Ottewill for polydisperse spherical particles[5]. In this approach, the particles are described as spherical objects with a Schulz distribution of radii[6]. In particular, the model accounts for a polydisperse population of spheres with uniform scattering length density. No structure factors were included in this model: in fact, due to the low concentration of particles in the dispersions, the interparticle interference effects can be neglected.

The model-fitting analysis of Schulz sphere is:

$$I(q) = (\frac{4\pi}{3})^2 N_0 \Delta\rho^2 \int_0^\infty f(R) R^6 F^2(qR) dR \qquad (3.1)$$

where N_0 is the total number of particles per unit volume, $\Delta\rho$ is the difference in scattered lenght density, F(qR) is the scattering amplitude for a sphere, and f(R) is the Schulz distribution of the radii.

$$f(R) = (z+1)^{z+1} x^z \frac{\exp[-(z+1)x]}{R_{avg}\Gamma(z+1)} \qquad (3.2)$$

where R_{avg} is the mean radius, z is the variance of distribution related to polidispersity and Γ is the gamma function.

The best fittings of small magnetic NPs are reported in figure 3.1a as solid lines. The estimated average radius <R> and the polidispersity are reported in Table 3.1. The system is affected by a considerable polidispersity, consistently with what observed for similar magnetic nanoparticles. In Figure 3.1b SAXS spectrum from larger $CoFe_2O_4$ nanoparticles is reported; the solid curve represents the best fitting results.

For large $CoFe_2O_4$ NPs it was not possible to fit the curve as a single population of particles, so a bimodal function has been used and each population was modeled as polidisperse spheres of radius R with a Schulz distribution of the radii [6] (Table 3.1). Spheres of about 23 nm in radius are the most represented population, while an averaged radius of 8 nm characterizes the second one.

The same samples have been investigated by DLS (Figure 3.2) and the autocorrelation functions are well fitted with Cumulant analysis. The obtained hydrodynamic radii, R_H, and polydispersity values are reported in Table 3.1.

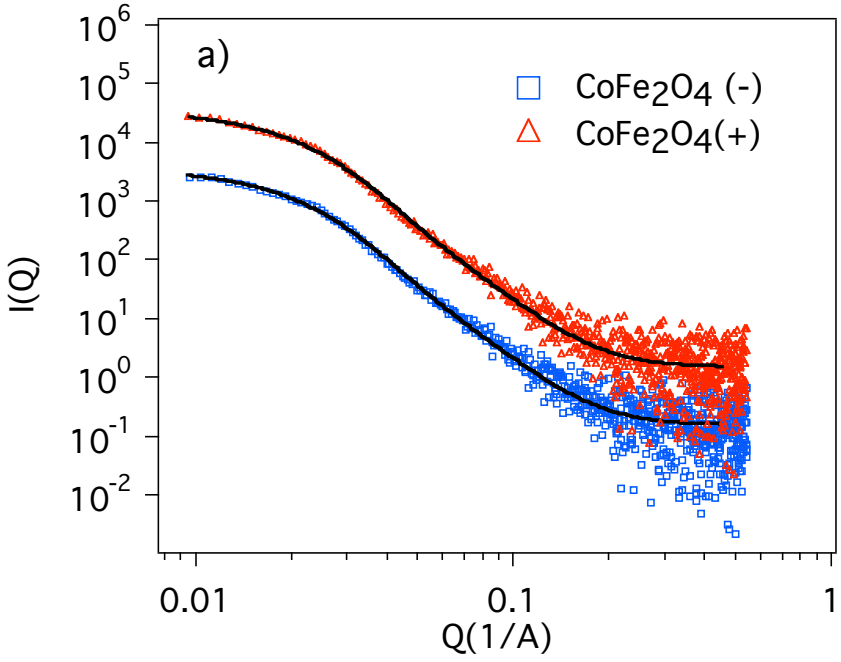

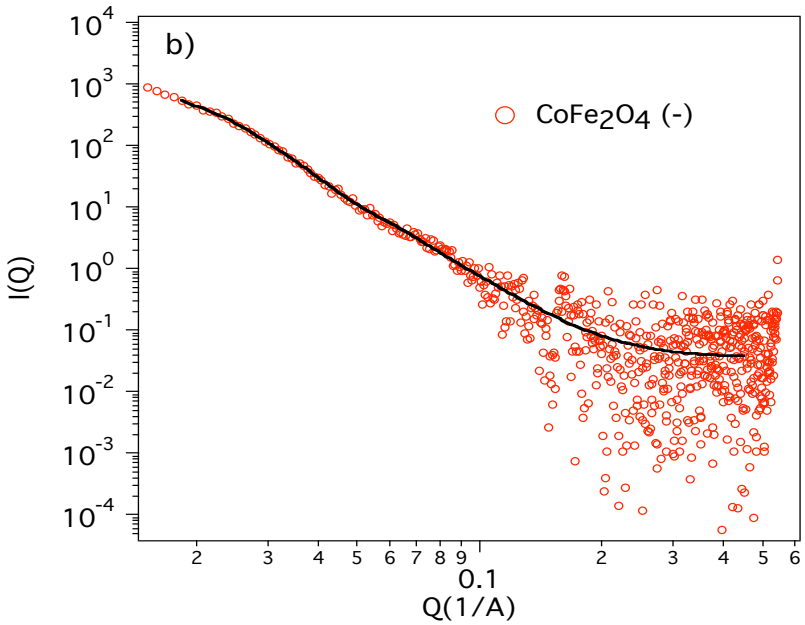

Figure 3.1. SAXS spectra (a) of small negative and positive cobalt-ferrite nanoparticles; (b) SAXS spectra of large negative cobalt-ferrite nanoparticles.

Table 3.1. Structural parameters of $CoFe_2O_4$ nanoparticles by SAXS and DLS

	Small $CoFe_2O_4$ (-)	**Small $CoFe_2O_4$ (+)**	**Large $CoFe_2O_4$ (-)**
SAXS fitting			
$A^*\phi$	0.0125	0.0123	0.0105 0.0013
<R> (nm)	5.7	5.9	23.4 8.3
Polydispersity	0.44	0.42	0.21 0.20
Cumulant analysis			
R_H (nm)	15.9	17.9	27.6
Polydispersity	0.20	0.21	0.19
CONTIN			
$<R_H>$	9.8	12.2	20.9

The R_H values of the nanoparticles are larger than the mean radii estimated by SAXS analysis: in fact, the objects diffusing in the aqueous solution are composed by the oxide cores together with their hydration layers, which do not contribute to the scattering intensities in SAXS experiments.

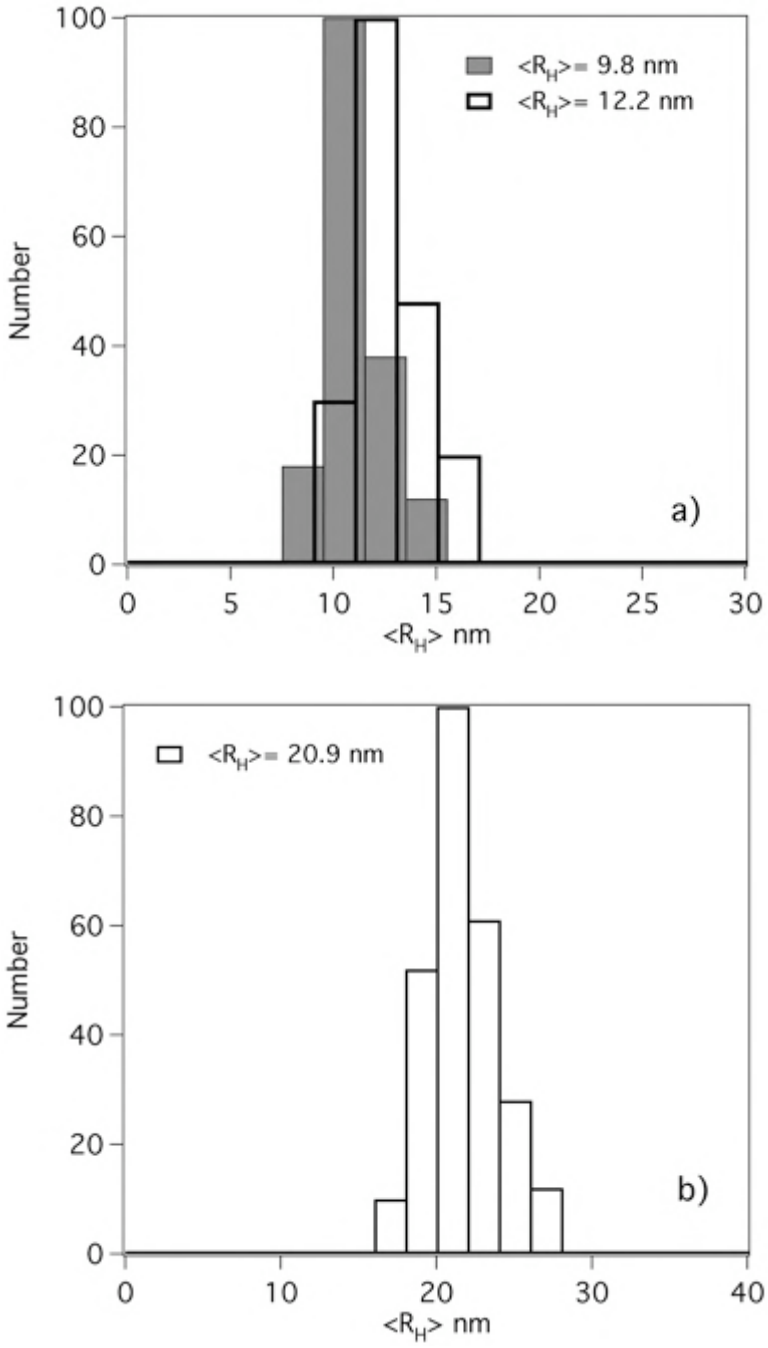

Figure 3.2. (a) Size distributions of small negative and positive cobalt-ferrite nanoparticles; (b) Size distribution of large negative cobalt-ferrite nanoparticles.

Negative uncoated Cobalt-ferrite nanoparticles were also investigated by TEM, confirming the results obtained by SAXS experiments.
These nanoparticles were also magnetically characterized by SQUID and AC measurements. TEM pictures and SQUID data of negative uncoated Cobalt-ferrite nanoparticles were reported in the next paragraph because the obtained results were compared with the ones obtained for citrate-coated Cobalt-ferrite nanoparticles.

3.2 Citrate-coated Cobalt Ferrite nanoparticles

Materials: Tri-Sodium citrate dihydrate (>99%), citric acid monohydrate (>99.5%), sodium hydroxide (99.5%) were purchased from Sigma-Aldrich. HEPES [4-(2-hydroxyethyl) piperazine-1-ethane-sulfonic acid] (ultra >>99.5%), concentrated nitric acid (90%) were purchased from Fluka. Uncoated Cobalt-ferrite nanoparticles dispersed in TMAOH.

Citrate-coated Cobalt ferrite nanoparticles were prepared starting from uncoated particles by adsorption of citric acid on their surface through the coordination of the carboxylate functionalities[7]. Negatively charged Cobalt ferrite nanoparticles (10 ml, 1% wt) in TMAOH were added to a 100 mM citric acid solution (30 ml) and slightly stirred for 1 h at room temperature (the resulting pH is around 5). After recollecting the precipitate with the magnet, nanoparticles were dispersed in 20 mM trisodium citrate (30 ml) and kept under stirring for 45 min. The obtained particles were separated by magnetic decantation and washed several times with water and acetone in order to remove any excess of citric acid. The

citrate coated nanoparticles were gently dried under a nitrogen gas flux, dispersed in the buffer solution (10 mM HEPES, 107 mM NaCl, 5.3 mM NaOH, pH 7.4) and kept under slight stirring for 24 h. Finally the dispersion was centrifuged at 1000 g for 2 min and the supernatant was dialyzed against water for 24 h through a cellulose dialysis bag (avg. flat width 23 mm, MWCO 12400, 99.99% retention) in order to remove non-adsorbed citrate species. However a residual ionic strength is always present because of solvated anions in equilibrium with the adsorbed ones. The adsorption of citrate onto metal oxide surfaces has been verified by attenuated total reflectance Fourier-transform infrared (ATR-FTIR) spectroscopy[8].

Iron and Cobalt contents in uncoated and coated nanoparticles was checked by inductively coupled plasma atomic emission spectrometer (ICP-AES) and eventually decreased by dilution or concentrated by means of ultrafiltration (Amicon, Millipore corporation).

Characterization

SAXS spectrum of citrate-coated Cobalt ferrite nanoparticles is reported in figure 3.3 and it has been investigated through the model fitting of spheres with a Shulz distribution of the radii.

The fitting results are reported in Table 3.2, where also the main features of negative uncoated nanoparticles were reported for comparison. The obtained results indicate that the radius of citrate-coated nanoparticles is very similar to the radius previously obtained for negative uncoated nanoparticles (the precursor). This is due to the fact that the electronic density in Cobalt ferrite nanoparticles largely overrules that of the citrate shell, so that SAXS signal accounts only for the magnetic cores. SAXS fitting shows that uncoated nanoparticles seem to be larger than coated nanoparticles. This is reasonably due to the presence of aggregates

formed by uncoated magnetic NPs.

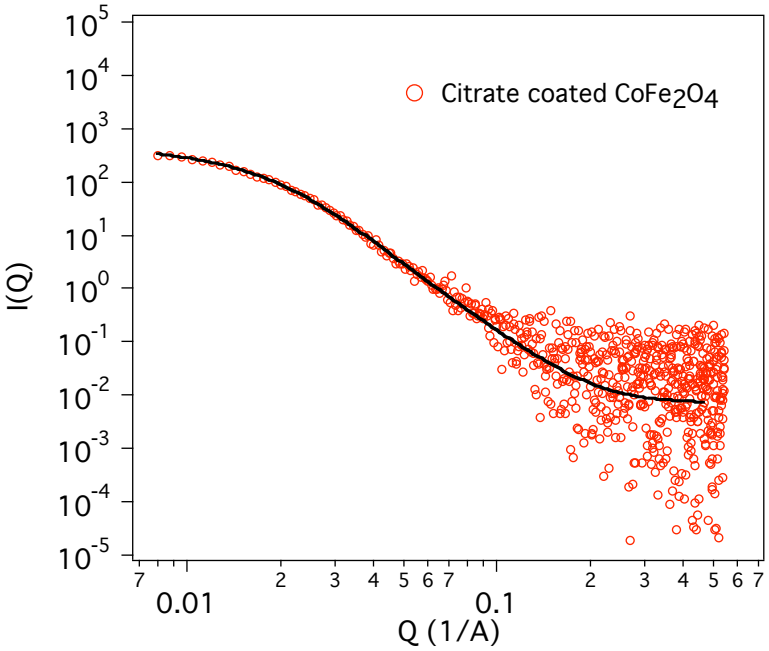

Figure 3.3. SAXS spectrum of citrate coated (□) Cobalt ferrite nanoparticles.

Nanoparticles dispersed in water were also characterised by DLS. To avoid multiple scattering, samples were first diluted 100 times with water. The DLS autocorrelation functions of citrate-coated Cobalt ferrite nanoparticles dispersions are well fitted with Cumulant analysis and their size distribution (obtained from a CONTIN analysis) is compared with the small negative uncoated ones, as shown in Figure 3.4. The obtained hydrodynamic radii, R_H, and polydispersity values are reported in Table 3.2. Citrate-coated nanoparticles show a larger hydrodynamic radius with respect to the uncoated ones that confirms the presence of the citrate shell.

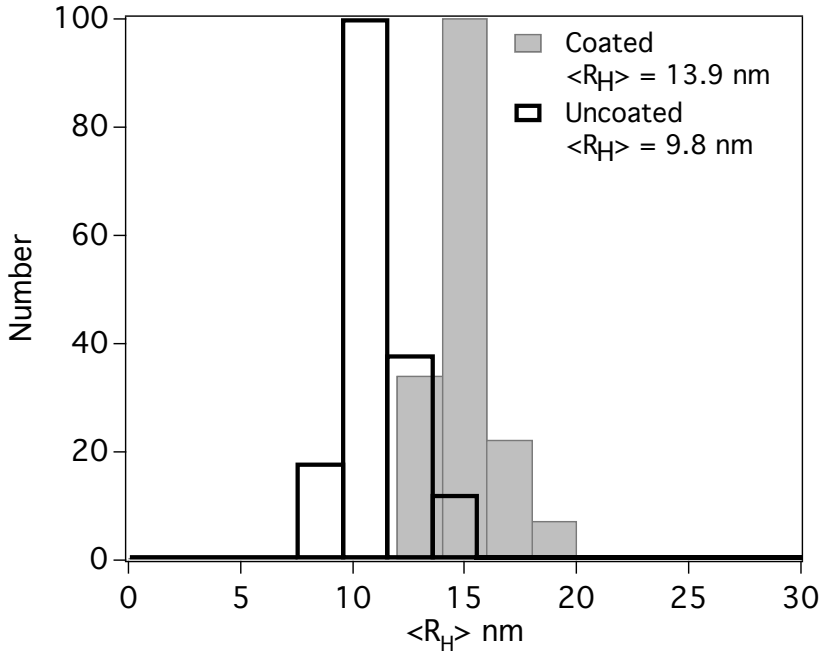

Figure 3.4. Size distributions of coated and uncoated Cobalt ferrite nanoparticles in water obtained from DLS analysis.

Table 3.2. Structural parameters of $CoFe_2O_4$ nanoparticles in water dispersions by SAXS and DLS analysis.

	Citrate coated $CoFe_2O_4$	**Uncoated $CoFe_2O_4$**
SAXS Fitting		
<R> [nm]	4.9	5.6
Polydispersity	0.60	0.49
Cumulant analysis		
R_H[nm]	21.3	15.9
Polydispersity	0.15	0.20
CONTIN		
$<R_H>$ [nm]	13.9	9.8

TEM images of citrate-coated Cobalt ferrite nanoparticles and negative uncoated ones were reported in figure 3.5. TEM pictures show that both coated and uncoated nanoparticles are quite polydisperse and their shape is nearly spherical, in agreement with SAXS results. In figure 3.6 the size distribution obtained from TEM images analysis of both NP samples is reported. A comparison of

the histograms shows that the radii of coated nanoparticles range from 2 to 8 nm according to a lognormal distribution centered at 3.4 nm, while uncoated nanoparticles present a population ranging between 2 and 6 nm of radius and some larger particles and aggregates, ranging from 8 to 12 nm of radius. It is important to stress that the citrate coating cannot be detected in TEM micrographs, because of its poor electronic density.

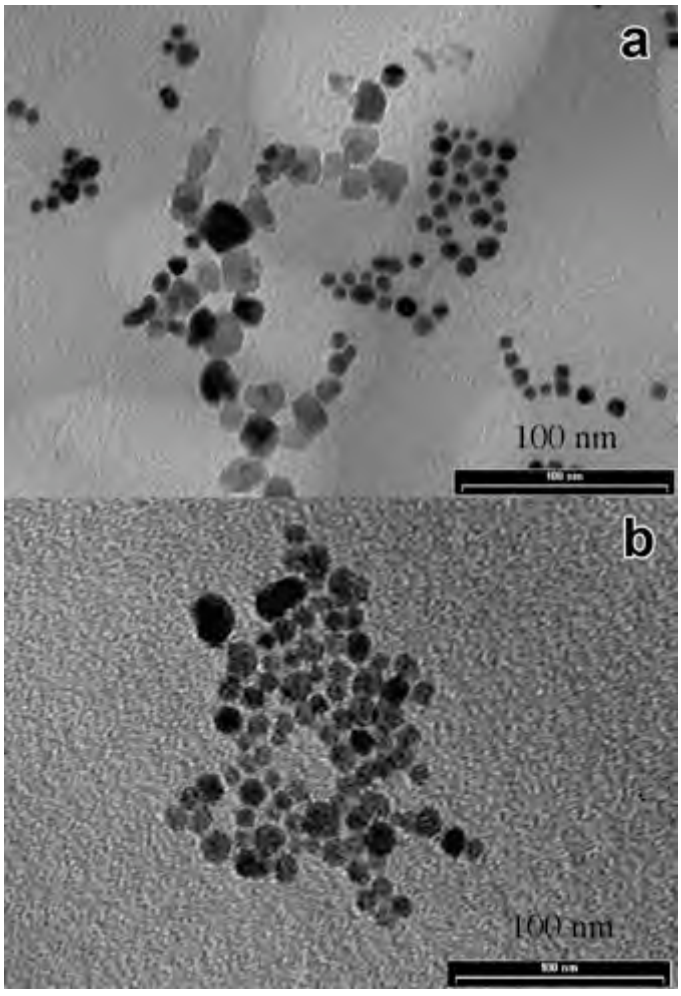

Figure 3.5. TEM images of (a) negative uncoated and (b) citrate coated Cobalt ferrite nanoparticles.

ATR-FTIR spectroscopy has been used to investigate the adsorption of citrate on Cobalt ferrite nanoparticles surfaces[9].

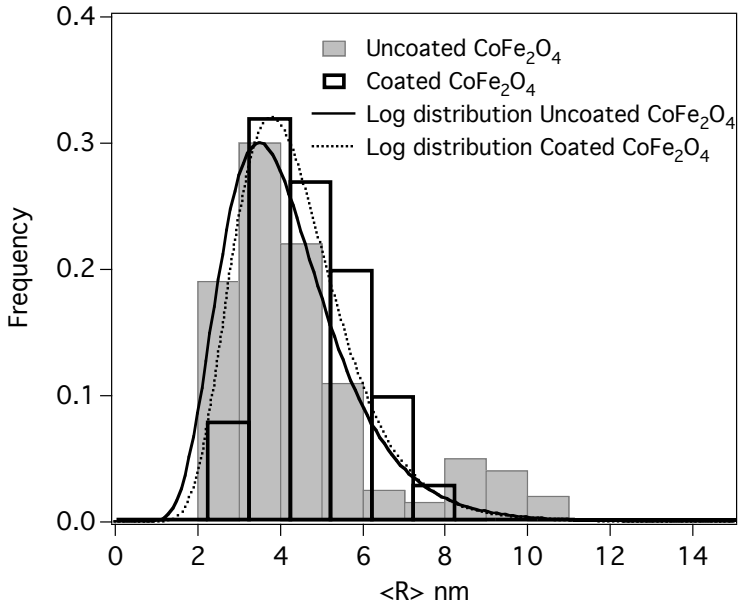

Figure 3.6. Size distribution of uncoated and citrate coated nanoparticles obtained from the analysis of TEM micrographs.

Figure 3.7 shows FTIR spectra of (a) citrate coated nanoparticles solution (1.6% wt) at pH 7.4, (b) pure trisodium citrate solution (20 mM) and (c) citric acid solution (20 mM).

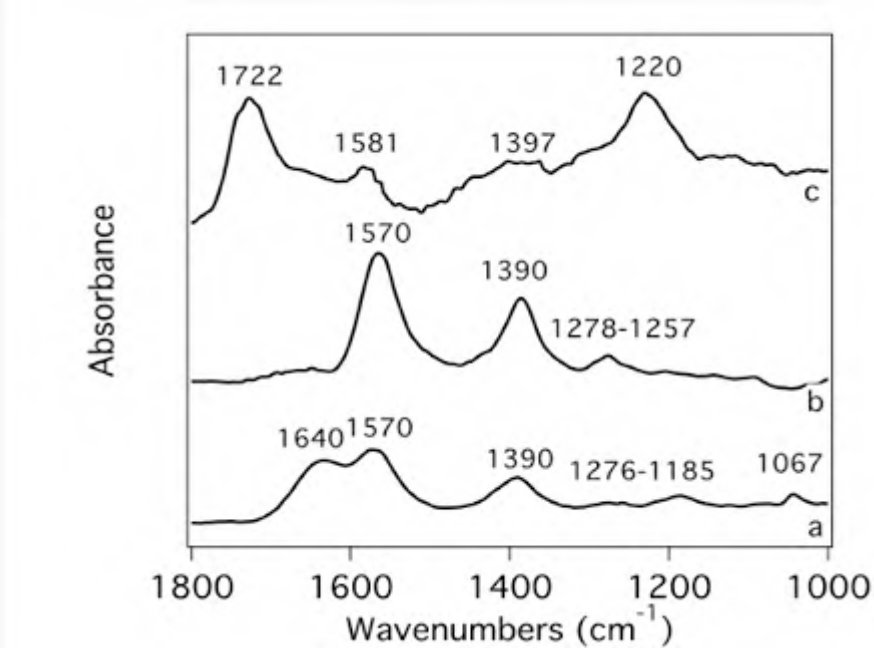

Figure 3.7. ATR-FTIR spectra of (a) citrate coated $CoFe_2O_4$ nanoparticles at pH=7.4, (b) 20 mM tri-sodium citrate solution, (c) 20 mM citric acid solution.

In Table 3.3 FTIR absorption frequencies are reported together with the corresponding assignments for all samples. The band at 1722 cm^{-1} for citric acid, corresponding to the C=O vibration, is not present in the spectra of tri-sodium citrate and citrate coated nanoparticle. This feature highlights that citric acid binds the Cobalt ferrite surface of nanoparticles by adsorption of citrate anions. The 1570 cm^{-1} and 1390 cm^{-1} peaks in pure citrate are assignable to the asymmetric and symmetric C-O stretching, respectively. Upon binding of citrate to the Cobalt ferrite surface, the asymmetric C-O stretching band splits in two peaks at 1640 and 1570 cm^{-1}. The 1640 cm^{-1} peak is the asymmetric C-O stretching of Fe-citrate complexes, in equilibrium with free citrate anions, whose peak remains at 1570 cm^{-1}.

Table 3.3. FTIR vibrational assignments for citric acid, tri-sodium citrate and adsorbed citrate on Cobalt ferrite nanoparticles

Vibrational modes	Frequency (cm^{-1}) Citric acid	Frequency (cm^{-1}) Tri-sodium citrate	Frequency (cm^{-1}) Adsorbed citrate on nanoparticles
ν_s (C=O)	1722	—	—
ν_{as} (C-O)	1581	1570	1640
ν_s (C-O)	1397	1390	1390
δ (O=C-O)	—	1278-1257	1276-1185
ν (C-OH)	1220	—	1067

Magnetic characterization of citrate coated and uncoated nanoparticles were performed by SQUID and AC measurements.

Low temperature hysteresis loops were measured on water dispersions of both $CoFe_2O_4$ nanoparticles at the same concentration (16.5 mg/ml). At low temperature, ice creates a glassy matrix that traps the nanoparticles, thus preventing their orientation due to torque effects induced by the applied magnetic field. As can be seen

from Figure 3.8a, the magnetic behaviour of the two types of particles is very similar, confirming that the citrate layer does not affect surface anisotropy of the particles, and the capping process does not introduce significant size alterations. The coercive field value of 9000 Oe is in line with the particle size found by SAXS and TEM measurements.

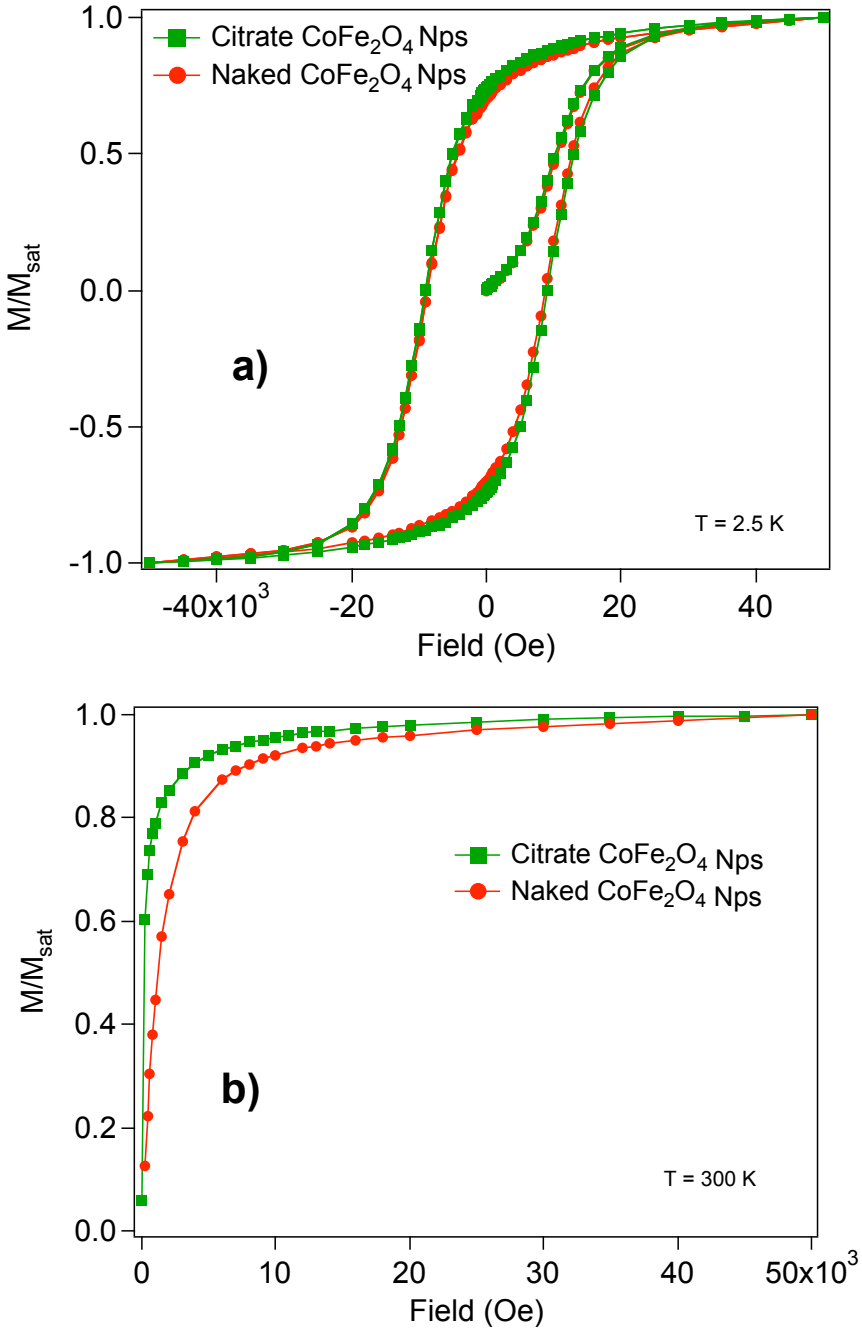

Figure 3.8. Magnetization curves of citrate-coated and uncoated cobalt ferrite nanoparticles measured at 2.5 K (a) and 300 K (b).

Room temperature magnetization curves were acquired for the same nanoparticle dispersions (Figure 3.8b). In this case, particles are free to rotate in water; as a consequence, the low field response of the sample is due to particle alignment with the external magnetic field, rather than to spin orientation. By comparing the magnetization curves of the two nanoparticle samples, it is clear that citrate coated particles show a stronger magnetic response at low applied field than uncoated ones. This result is a strong indication that aggregation is likely to occur in uncoated dispersions: in fact, if a particle aggregate dispersed in a solvent is immersed in a magnetic field, it will align with the field. However, single particles in the aggregate still possess a random magnetic moment distribution (Figure 3.9a), that will align, either by mechanical rotation or spin flip across the energy barrier, with higher magnetic field values.

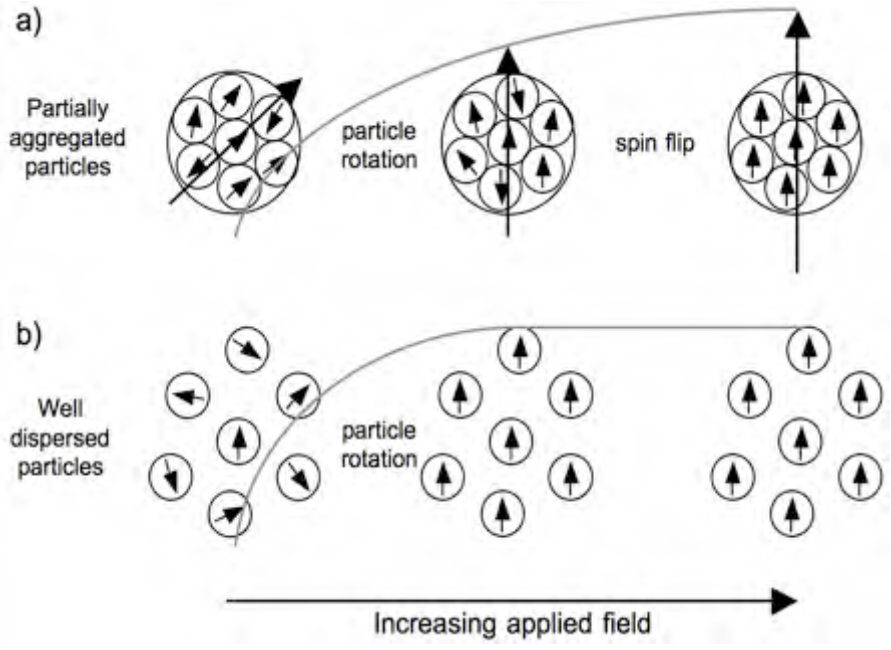

Figure 3.9. Schematic picture of the behaviour of a) aggregated and b) well dispersed magnetic particles in a fluid medium. Grey lines mimic the magnetization value as a function of the applied field.

In the case of well dispersed single grain particles (as in the case of citrate coated nanoparticles) instead, a weak applied field is enough to align all particles (Figure 3.9b). The result points out that, as expected, the citrate coating reduces particle aggregation in solution.

AC measurements carried out on powder samples of both uncoated and coated particles confirm that the magnetic behaviour of the magnetic cores is very similar. Both samples show a bimodal distribution of magnetic relaxation times (the faster under room temperature and the slower above 300 K on the investigated experimental time scale), coherently with the size distribution observed in TEM analysis.

AC results of negative uncoated and citrate-coated Cobalt ferrite NPs are reported in Figure 3.10 (a,b).

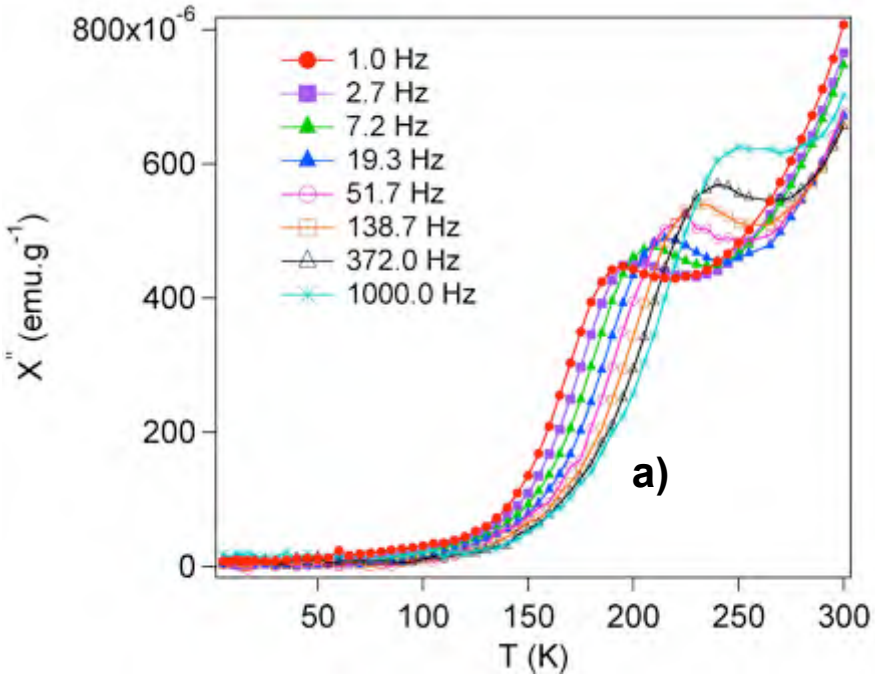

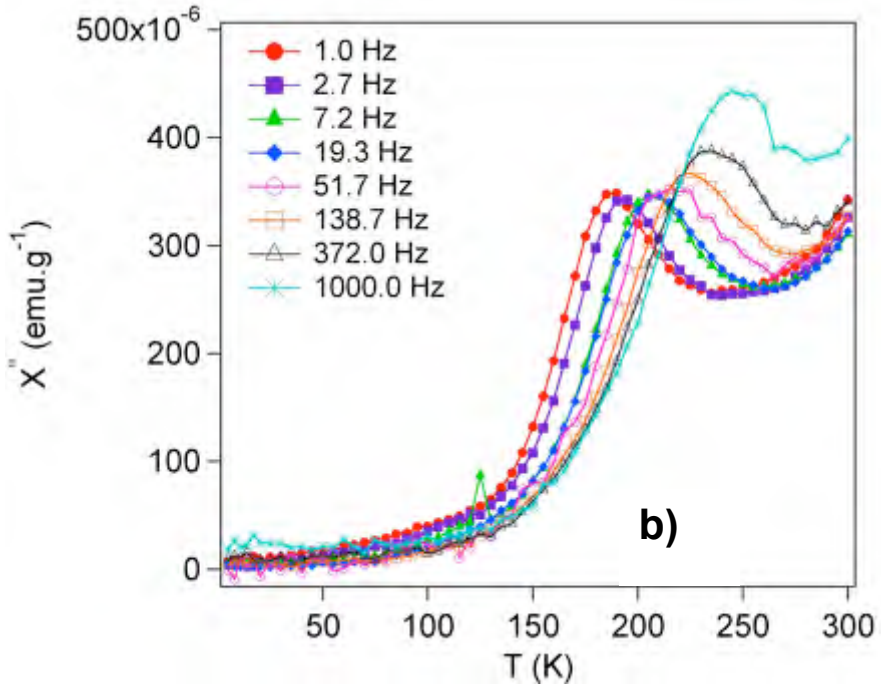

Figure 3.10**.** AC measurements on powder samples of (a) uncoated and (b) citrate-coated Cobalt ferrite nanoparticles

3.3 Oleic acid-coated Cobalt Ferrite nanoparticles

Materials: oleic acid (95%), tetramethyl ammonium hydroxide (TMAOH; 25% wt% water solution) and cyclohexane (99.9%) were purchased from Sigma-Aldrich. Acetone (99.5%) was purchased from Fluka. Uncoated positively charged Cobalt-ferrite nanoparticles in water.

Uncoated positively charged Cobalt-ferrite nanoparticles obtained by Massart method were dispersed in water (45 ml) and poured in a separatory funnel. A 10% wt solution of oleic acid in cyclohexane (15 ml) was used as extraction medium for magnetic nanoparticles and added to the water dispersion in the funnel. A 25% wt solution of TMAOH (20 ml) was added dropwise to the mixture and vigorously agitated in order to promote the transfer of Cobalt ferrite nanoparticles in the cyclohexane phase where the adsorption of oleic acid on their surface took place through the coordination of the carboxylate functionalities. This procedure was repeated ten times in order to extract all the nanoparticles from the aqueous to the cyclohexane phase. The solvent of the collected organic solution was removed by evaporation in order to take off any trace of water and then the dry nanoparticles were washed twice with acetone (30 ml).
After recollecting the precipitate with the magnet, the Cobalt ferrite nanoparticles covered with oleic acid were dispersed in cyclohexane. Finally the dispersion was centrifuged at 1000 g for 2 min to remove larger nanoparticle clusters and the supernatant (containing the stable nanoparticles) was recuperated.
Iron and cobalt contents in nanoparticles were checked by

inductively coupled plasma optical emission spectrometer (ICP-AES).

Characterization

SAXS spectra of nanoparticles (corrected for the solvent, cyclohexane) and the best fitting curve are reported in figure 3.11. The scattering intensity due to the $CoFe_2O_4$ nanoparticles was modeled according to the formalism introduced by Bartlett and Ottewill for polydisperse spherical particles[5]. In this approach, the particles are described as spherical core-shell objects with a Schulz distribution of the core radius and constant thickness of the shell[6,10]. In particular, the model accounts for a polydisperse population of spheres with uniform scattering length density. No structure factors have been included in this model as, due to the low concentration of particles in the dispersions, the interparticle interference effects can be neglected.

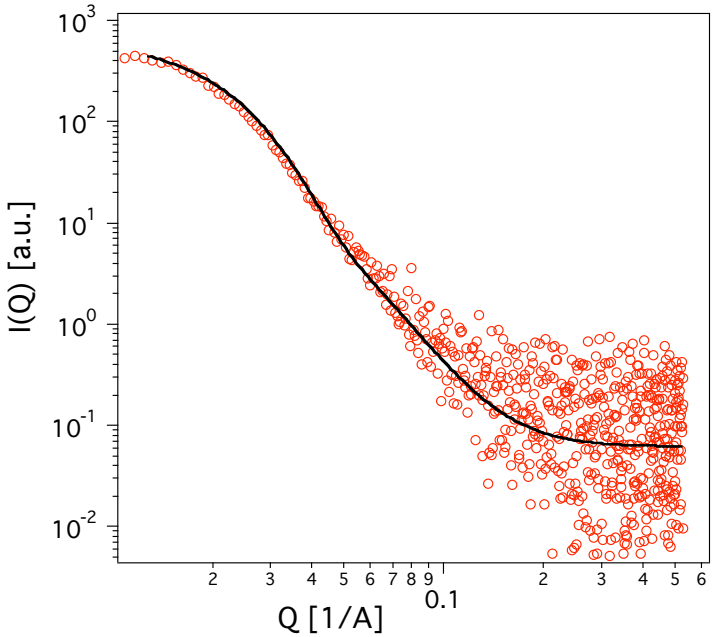

Figure 3.11. SAXS spectra of oleic acid coated (O) cobalt ferrite nanoparticles

The autocorrelation functions obtained by DLS measurements were well fitted with Cumulant analysis; the size distribution is shown in figure 3.12. The hydrodynamic radius calculated by DLS includes also the oleic acid shells and the solvent layers of the

nano-objects in solution.

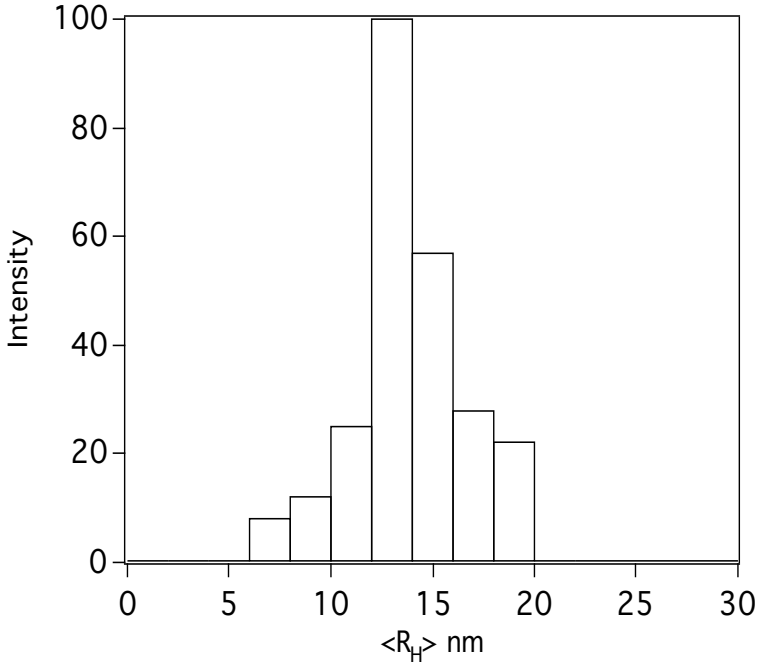

Figure 3.12. Size distribution of oleic-coated Cobalt-ferrite nanoparticles obtained from DLS analysis.

In table 3.4 the main features of oleic Cobalt-ferrite nanoparticles were reported.

Table 3.4. Structural parameters of oleic acid coated $CoFe_2O_4$ nanoparticles by SAXS and DLS analysis.

SAXS Fitting	
<R> [nm]	7.5
Polydispersity	0.28
Shell thickness [nm]	2.4
Cumulant analysis	
R_H[nm]	22.4
Polydispersity	0.24
CONTIN	
$<R_h>$ [nm]	12.4

3.4 Fluorescent Cobalt Ferrite nanoparticles (MP@SiO_2(RITC))

Materials: Rhodamine B isothiocyanate (RITC) (λ_{ex}= 546 nm, λ_{em}= 572 nm), tetraethyl orthosilicate (TEOS), 3-aminopropyltriethoxysilane (APTES), tetramethylammonium hydroxide 25% wt solution in water (TMAOH), chloroform (99.9% HPLC grade), absolute ethanol (≥ 99.5%) were purchased from Sigma-Aldrich. Uncoated negative charged Cobalt-ferrite nanoparticles in water.

The synthesis of fluorescent silica-coated Cobalt-ferrite nanoparticles includes two important steps: functionalization of APTES with the fluorescent molecule RITC (APTES-RITC) and polysiloxane coating of magnetic NPs with TEOS and APTES-RITC.

- *APTES-RITC,* aminopropyltriethoxysilane covalently coupled to the fluorescent dye Rhodamine B, was prepared from APTES (0.0238 mmol) and RITC (0.0124 mmol) dissolved in 8 ml of anhydrous ethanol. The mixure was stirred for 24 hours in the dark and under nitrogen[11].
- *MP@SiO_2(RITC)* were prepared by a sol-gel method, introducing some modifications to the standard procedure[12]. RITC coating of Cobalt ferrite NPs was obtained by adding to 1 ml of 0.15 M Cobalt ferrite nanoparticles dispersed in TMAOH, diluted in 3 ml of ethanol, 18 μl of APTES-RITC and 3μl of TEOS. The reaction was allowed to proceed at room temperature for 2 hours in the dark under continuous stirring. The growth of APTES-RITC shells on Cobalt ferrite NP involved the hydrolysis of TEOS and the condensation of silica on Cobalt ferrite cores. MP@SiO_2(RITC) were separated from the reaction

medium by centrifugation at 4500 rpm for 20 minutes. The collected particles were washed several times with ethanol and then dispersed in water and dialyzed by means of ultrafiltration (Amicon, Millipore corporation, membrane of regenerated cellulose, 10 kDa NMWL) in order to remove any excess of unreacted RITC. Cobalt and iron contents in MP@SiO_2(RITC) were checked by inductively coupled plasma atomic emission spectrometer (ICP-AES) indicating 950 mg/ml and 1920 mg/ml of Co and Fe respectively.

Characterization

MP@SiO_2(RITC) size and shape were observed by an inverted Optical Microscope (Nikon Diaphot 300) equipped with a DS-L1 charge-coupled device camera (oil immersion objective 100/1x25) and Epi-Fluorescence Attachement (Nikon HB-10104AF, mercury lamp λexc= 510 nm).

Confocal images of MP@SiO_2(RITC) were also acquired by a DMIRE2 Confocal Laser Scanning Microscope (CLSM, Leica TCS SP2) with argon ion lasers and a water immersion objective 63x/1.2W (Zeiss), exciting at λ= 514 nm and acquiring between 560 and 650 nm.

In Figure 3.13 (a,b) microscopy images of the particles are reported, evidencing fluorescent structures and the presence of some aggregates of MP@SiO_2(RITC) which have tendency to form chains aligned in a particular direction because of their magnetic anisotropy.

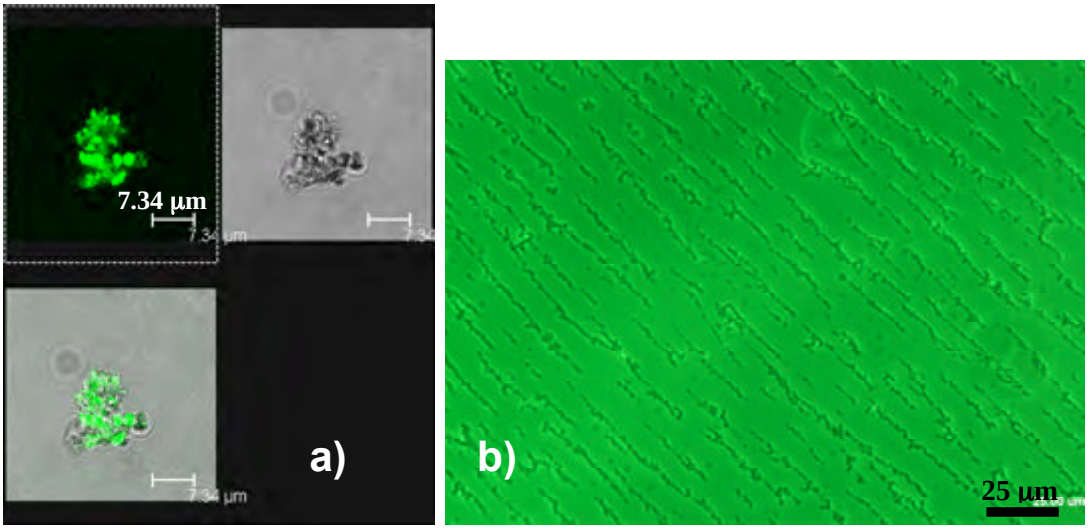

Figure 3.13. (a) CLSM (argon ion laser at λ= 514 nm) images, (b) optical microscopy images in phase contrast modality of MP@SiO_2(RITC). MP@SiO_2(RITC) have the tendency to align in a particular direction because of the magnetic anisotropy.

The autocorrelation functions, obtained by DLS measurements performed on MP@SiO_2(RITC) solution diluted 100 times with water, were well fitted with Cumulant analysis. The size distributions of nanoparticles have been extracted from CONTIN analysis, indicating the presence of three different populations (see Figure 3.14). In particular, a CONTIN analysis calculated in function of the number of nanoparticles has indicated a representative population of nanoparticles around 50 nm of diameter and the presence of some larger aggregates of about 180 nm and 350 nm of diameter.

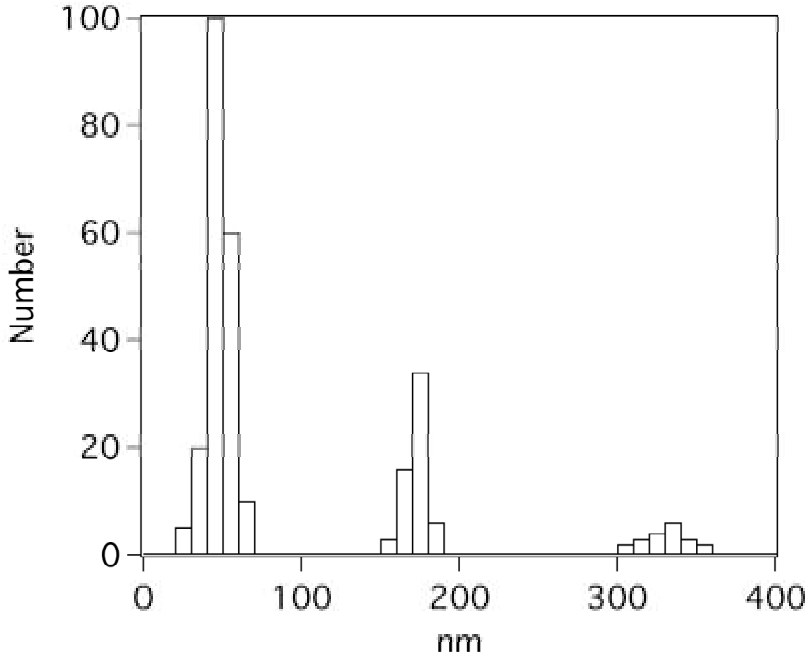

Figure 3.14. Size distribution of MP@SiO_2(RITC) nanoparticles obtained from DLS analysis in function of the number of nanoparticles.

The fluorescence emission spectra of MP@SiO_2(RITC) and APTES-RITC aqueous solutions were acquired exciting at λ= 546 nm (corresponding to the maximum fluorescence emission) and λ= 514 nm (corresponding to the laser line used for Confocal Microcopy acquisition). A comparison between MP@SiO_2(RITC) and APTES-RITC fluorescence spectra, reported in Figure 3.15 (a,b), has indicated a strong red shift effect for MP@SiO_2(RITC) due to the interaction of the dye with Cobalt ferrite NP, confirming that the APTES-RITC dye is effectively bounded to magnetic particles.

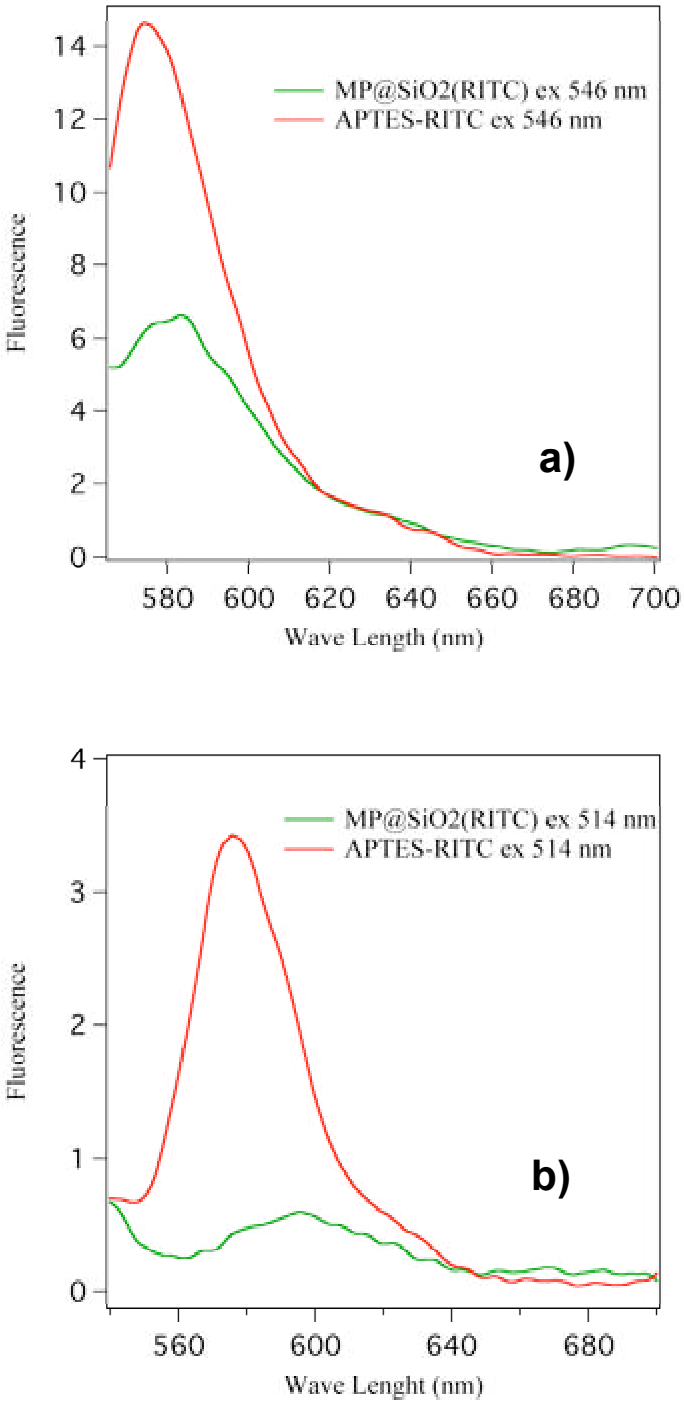

Figure 3.15. Fluorescence emission spectra of MP@SiO_2(RITC) and free APTES-RITC in water with excitation set at (a) 546 nm (maximum emission) and (b) 514 nm (laser line used for CLSM experiments).

3.5 Liposomes and Magnetoliposomes

Materials: L-α phosphatidylcholine egg yolk Grade 1 (99.9% TLC) in chloroform (PC) was purchased from Lipid Products. Sodium hydroxide (98%), sodium chloride (99.5%), 5(6)-carboxyfluorescein (>>95% HPLC, CF), ethylenediaminetetraacetic acid (EDTA, 99.5%) were purchased from Sigma-Aldrich. HEPES [4-(2-hydroxyethyl)piperazine-1-ethane-sulfonic acid] (ultra >>99.5%) was purchased from Fluka and Sephadex G-25 Superfine from Pharmacia Fine Chemicals.

Magnetoliposomes were prepared by the extrusion method (see Methods) where the lipid film hydration is followed by sequential extrusion[13-15].

- *Magnetoliposomes with hydrophilic magnetic nanoparticles* (uncoated and citrate-coated Cobalt ferrite NPs) embedded in the aqueous pool were prepared by evaporation of the solvent from a $CHCl_3$/MeOH solution of the lipid; the dry lipid film was hydrated with a buffer solution of Carboxyfluorescein (50 mM CF, 10 mM HEPES, 10 mM NaCl, 148 mM NaOH, 1 mM EDTA) and magnetic nanoparticles to give a lipid concentration of 20 mM.

- *Magnetoliposomes with hydrophobic magnetic nanoparticles* (oleic acid-coated Cobalt-ferrite NPs) entrapped in the lipid bilayer of the vesicles were prepared by evaporation of the solvent from a $CHCl_3$/MeOH solution of the lipid (PC) mixed to an aliquot of Cobalt ferrite Nps in cyclohexane and then the dry film was hydrated with the buffer solution of Carboxyfluorescein.

- *Control liposomes* without Cobalt-ferrite NPs were prepared by adding only the Carboxyfluorescein solution to the dry lipid film.

The suspensions were vortexed until complete dispersion of the film and then frozen-thawed six times. Multilamellar polydisperse vesicles were then sized down by repeated extrusion at room temperature through polycarbonate membrane (Whatman). Three steps of twenty-one extrusions through filters of 0.8 μm, 0.4 μm and 0.2 μm pore sizes allowed the preparation of a narrow sized distribution of unilamellar vesicles. The nanoparticles and the molecules of CF that were not entrapped inside the liposome pool were removed by gel exclusion chromatography (GEC) with Sephadex G-25 microcolumn (1 ml-syringe) saturated with lipids so that liposomes were recovered without dilution.

Under these conditions, 300 μl of liposome dispersions were eluted and centrifuged at 2000g for two minutes without loss or dilution of material.

Characterization

Magnetoliposomes with different concentrations of Cobalt ferrite nanoparticles were prepared and characterized.

The fractions of purified magnetoliposomes were collected and investigated by DLS in order to have their size distributions. The autocorrelation functions were well fitted with Cumulant analysis and the obtained hydrodynamic radii, R_H, are ranging between 70-85 nm and 95-115 nm for liposomes and magnetoliposomes, respectively, with polydispersity ranging from 0.10 to 0.20. The size distributions extracted from CONTIN analysis show that magnetoliposomes are constituted by a single population (monomodal distribution) centred at the R_H value obtained by Cumulant analysis (see the size distribution of magnetoliposomes and liposomes in Figure 3.16). No contribution to the overall scattering intensity arising from the Brownian motion of nanoparticles could be detected. However, if we externally add to a liposome solution the same concentration of nanoparticles

determined in our magnetoliposome samples, the scattering contribution of the nanoparticles is detectable and the correspondent autocorrelation function could not be fitted with Cumulant analysis.

Cobalt-ferrite nanoparticle concentrations were measured by Inductively Coupled Plasma–Atomic Emission Spectrometry (ICP-AES), while lipid concentrations after purification by the Steward-Marshall method[16]. Steward-Marshall is a colorimetric method based on the formation of a complex between phospholipid and ammonium ferrothiocyanate in chloroform; the lipid concentration is determined from the absorbance read at 485 nm.

The main features of the magnetoliposome dispersions investigated in this work are reported below and their encapsulation efficiency was estimated as the ratio of $CoFe_2O_4$ concentration before and after GEC purification.

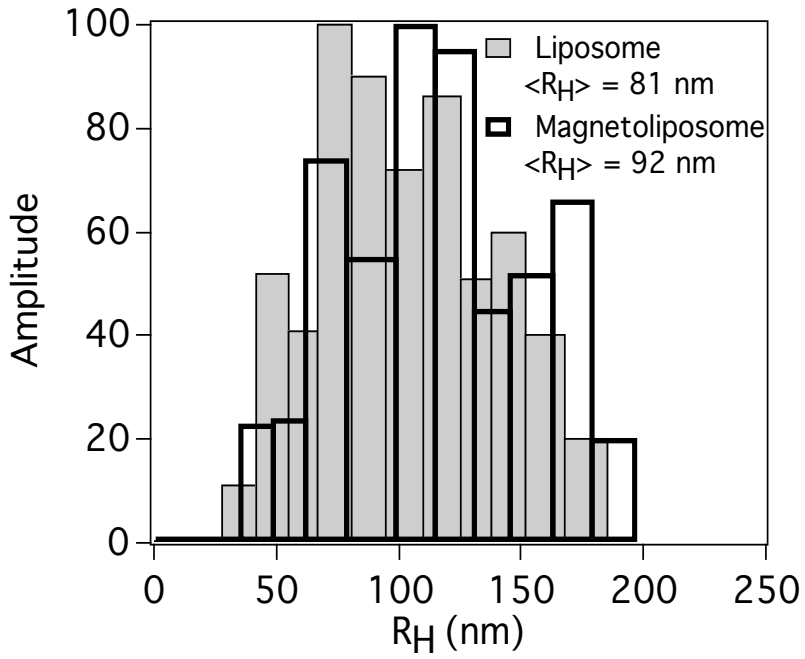

Figure 3.16. Representative size distributions of liposomes (grey bars) and magnetoliposomes (black bars) obtained by CONTIN analysis of the autocorrelation functions.

A detailed characterization of magnetoliposomes with hydrophilic and hydrophobic NPs has been reported in the following paragraphs.

3.5.1 Magnetoliposomes with hydrophilic nanoparticles

The main features of magnetic nanoparticles embedded in liposome aqueous pool are reported in table 3.5 (uncoated nanoparticles) and in table 3.6 (citrate-coated nanoparticles). An estimate of the mean number of magnetic nanoparticles per liposome, <N>, was calculated as the ratio of the number of nanoparticles (N_{NPs}) and lipid vescicles (N_{ves}), $<N> = N_{NPs}/N_{ves}$, where N_{NPs} and N_{ves} were obtained from their corresponding size and concentration through the following equations:

$$N_{NP} = \frac{M_{NP}}{d_{NP} \cdot V_{NP}} \qquad (3.3)$$

$$N_{ves} = \frac{V_{bilayer}}{V_{phospholipid} \cdot N_{phospholipid}} \qquad (3.4)$$

where M_{NP} is the total mass of $CoFe_2O_4$ as obtained from ICP-AES, d_{NP} is the density of $CoFe_2O_4$ nanoparticles, V_{NP} is the volume of a single nanoparticle according to SAXS results, N_{ves} is the total number of vesicles, $V_{bilayer}$ is the total volume occupied by the bilayer, $V_{phospholipid}$ is the volume occupied by a single lipid molecule and $N_{phospholipid}$ is the total number of lipid molecules.

Table 3.5. Uncoated Cobalt-ferrite nanoparticle loading in the liposomes

MLs	Charge[a]	[NPs] (mg/L)[b]	<R> (nm)[c]	<R_H> (nm)[d]	Encapsulation Percentage[e]	<N>[f]
A	(-)	9±0.1	5.7±0.2	84.2±0.7	9.5	0.4
B	(-)	37±0.4	5.7±0.2	84.5±0.9	7.4	1.5
C	(-)	60±0.6	5.7±0.2	86.7±1.0	6.3	2.5
D	(-)	194±2.0	5.7±0.2	90.2±1.2	6.2	8.6
E	(-)	162±1.6	23.4±1.0	92.0±1.0	16.2	0.2
F	(+)	58±0.6	5.9±0.2	87.9±1.0	6.8	2.6

Table 3.6. Citrate Cobalt-ferrite nanoparticle loading in the liposomes

MLs	[NPs] (mg/L)[b]	<R> (nm)[c]	<R_H> (nm)[d]	Encapsulation Percentage[e]	<N>[f]
A	216±3	4.9±0.1	95.5±1.1	53.7	2.2
B	449±4	4.9±0.1	96.5±1.2	43.7	4.6
C	2027±20	4.9±0.1	115.5±1.5	39.4	29.8

[a] Nanoparticle charge
[b] $CoFe_2O_4$ concentration by ICP-AES after GEC purification
[c] Average radius of nanoparticles by SAXS analysis
[d] Average hydrodynamic radius of MLs from DLS by CONTIN analysis
[e] $\{[CoFe_2O_4]_{\text{after GEC}}/[CoFe_2O_4]_{\text{before GEC}}\}\times 100$
[f] Mean number of nanoparticles per liposome

From the results reported in tables 3.5 and 3.6, we can see that the loading of citrate-coated ferrite NPs embedded in liposomes is more effective compared to the loading obtained for uncoated nanoparticles. The higher loading of citrate-coated NPs is reasonably due to their higher stability in buffer medium at pH 7.4 with respect to uncoated NPs.

Magnetoliposomes embedded with citrate-coated nanoparticles (sample A in Table 3.6) were also characterized by Cryo-TEM acquisition. Cryo-TEM images (Figure 3.17) show that only some of the vesicles contain magnetic nanoparticles in their aqueous pool, while others are completely empty. Moreover the entrapped

nanoparticles present aggregation, while no specific interaction with the lipid bilayer can be seen.

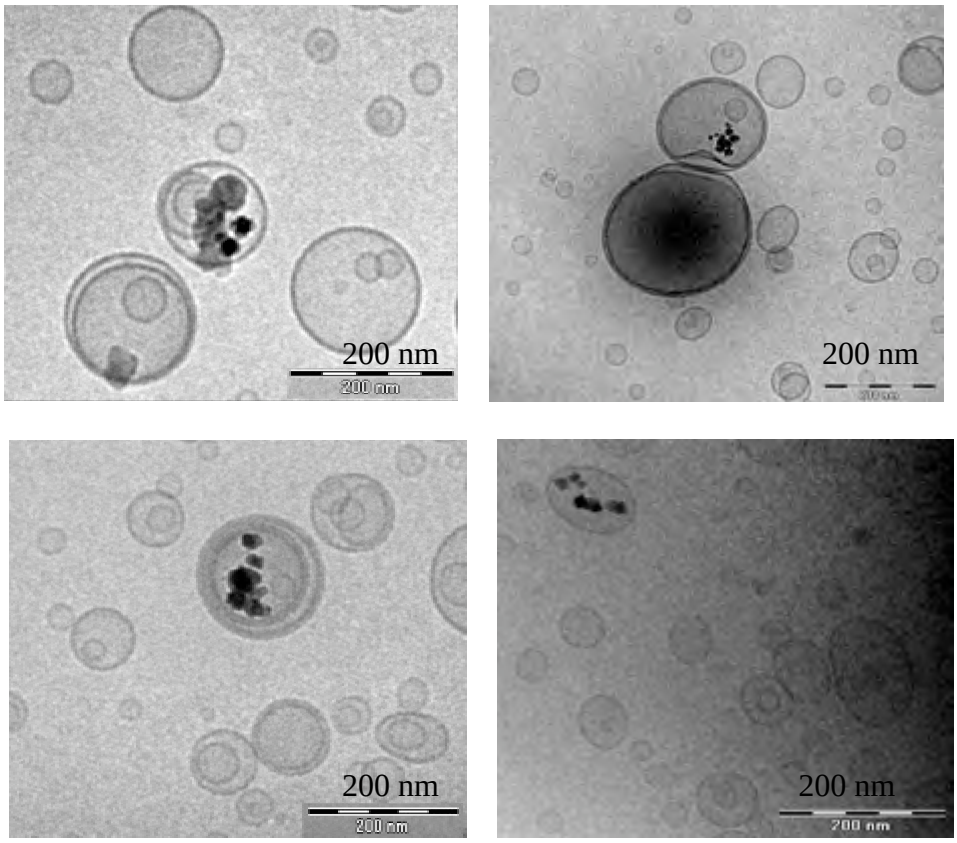

Figure 3.17. Cryo-TEM images of magnetoliposomes embedded with citrate-coated Cobalt-ferrite nanoparticles (sample A in table 3.6)

3.5.2 Magnetoliposomes with hydrophobic nanoparticles

The main features of the investigated samples of magnetoliposomes with oleic acid-coated nanoparticles entrapped in lipid bilayers of vesicles are reported in Table 3.7.

In order to understand how magnetic nanoparticles interact with the lipid bilayer of magnetoliposomes, SAXS experiments were carried out on both liposome (control sample) and magnetoliposome samples.

Table 3.7. Oleic acid-coated cobalt-ferrite nanoparticle loading in the liposomes

MLs	[Nps] (mg/L)[a]	<R>[b] (nm)	<R_H>[c] (nm)	PC/$CoFe_2O_4$ [w/w][d]	Encapsulation Percentage [e]
A	26.0±0.3	7.44±0.1	83.5±1.0	550:1	41.7
B	94.0±1.0	7.44±0.1	85.5±1.5	150:1	57.4
C	192.0±2.0	7.44±0.1	86.0±1.5	75:1	60.2
D	205.0±2.0	7.44±0.1	81.5±1.0	110:1	64.1

[a] $CoFe_2O_4$ concentration by ICP-OES after GEC purification
[b] Average radius of nanoparticles by SAXS analysis
[c] Average hydrodynamic radius of MLs from DLS by CONTIN analysis
[d] Weight ratios between phospholipids and nanoparticles
[e] $\{[CoFe_2O_4]_{\text{after GEC}}/[CoFe_2O_4]_{\text{before GEC}}\}\times 100$

SAXS spectra (reported in Figure 3.18) have been fitted according to a model proposed by Nallet *et al*[17] for lamellar phases of amphiphilic bilayer, through the following equation:

$$I(Q) = \frac{2\pi P(Q)}{2(\delta_H + \delta_T)q^2} \quad (3.5)$$

where the form factor is given by:

$$P(Q) = \frac{4}{q^2}\left\{\Delta\rho_H\left[\sin\left[q(\delta_H + \delta_T)\right] - \sin(q\delta_T)\right] + \Delta\rho_T \sin(q\delta_T)\right\}^2 \quad (3.6)$$

and δ_H is the head group thickness, δ_T is the tail length, $\Delta\rho_H$ (ρ_H - ρ_{solv}) and $\Delta\rho_T$ (ρ_T - ρ_H) are the scattering length density contrast, where ρ_H , ρ_T and ρ_{solv} are the scattering length density of head group, tail and solvent, respectively. In this model no inter-lamellar structure factor S(Q) is included.

SAXS spectrum of magnetoliposomes has been modelled according to the following equation:

$$I(Q) = I_{liposomes} + I_{MagNPs} + I_{bkg} \quad (3.7)$$

where $I_{liposomes}$ is the scattering intensity from the liposomes, while I_{MagNPs} is the scattering intensity arising from magnetic nanoparticles arranged in fractal clusters and modelled according to the pearl

necklace model[18]. We previously used this model to describe polydisperse spherical nanoparticles with a core-shell structure, arranged into fractal clusters[19]. The spherical particles have a constant shell thickness and a core with a Schulz distribution of radii[19,20]. The contribution to the total scattering intensity arising from these objects was calculated according to:

$$I_{MagNPs} = \phi P(Q) S(Q) \tag{3.8}$$

where ϕ is the particle volume fraction, P(Q) is the form factor and S(Q) is the interparticle structure factor accounting for the interparticle correlations. The form factor was modelled as:

$$P(Q) = (1/V_p)\int_0^\infty G(r_c) F^2(Qr_c) dr_c \tag{3.9}$$

$$F(Qr_c) = (4\pi/Q^3)(\rho_{shell} - \rho_{core})\{\rho_{scaled} j[Qr_c + (t/r_c)Qr_c] - j(Qr_c)\} \tag{3.10}$$

$$\rho_{scaled} = (\rho_{solv} - \rho_{shell})(\rho_{core} - \rho_{shell}) \tag{3.11}$$

$$j(Qr_c) = \sin(Qr_c) - (Qr_c)\cos(Qr_c) \tag{3.12}$$

where r_c is the core radius, t is the shell thickness, V_p is the particle volume, and ρcore, ρ_{shell} and ρ_{solv} are the scattering length densities (SLDs) of the core, shell and solvent, respectively. The function $G(r_c)$ is the normalized probability of finding a particle with a core radius between r_c and $r_c + dr_c$, and it accounts for the polydispersity of the cores according to a Schultz distribution[10,21].

$$G(rc) = \frac{r_c^{\,Z}}{\Gamma(Z+1)}\left(\frac{Z+1}{\langle r_c\rangle}\right)^{Z+1} \exp\left[-\frac{r_c}{r_{avg}}(Z+1)\right] \tag{3.13}$$

where $\Gamma(Z + 1)$ is the gamma function and the parameter Z is related to the polydispersity σ_c of the core radius by the expression:

$$\sigma_c = \frac{(\langle r_c^2\rangle - \langle r_c\rangle^2)^{1/2}}{\langle r_c\rangle} = \frac{1}{(Z+1)^{1/2}} \tag{3.14}$$

The interparticle structure factor S(Q) describes how the scattering intensity is modulated by interference effects between radiation scattered by different scattering objects. In our case, it should account for the aggregation of the magnetic nanoparticles, in analogy

with the distribution of micelles along the polypeptide backbone. Therefore, we used the same expression derived by Chen and Teixeira[18]:

$$S(Q) = 1 + \frac{D\Gamma(D-1)}{(Qr)^D}\sin[(D-1)\tan^{-1}(Q\xi]\left(1+\frac{1}{Q^2\xi^2}\right)^{(1-D)/2} \qquad (3.15)$$

where r is the mean radius of the particles as resulting from the sum of the core radius r_c and the shell thickness t, Γ is the gamma function and ξ is the correlation length, i.e. a cut-off factor related to the dimensions of the aggregates that are eventually formed by the particles. D is the fractal dimension that describes the spatial distribution of the individual scatterers and it is related to their number N(R) within a sphere of radius R through the equation:

$$N(R) = (R/r)^D \qquad (3.16)$$

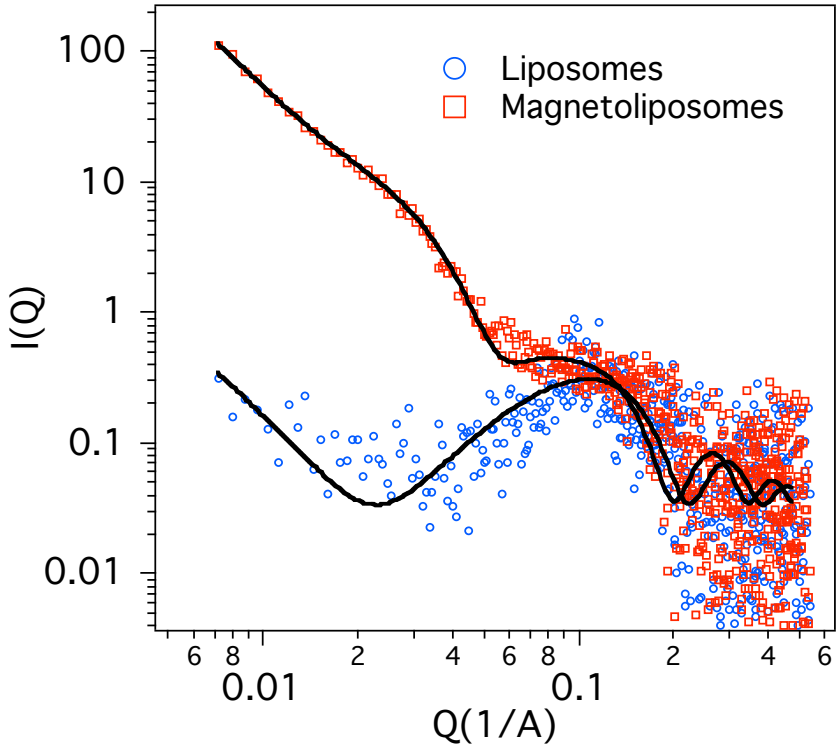

Figure 3.18. SAXS spectra of liposome (PC 15 mg/ml) and magnetoliposome (sample C in Table 2) solutions. The best fittings are reported as solid lines.

Fitting results (reported in Table 3.8) show that the presence of the magnetic nanoparticles does not affect the structure of the bilayer, as the experimental SAXS curve is well fitted by the sum of nanoparticle and bilayer contributions. This schematically corresponds to the physisorption of aggregates (average dimension around 25 nm) of magnetically nanoparticles onto the lipid bilayer.

Table 3.8. Structural parameters of liposomes and magnetolipomes by SAXS analysis

	Liposomes	Magnetoliposomes
Lipid head group thickness, δ_H [Å]	4.5	4.5
Lipid tail length, δ_T [Å]	17.8	17.8
$CoFe_2O_4$ mean core radius, <R> [Å]	_____	51.5
$CoFe_2O_4$ shell thickness, t [Å]	_____	38.1
$CoFe_2O_4$ core polidispersity, σ_e	_____	0.29
$CoFe_2O_4$ fractal dimension, D	_____	2.6
$CoFe_2O_4$ correlation length, ξ [Å]	_____	255.0

3.6 Giant Unilamellar Vesicles (GUVs)

Materials: L-α phosphatidylcholine egg yolk Grade 1 (99.9% TLC) in chloroform (PC) was purchased from Lipid Products. Alexa Fluor 488-C5 maleimide and $DiIC_{18}$ (1,1'-dioctadecyl-3,3,3',3'-tetramethylindocarbocyanine perchlorate) were purchased from Invitrogen Molecular Probes. D(+)-Sucrose (≥ 99.5% HPLC) and D-(+)-Glucose (≥ 99.5% HPLC, sum of enantiomers) anhydrous were purchased from Fluka.

GUVs were prepared using the electroformation method, originally developed by Angelova and Dimitrov by using a homemade chamber prepared by assembling two Indium Tin Oxide (ITO)-coated microscope slides separated by an O-ring spacer (see Methods).
The lipid was dissolved in chloroform (PC, 5 mg/ml) with 0.1% mol of the fluorescent probe $DiIC_{18}$ (excitation and emission wavelengths are 549 and 565 nm, respectively). A volume of 15 μl of lipid stock solution was spread on each conducting face of ITO-coated microscope slides and then dried under vacuum for at least 2 h in order to remove solvent. An O-ring was positioned around the film, and the two slides were sandwiched to form a chamber where GUV growth took place. The chamber was then filled with a buffer solution (volume 350 μl) of Alexa 488-C5-maleimide 5 μM in sucrose 0.23 M and equilibrated at room temperature. Magnetic GUVs were prepared by adding citrate coated NPs in buffer in order to have nanoparticles and lipid in molar ratio of 2:1.
An analogue preparation was used by adding magnetic and fluorescent nanoparticles of $MP@SiO_2$(RITC) in order to detect their location on GUVs. Finally, the chamber was connected to a function

generator and a low-frequency AC electric field (sinusoidal wave with a frequency of 10 Hz and amplitude of 2 V) was applied for 3 h. GUV growth was monitored by optical microscopy and, when complete, the solution was gently removed from the electro-formation chamber. To reduce the fluorescence from Alexa molecules not confined within the GUV, samples were diluted 15 times with an iso-osmolar solution of glucose 0.23 M. The density difference between sucrose (inner pool) and glucose (external medium) lead to GUV deposition, helping in microscopy observation.

The diameter of the vesicles obtained by electro-formation method ranged from 5 to 50 μm[22]. A CLSM image of a fluorescent GUV labeled with the lipophilic marker $DiIC_{18}$ (red) and filled with the water-soluble Alexa dye is reported in Figure 3.19.

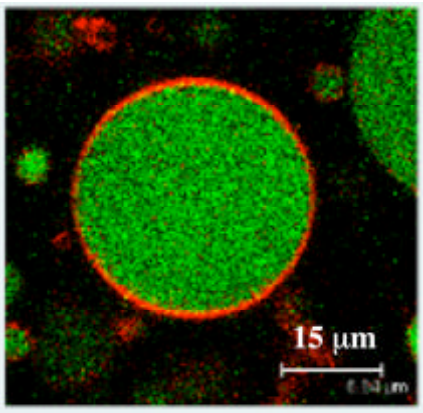

Figure 3.19. CLSM image of a GUV labeled with $DiIC_{18}$ (red) and filled with Alexa dye (green)

3.6.1 GUVs in the presence of MP@SiO_2(RITC)

CLSM images of magnetic and fluorescent GUVs are reported in Figure 3.20, showing that MP@SiO_2(RITC) nanoparticles are adsorbed on the surface of GUVs'bilayer.

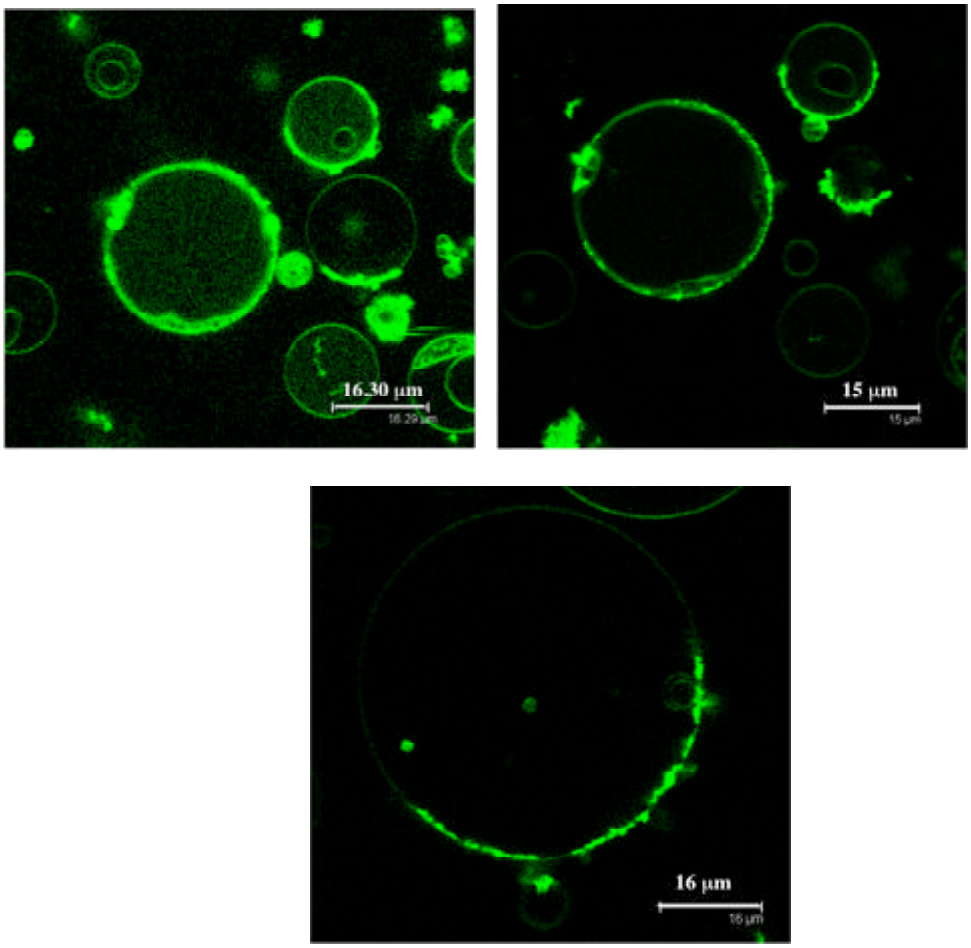

Figure 3.20. CLSM images of magnetic GUVs prepared by electroformation in the presence of MP@SiO_2(RITC).

Three-dimensional projection obtained assembling with Leica software confocal slices (thickness 0.366 µm) of magnetic GUVs indicates that MP@SiO_2(RITC) were not homogeneously distributed on the membrane surface of the vesicles (Figure 3.21).

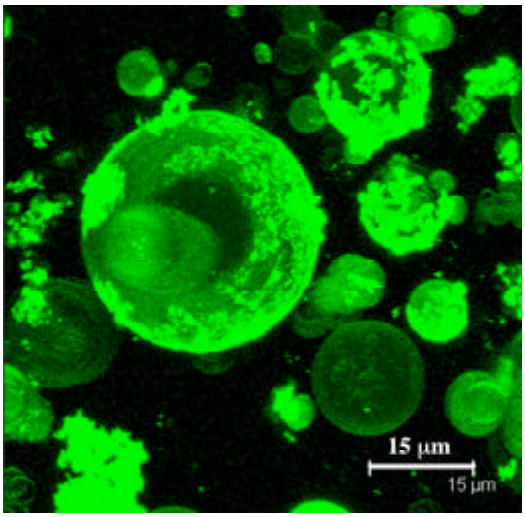

Figure 3.21. Three-dimensional projection (max fix treatment) of magnetic GUVs prepared by electroformation in the presence of MP@SiO_2(RITC).

Intensity line profiles of different regions of GUV membrane (Figure 3.22) confirm that the magnetic particles are not uniformly distributed on the lipid bilayer of vesicles, evidencing larger thickness (ranging between 1 and 4 μm) and higher fluorescent intensity where MP@SiO_2(RITC) are adsorbed. Moreover, confocal xyλ-scans of magnetic GUVs were performed to analyze the different fluorescence spectra in different regions of the membrane, depending on MP@SiO_2(RITC) adsorption, evidencing higher fluorescent intensity (maximum emission around λ= 586 nm) in the presence of larger amounts of adsorbed nanoparticles. These results were compared with the ones obtained with GUVs hydrated with a solution of free APTES-RITC in sucrose 0.23 M. Differently from magnetic GUVs, RITC-labeled GUVs images show a uniform distribution of the fluorescent dye on the lipid bilayer of vesicles, evidencing the same membrane thickness (around 0.5 μm) over the entire surface of GUVs (Figure 3.23).

Empty and non-fluorescent GUVs, also prepared in sucrose, were mixed to MP@SiO_2(RITC) in a way to have [$CoFe_2O_4$]/[PC] = 2 and analyzed by CLSM in order to detect the effect of an external addition of magnetic particles to pre-formed GUVs.

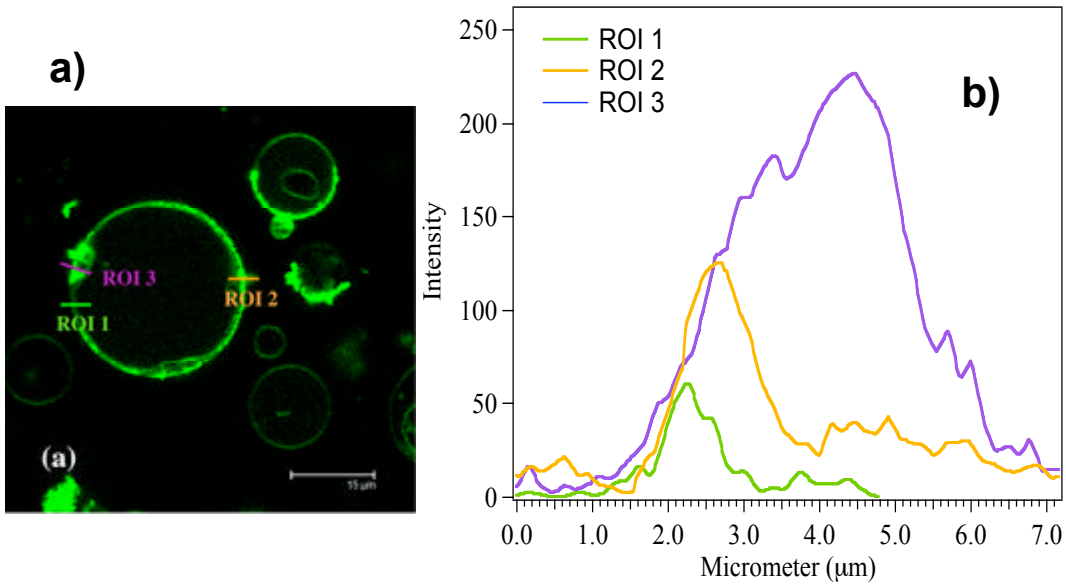

Figure 3.22. (a) Different regions (ROI) of GUV membrane prepared in the presence of MP@SiO_2(RITC) (b) intensity line profile spectra of the three different regions of magnetic GUV membrane.

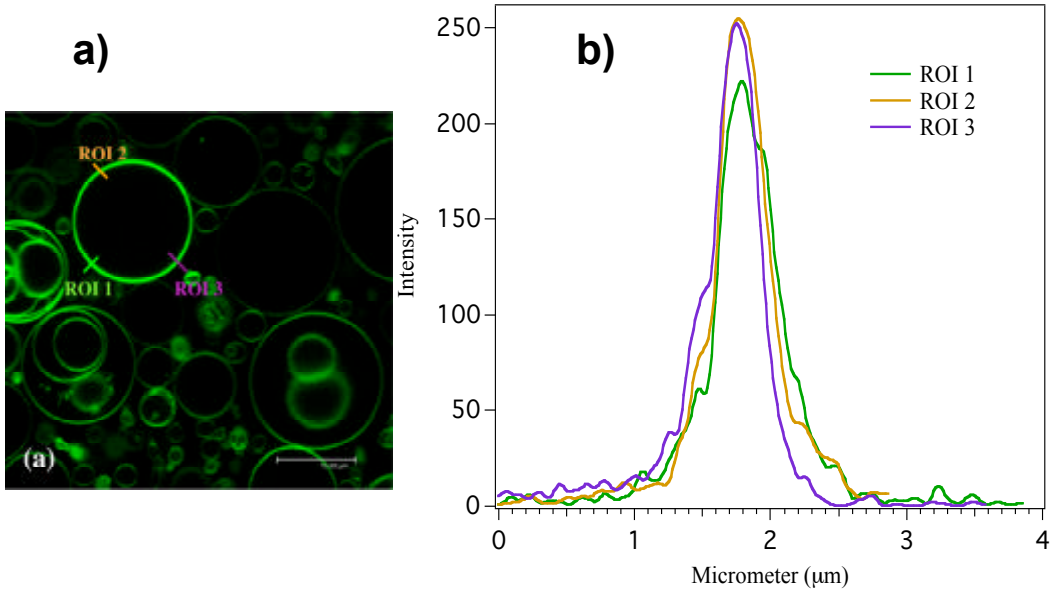

Figure 3.23. (a) Different regions (ROI) of GUV membrane labeled with APTES-RITC (b) intensity line profile spectra of the three different regions of RITC-labeled GUV membrane.

Confocal image reported in Figure 3.24 of pre-formed GUVs in the presence of MP@SiO_2(RITC) shows the formation of large aggregates of magnetic particles and the appearance of some vesicles after the addition of fluorescent and magnetic nanoparticles to the empty GUV solution. A shape deformation of some GUVs is observed in the regions where MP@SiO_2(RITC) were present in larger amounts.

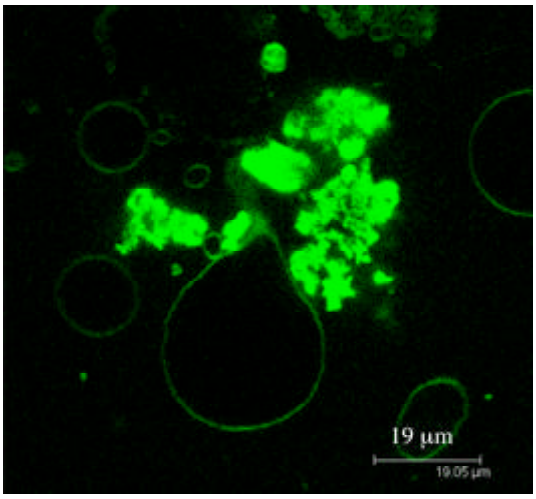

Figure 3.24. CLSM image of pre-formed GUVs to which MP@SiO_2(RITC) were added.

3.7 References

(1) Massart, C. R. *Acad. Sci. Ser. C* 1980, *291*, 1-3.
(2) Massart, C. R. *IEEE Trans. Magn.* 1981, *17*, 1247-1248.
(3) Bonini, M.; Wiedenmann, A.; Baglioni, P. *J. Phys. Chem. B* 2004, *108*, 14901-14906.
(4) Bonini, M.; Wiedenmann, A.; Baglioni, P. *Physica A* 2004, *339*, 86-91.
(5) Bartlett, P.; Ottewill, R. H. *Journal of Chemical Physics* 1992, *96*, 3306-3318.
(6) Schulz, G. V. *J. Phys. Chem.* 1935, *43*, 25.
(7) Morais, P. C.; Santos, R. L.; Pimenta, A. C. M.; Azevedo, R. B.; Lima, E. C. D. *Thin Solid Films* 2006, *515*, 266-270.
(8) Sahoo, Y.; Goodarzi, A.; Swihart, M. T.; Ohulchanskyy, T. Y.; Kaur, N.; Furlani, E. P.; Prasad, P. N. *Journal of Physical Chemistry B* 2005, *109*, 3879-3885.
(9) Schroeder, A.; Avnir, Y.; Weisman, S.; Najajreh, Y.; Gabizon, A.; Talmon, Y.; Kost, J.; Barenholz, Y. *Langmuir* 2007, *23*, 4019-4025.
(10) Hayter, J. B.; Penfold, J. *Mol. Phys.* 1981, *42*, 109.
(11) Verhaegh, N. A. M.; Vanblaaderen, A. *Langmuir* 1994, *10*, 1427-1438.
(12) Lu, Y.; Yin, Y. D.; Mayers, B. T.; Xia, Y. N. *Nano Letters* 2002, *2*, 183-186.
(13) Lesieur, S.; Grabielle-Madelmont, C.; Menager, C.; Cabuil, V.; Dadhi, D.; Pierrot, P.; Edwards, K. *J. Am. Chem. Soc.* 2003, *125*, 5266-5267.
(14) Martina, M.-S.; Fortin, J.-P.; Menager, C.; Clement, O.; Barratt, G.; Grabielle-MAdelmont, C.; Gazeau, F.; Cabuil, V.; Lesieur, S. *J. Am. Chem. Soc.* 2005, *127*, 10676-10685.
(15) Sabate, R.; Barnadas-Rodriguez, R.; Callejas-Fernandez, J.; Hidalgo-Alvarez, R.; Estelrich, J. *Intern. J. Pharma.* 2008, *347*, 156-162.
(16) Steward-Marshall, J. C. *Anal. Biochem.* 1980, 10-14.
(17) Nallet, F.; Laversanne, R.; Roux, D. *Journal De Physique Ii* 1993, *3*, 487-502.
(18) Chen, S. H.; Teixeira, J. *Physical Review Letters* 1986, *57*, 2583-2586.
(19) Bonini, M.; Fratini, E.; Baglioni, P. *Materials Science & Engineering C-Biomimetic and Supramolecular Systems* 2007, *27*, 1377-1381.
(20) Kline, S. R. *Journal of Applied Crystallography* 2006, *39*, 895-900.
(21) Hayter, J. B. *Edited by V. DeGiorgio & M. Corti. Amsterdam:*

North Holland 1983, 59-93.
(22) Ambroggio, E. E.; Separovic, F.; Bowie, J. H.; Fidelio, G. D.; Bagatolli, L. A. *Biophysical Journal* 2005, *89*, 1874-1881.

4 - Drug release

4.1 Magnetoliposomes embedded with hydrophilic nanoparticles

The release of Carboxyfluorescein (CF) from magnetoliposomes embedded with hydrophilic magnetic nanoparticles was monitored as the increase of fluorescence emission of CF (see Methods). The leakage has been measured as a function of the field frequency (0.2 kHz, 2.84 kHz and 5.82 kHz), the time of exposure (10, 20 and 50 min) to the field and concentration of the loaded magnetic nanoparticles.

Although the release results obtained from magnetoliposomes embedded with uncoated magnetic NPs were very promising, their loading and their encapsulation efficiency were quite low with respect to the citrate-coated ones (see Drug-carriers, Tables 3.5 and 3.6). Furthermore, the stability of the system was strongly affected by the presence of uncoated NPs, as shown by the appearance of a black precipitate after few days. The precipitation of aggregates induced by uncoated $CoFe_2O_4$ NPs is a limit to biomedical applications: in fact, large particles are easily sequestered by the spleen and eventually removed by the cells of the phagocyte system, resulting in decreased circulation time.

For these reasons magnetoliposomes loaded with citrate-coated $CoFe_2O_4$ NPs appear more promising for drug delivery applications,

so I have mainly reported the release results obtained with these magnetoliposomes, which have a higher stability during time and optimized release conditions.

However, both magnetoliposome samples (loaded with uncoated or citrate-coated NPs) have shown a significant increase in their permeability upon LF-AMF application with respect to a control sample without nanoparticles and have shown similar release results. A comparison between the release from liposomes loaded with citrate-coated Cobalt-ferrite NPs (sample C in Table 3.6) and liposomes loaded with the uncoated ones (sample A Table 3.5) prepared at the same concentration (about 200 mg/l of $CoFe_2O_4$) and exposed to the field (5.8 kHz for 50 minutes) has been reported in Figure 4.1.

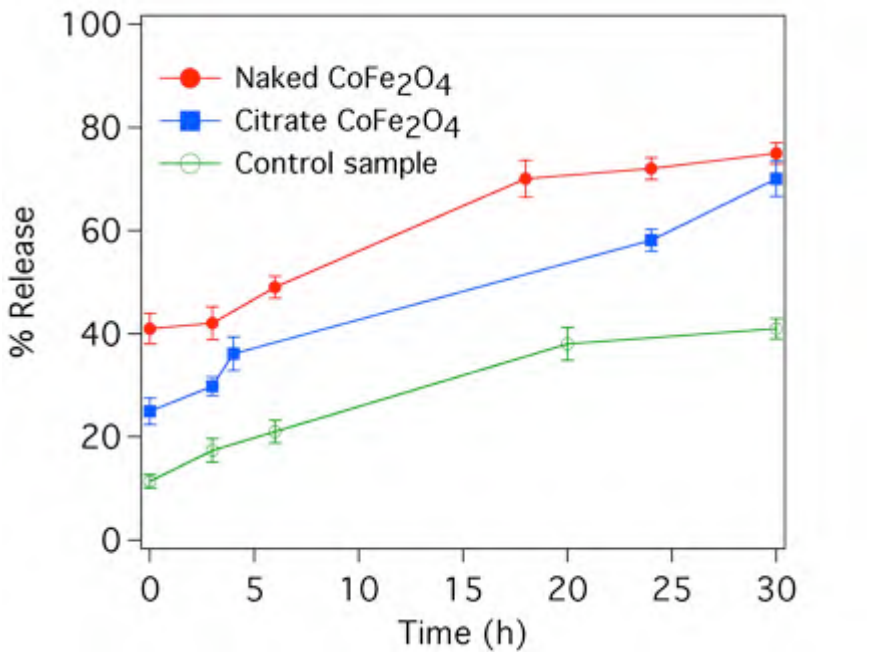

Figure 4.1. Release curves of control sample, uncoated and citrate coated nanoparticles-loaded liposomes after LF-AMF exposure at 5.82 kHz for 50 minutes.

Immediately after the LF-AMF exposure magnetoliposmes loaded with citrate nanoparticles appear less sensitive to the magnetic field (about 25% of CF release) with respect to uncoated nanoparticles-embedded

vesicles (over 40% of CF release). However, after 30 hours, both magnetoliposome solutions reach nearly 60% of CF release. The different behaviour between equally loaded magnetoliposomes can be explained by taking into account two factors. First, uncoated magnetic NPs are expected to have a higher electrostatic interaction with the bilayer as their surface charge is not screened by the citrate counterions. This would suggest a preferential location of the nanoparticles next to the bilayer, resulting in the enhancement of the hyperthermic effect. Secondly, the uncoated magnetic nanoparticles form large aggregates in the buffer solution. In presence of an anisotropic magnetic field, as in the case of our home-made apparatus (see Methods), magnetic nanoparticles are trailed in opposite directions during the alternating magnetic field cycles. Larger particles strongly affect the lipid bilayer permeability causing the formation of pores when they hit the liposome membrane during these oscillations at the applied magnetic field frequency, promoting CF release, without the rupture of the vesicles. This was confirmed by DLS analysis that shows no significant changes in the total scattered intensity and in the evaluated size distributions. The results reported below are referred to magnetolipoosmes loaded with citrate-coated NPs, but similar release trends were obtained with the uncoated ones.

Magnetoliposomes have shown higher release at longer exposure times with respect to the empty liposomes, especially when the LF-AMF is applied for at least 50 minutes. The results, reported in Figure 4.2a, show about a 10% increase after 10 and 20 minutes of treatment, while nearly 30% increase after 50 minutes of treatment was observed. CF release increases in all the samples during time. In particular, 30 hours after the LF-AMF application, all samples reached about 50-60% of release. The comparison between the control samples (liposomes without magnetic NPs) exposed to LF-AMF for 50 minutes at the highest frequency of oscillation and those

containing magnetic NPs show that the release is almost the same for the control samples and the 10-20 minutes treated samples, especially during the first hours.

Concerning the effect of field frequency, a higher release at high frequencies for the longer exposure time (Figure 4.2b) was observed. However, the initial percentage of CF release in magnetoliposomes exposed for 50 minutes at 0.2 kHz and 2.84 kHz of field frequency is below 10% and increases up to 50% after 30 hours, similarly to what observed for the control sample (blank in figure 4.2). On the other hand, at the frequency of 5.82 kHz the percentage of release is higher (about 30%) and it reaches nearly 60% after 30 hours.

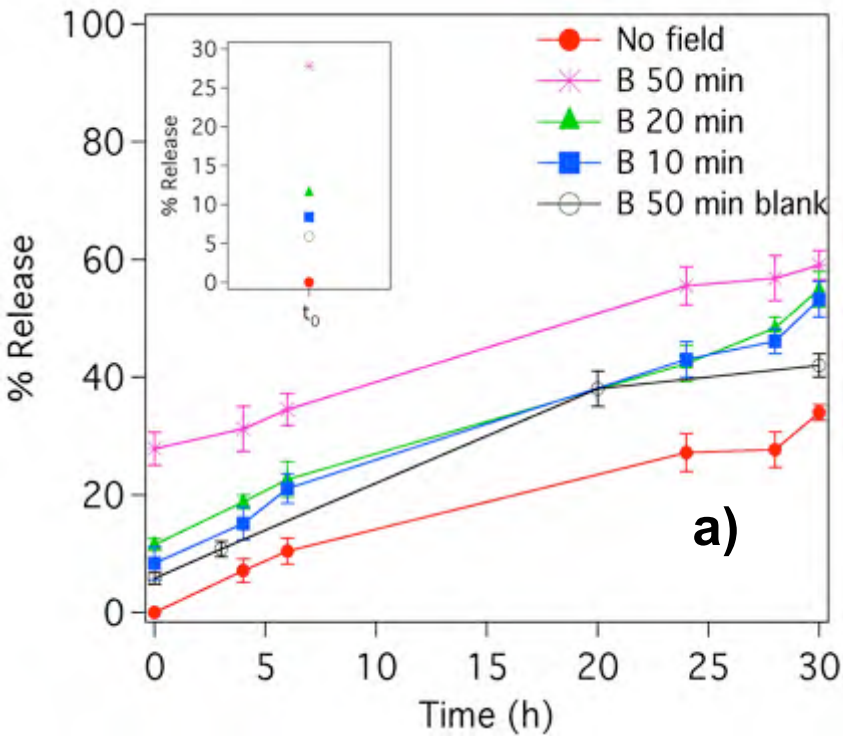

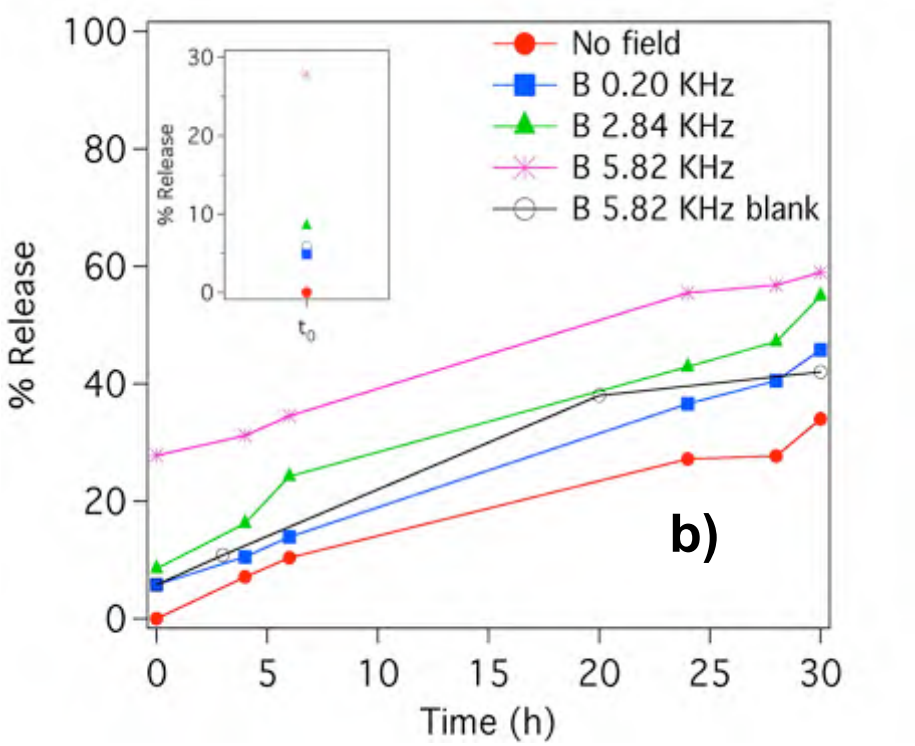

Figure 4.2. Release of CF-loaded magnetoliposomes (sample C in Table 3.6) in the presence of LF-AMF as a function of (a) exposure time at 5.82 kHz and (b) of field frequency for 50 minutes of treatment. An enlargement of the release% at $t=t_0$ is shown in the inset.

The release curves of samples with different loading of citrate-coated $CoFe_2O_4$ nanoparticles are reported in Figure 4.3, which shows that CF release is independent of magnetic fluid concentration. The percentage of release is almost the same for all the samples (Table 3.6) exposed to 5.82 kHz field frequency for 50 minutes. After 30 hours the release in liposomes with the lowest magnetic loading is even higher.

This behaviour is different from what we have observed for liposomes loaded with uncoated nanoparticles, which have shown an increase of the percentage of release at higher NP concentrations. However, uncoated NP loadings are lower than the citrate-coated ones.

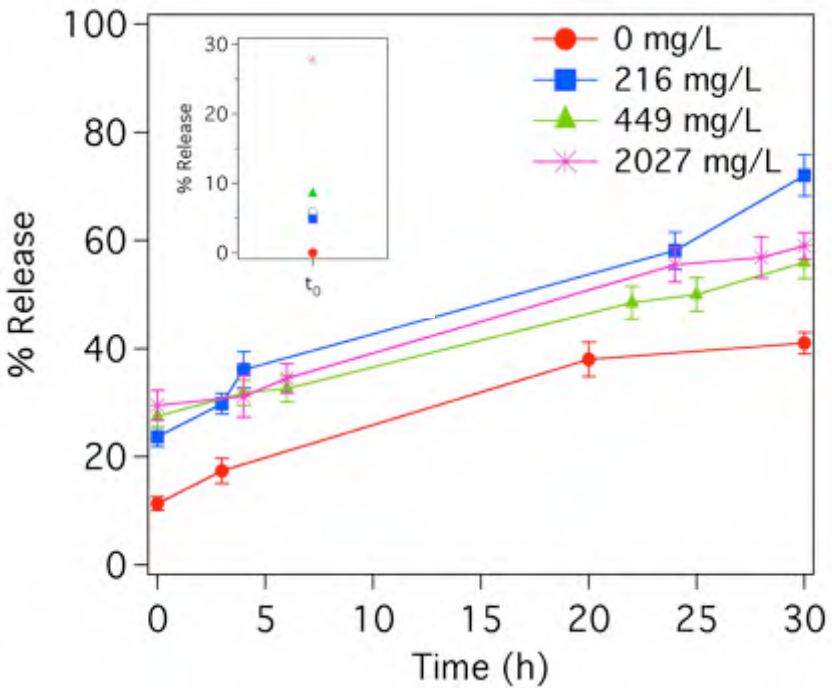

Figure 4.3. Release curves of CF-loaded magnetoliposomes at different $CoFe_2O_4$ content. The characteristics of these samples are reported in Table 3.6 where they are labeled as A, B, C, respectively.

Upon exposure to the LF-AMF, both magnetoliposomes and control liposomes have shown a continuos increase of temperature with time due both to the heat dissipation from the coil and hyperthermic effects from the NPs. The temperature increase is slightly higher at higher magnetic fluid loading, showing that the hyperthermic heating is significant. To evaluate the effect produced by the heating of the coil, control experiments on both magnetoliposomes and control liposomes, incubated at the highest temperature produced by the oscillating field for the total exposure time, have been performed to take into account the temperature contribution. We have observed that magnetoliposomes and control samples (empty liposomes) have similar release trend as a function of temperature increase. The overall increase due to the

temperature is never higher than 30% as shown in Figure 4.4 (a, b) and it is lower with respect to the release percentage due to the magnetic field exposure.

Therefore, it is very complicated to distinguish the temperature contribution from the release enhancement due to the LF-AMF application, though the latter is slightly dominant. From a comparison with the results obtained for liposomes loaded with uncoated nanoparticles, we observe that the temperature increase is proportional to the nanoparticles' loading, independently of the presence of the citrate coating, according to the presence of a hyperthermic effect.

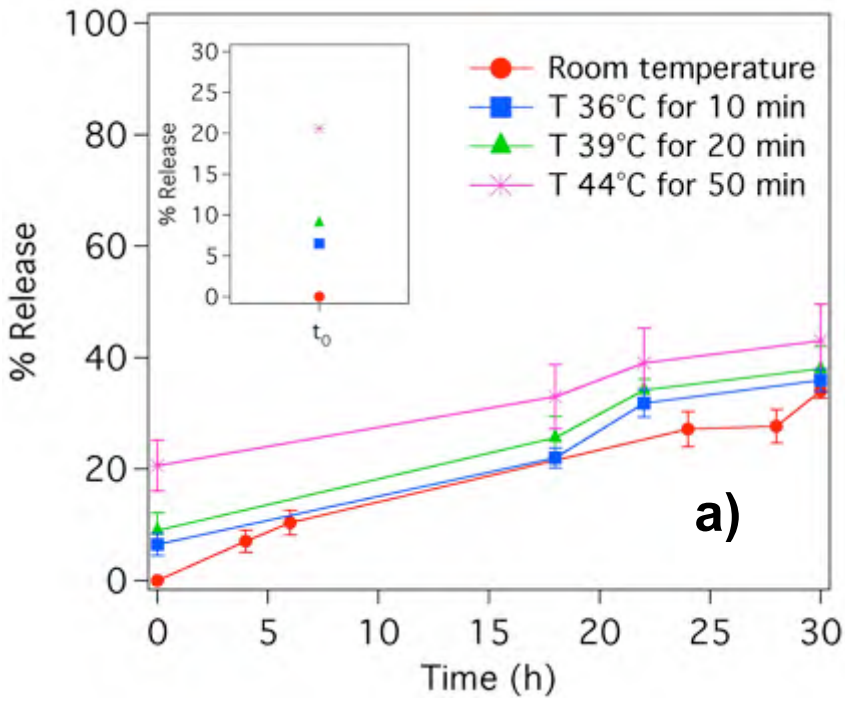

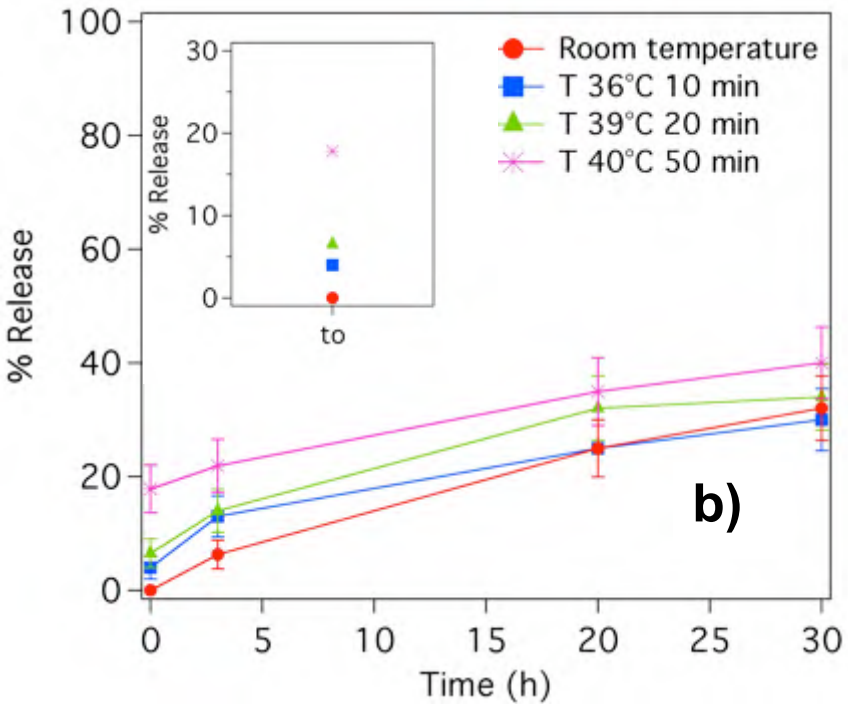

Figure 4.4. Release curves of (a) CF-loaded magnetoliposomes (sample C in Table 3.6) and (b) control liposomes incubated at the temperature indicated in the figure legend

In order to gain a deeper understanding of the magnetic response of citrate NPs loaded liposomes, AC susceptibility measurements on a high loading sample (sample C in Table 3.6) were carried out. Variable temperature AC measurements on ferrofluids can yield precious information on the mobility of magnetic cores in solution, and on the nature of the mechanism, underlying the liposome membrane disruption process at frequencies close to that of LF-AMF irradiation.

The AC experiment was carried out by scanning the temperature from 5 K to 310 K in a frequency range of 0.5-1000 Hz with an amplitude of the oscillating magnetic field of 3.5 Oe (Figure 4.5). Above ca. 150 K a frequency dependent signal arises in the in-phase (χ') component, indicating a Néel type spin relaxation. As expected, the signal increases with temperature. This behaviour is

in good agreement with AC measurements on powder indicating that a large fraction of particles is still blocked at room temperature.

For high frequency AC fields (n>10 Hz), χ' increases steadily with temperature up to 310 K, while a sharp peak appears in the 270-290 K area for low frequency AC fields: this has to be ascribed to a minority of particles that are free to rotate under the action of the alternating field as the aqueous medium melts. However, at higher temperature the curves resume the trend observed in the frozen dispersion, confirming that the majority of particles is not mechanically affected by the oscillating field for frequencies higher than about 10 Hz. This is confirmed by the out of phase (χ") component of susceptibility, which features a sharp frequency-dependent peak in the melting temperature region in a background that, though more noisy, is compatible in the whole temperature range with the powder-like behaviour (i.e. mechanically blocked particles).

Altough this investigation was performed at frequencies lower than that of the optimal LF-AMF experiment (n=5.82 kHz), some conclusions can be inferred. Indeed it can be reasonably assumed that no significant difference in the magnetic behaviour is to be expected between the highest investigated frequency (1000 Hz) and 5820 Hz; thus it can be concluded that in LF-AMF conditions local hyperthermal heating effects are operative, which are mainly due to relaxation (Néel) losses and, for a minor component, to frictional (Brown) losses.

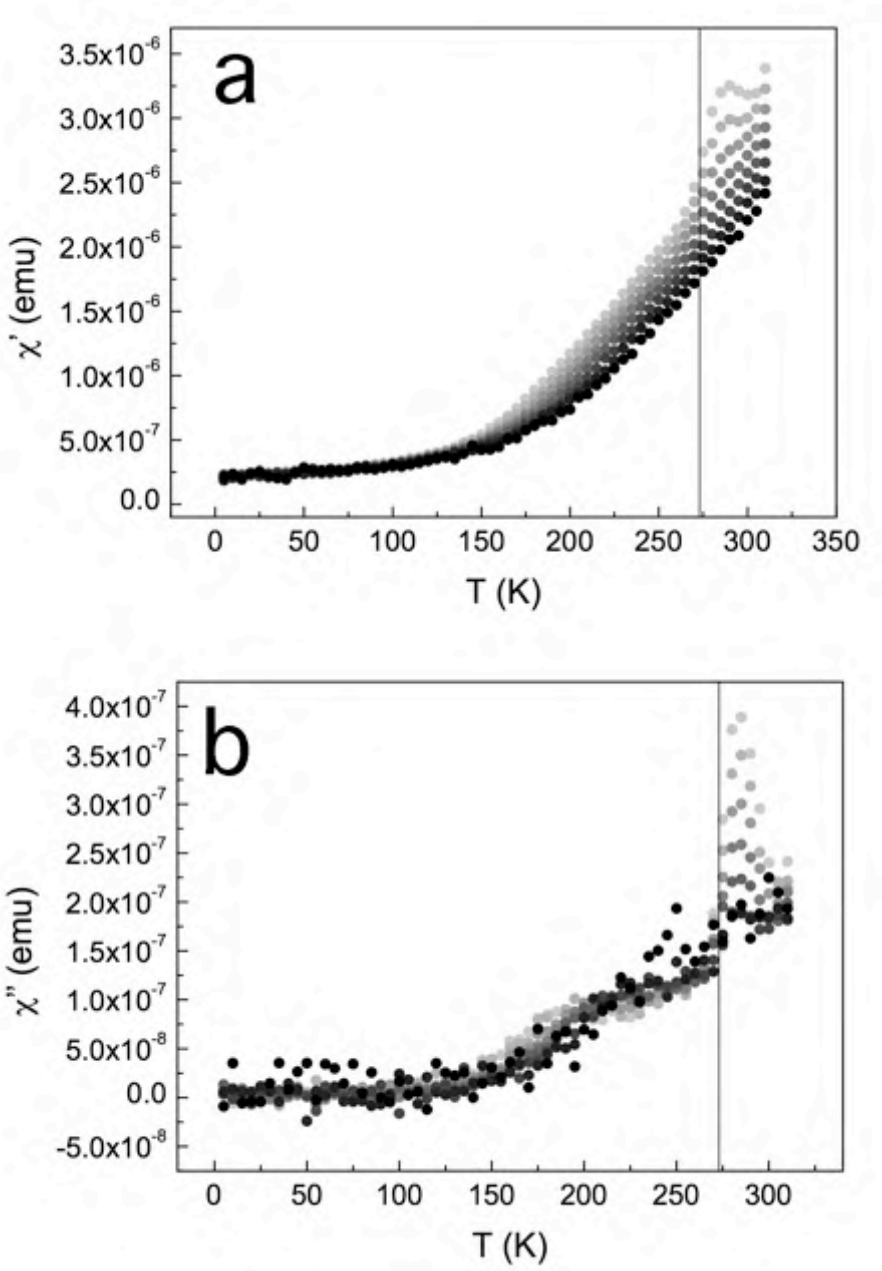

Figure 4.5. Temperature dependence of the in-phase (a) and out-phase (b) components of the magnetic susceptibility of a dispersion of liposomes loaded with citrate coated NPs (sample C in Table 3.6). Darker grey tones represent increasing frequencies from 0.5 to 1000 Hz; the solid line represents T= 273K.

As already introduced, in the case of magnetoliposomes loaded with uncoated Cobalt-ferrite Nps the effect of the size and charge of nanoparticles has been evaluated. Magnetoliposomes were

prepared in presence of both negatively and positively-charged uncoated nanoparticles to highlight possible interactions with liposome membrane that could enhance or inhibit the effect to LF-AMF exposure (samples C and F in Table 3.5). Release curves have shown that negatively charged nanoparticles are more effective in the same conditions (Figure 4.6a), consistently with a stronger interaction between positively charged phosphatidylcholine and negatively charged NPs, taking to an increased permeability of the membrane. The release is also enhanced by using larger uncoated nanoparticles (Figure 4.6b, samples D and E in Table 3.5). This can be explained by two separate effects. In the framework of the hypothesis we introduced when discussing the effect of the field frequency, bigger nanoparticles show a stronger response to the magnetic field, producing then bigger pores when magnetically collected next to the bilayer. Bigger NPs are also expected to generate more defects when exposed to oscillating magnetic fields, both due to their hindrance and to the heat they can produce.

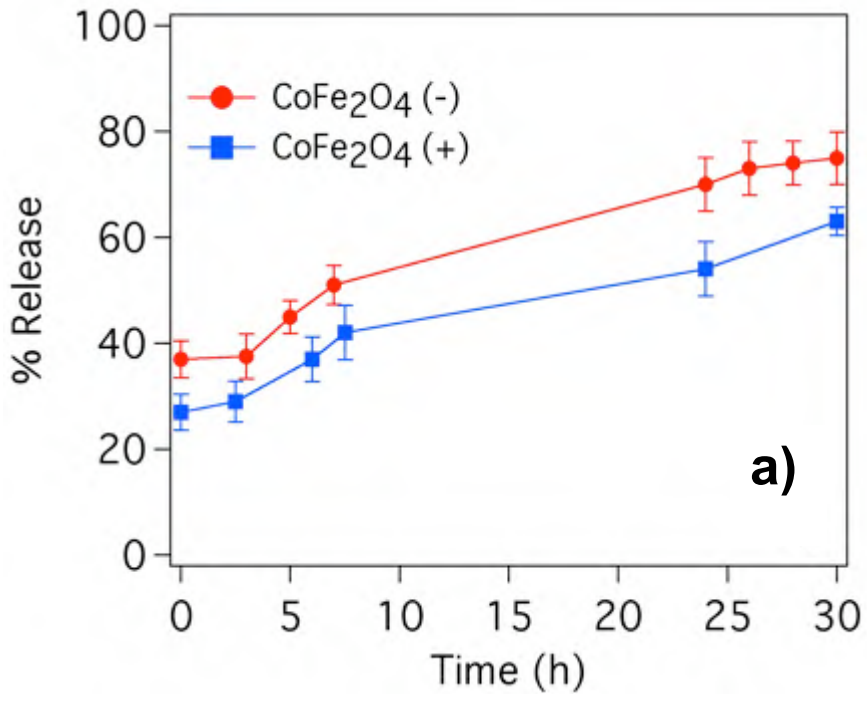

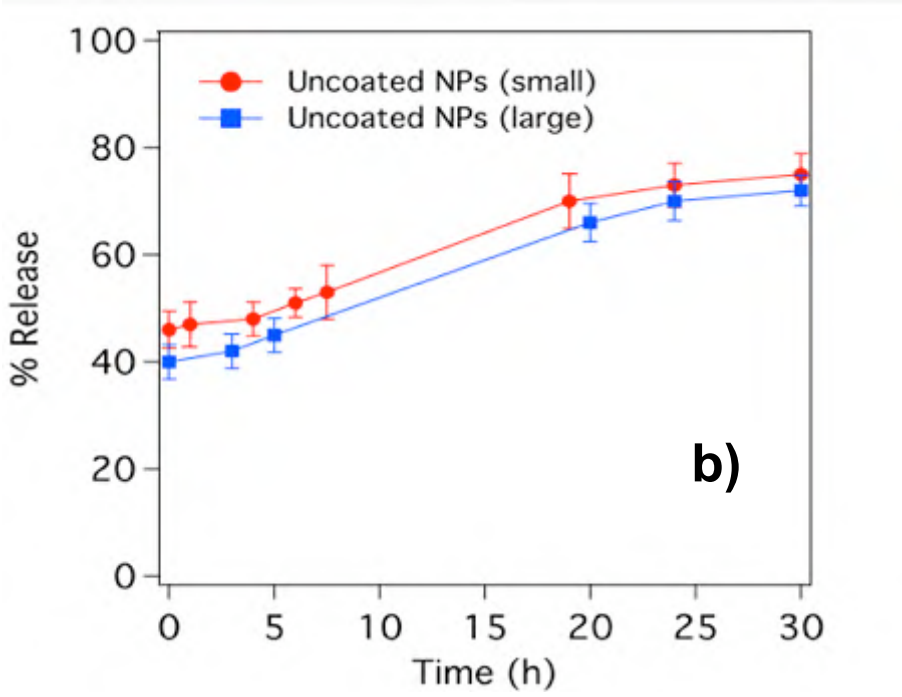

Figure 4.6. Release curves of CF-loaded magnetoliposomes after LF-AMF exposure at 5.82 kHz for 50 minutes as a function of (a) uncoated nanoparticle surface overall charge (samples C and F in Table 3.5) and (b) nanoparticle size (samples D and E in Table 3.5).

4.1.1 Drug release kinetics

In order to better understand the mechanism of CF release from magnetoliposomes loaded with magnetic nanoparticles, CF fluorescence intensity has been monitored during 1000 minutes. CF release has been investigated in LF-AMF treated and untreated magnetoliposomes and, for the sake of comparison, in heated samples. The fluorescence readings were normalized to the maximum fluorescence intensity of the solution by disrupting the liposomes with Triton-X 100. The experimental data were fitted using the Ritger-Peppas equation[1-3] widely used to analyze the release behaviour of various drug delivery systems[4-6].

Ritger-Peppas equation can be written as:

$$\frac{M_t}{M_\infty} = Kt^n \qquad \text{for } M_t/M_\infty < 0.6 \qquad (4.1)$$

where M_t/M_∞ is the drug fraction released at time t, K is the kinetic constant and n is the diffusion exponent that can be related to the drug transport mechanism. The power-law equation is the superposition of Fickian diffusion and the so-called "case-II transport"[1,3]: when n is between 0.40 and 0.50 (depending on the matrix geometry) the release follows Fickian diffusion, while "case-II transport" occurs for n≥1, leading to a zero-order release. For n values between 0.5 and 1, a so-called "anomalous transport" is observed and the two processes are coupled.

Occasionally, values of n>>1 has been observed and considered as kinetics dominated by erosion processes of the matrix ("supercase II transport"). This equation is generally used to analyze the release behaviour during the first 60% of the total release. However, equation 4.1 is based on the assumption that one of the above mentioned kinetic mechanism of release occurs as soon as the CF fluorescence intensity is measured. Ford and co-workers[7,8] introduced a correction to Ritger and Peppas equation for lag periods (l):

$$\frac{M_t}{M_\infty} = k(t-l)^m \qquad (4.2)$$

The lag period is the time required for the matrix to reach a sort of equilibrium before a new kinetic mechanism of release occurs, usually erosion or matrix disruption. Generally, lag periods in diffusion or dissolution cannot be ignored, despite they are relatively constant and small, when release mechanisms are described using exponential functions.

The experimental kinetic curves and the correspondent fittings obtained with magnetoliposomes loaded with citrate-coated (sample C of Table 3.6) and uncoated negative (sample C Table 3.5) Cobalt-ferrite NPs are reported in Figure 4.7a and 4.7b respectively.

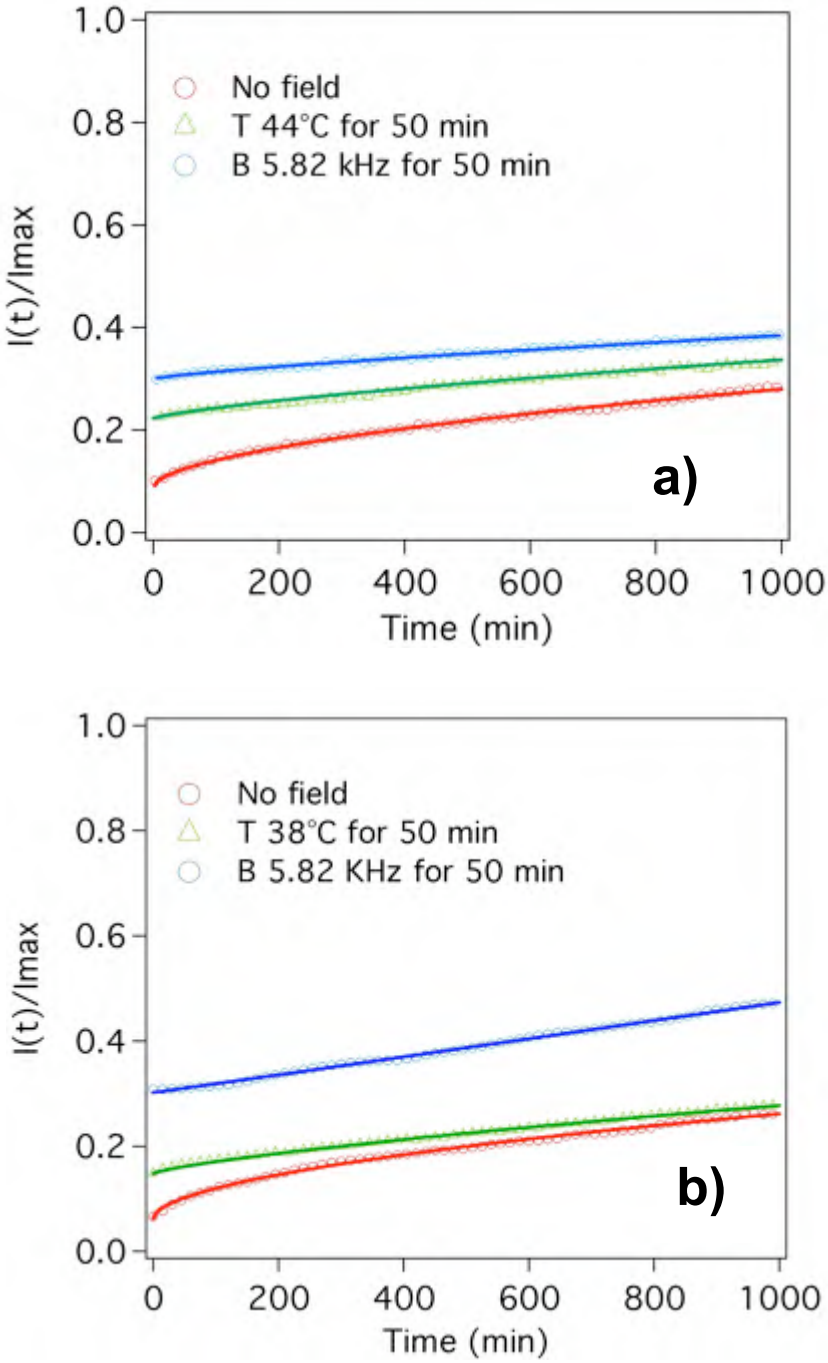

Figure 4.7. (a) Release curves of citrate coated $CoFe_2O_4$ NPs-embedded magnetoliposomes (sample C Table 3.6) in time drive mode and (b) release curves of uncoated negative $CoFe_2O_4$ NPs-embedded magnetoliposomes (sample C Table 3.5). (●) Untreated samples, (△) incubated at 44°C for 50 minutes, (○) samples subjected to LF-AFM for 50 minutes at a frequency of 5.82 kHz. Solid curves are the best fitting obtained by means of equation (4.1).

Kinetics parameters obtained from the analysis of the curves with equation (4.1) are shown in Table 4.1. For magnetoliposomes loaded with citrate-coated NPs, untreated samples are well fitted by equation (4.1) for n equal to 0.57±0.01 indicating that the dominant drug release mechanism is due to Fickian diffusion. The fit for magnetoliposomes exposed to LF-AMF and samples incubated at 44°C gives n=0.80±0.03 and n=0.72±0.01, respectively, indicating the combination of Fickian diffusion and initial membrane destabilization. The similar release kinetics obtained with LF-AMF and heated samples, indicates that both nanoparticle motions and temperature increase (arising from heat dissipation from the magnet and from the hyperthermic effect of NPs) induce an alteration of the lipid bilayer structure that enhances the CF-release.

For magnetoliposomes loaded with uncoated NPs, the fitting results give n equal to 0.55±0.01 for untreated samples, indicating Fickian diffusion, n = 0.76±0.01 for the samples incubated at 38°C, indicating the presence of anomalous transport, and n = 1.01±0.02 for LF-AMF exposed samples, indicating a zero-order kinetic.

Magnetoliposomes loaded with citrate-coated and uncoated nanoparticles have shown similar drug-release kinetics, except for the LF-AMF treated samples. In particular, uncoated magnetic nanoparticle-embedded liposomes under LF-AMF follow a zero-order kinetic, confirming that uncoated NPs have a stronger effect on the lipid bilayer structure with respect to citrate-coated ones.

Generally, K values decrease when passing from Fickian diffusion to “anomalous transport” and zero-order release. Indeed, the rate of release is higher at the beginning, when most of the CF is inside liposomes and diffuses out by concentration gradient. When water mobility is dominant in penetrating the lipid bilayer as a consequence of increased porosity due to temperature increase and

nanoparticle motions under the applied oscillating magnetic field, the rate of release is slower.

Table 4.1. Kinetic parameters obtained fitting CF release curves of magnetoliposomes with equation (4.1).

	Citrate $CoFe_2O_4$ NPs-loaded magnetoliposomes	**Uncoated $CoFe_2O_4$ NPs-loaded magnetoliposomes**
No field		
n	0.57±0.01	0.55±0.01
K	$3.62 \cdot 10^{-3} \pm 0.13 \cdot 10^{-3}$	$4.75 \cdot 10^{-3} \pm 0.15 \cdot 10^{-3}$
Temperature		
n	0.72±0.01	0.76±0.01
K	$7.85 \cdot 10^{-4} \pm 0.52 \cdot 10^{-4}$	$7.02 \cdot 10^{-4} \pm 0.31 \cdot 10^{-4}$
LF-AFM		
n	0.80±0.03	1.01±0.02
K	$3.35 \cdot 10^{-4} \pm 0.68 \cdot 10^{-4}$	$1.58 \cdot 10^{-4} \pm 0.18 \cdot 10^{-4}$

4.1.2 Confocal Laser Scanning microscopy experiments

To further investigate the leakage behaviour, giant unilamellar vesicles (GUVs) labeled with $DiIC_{18}$ and filled with a water soluble fluorophore (Alexa 488-C5-maleimide) have been prepared (see Drug carriers) and studied by means of Confocal Laser Scanning Microscopy (CLSM)[9].

The incorporation of a hydrophilic fluorophore in the vesicle pool allows the direct observation of the variation of fluorescent intensity during time, which is linked to the probe leakage. Moreover, the $DiIC_{18}$ probe was incorporated into GUVs bilayer to monitor the membrane stability during the experiments. GUVs

embedded with Cobalt ferrite NPs and control samples (GUVs without magnetic NPs) have been analyzed by measuring the change in fluorescence intensity of the Alexa dye inside the GUVs in a way to check the vesicle permeability changes under LF-AMF. CLSM experiments with CF-loaded vesicles are not reported because Carboxyfluorescein undergoes strong photobleaching when continuously irradiated with the excitation laser source: i.e., CF does not allow the distinction between the fluorescence intensity decrease due to the photobleaching effect or to the field exposure. Therefore, only Alexa 488-C5-maleimide dye, which has the same excitation and emission wavelengths of CF, was used to fill the vesicles, although its molecular weight is higher.

Time-series scans have been performed before, during and after the application of LF-AMF at the maximum oscillating frequency (5.82 kHz).

Control samples of Alexa-loaded GUVs were scanned under CLSM in absence and presence of LF-AMF, indicating no change in fluorescence intensity during time (time-series in Figure 4.8). Therefore, we can exclude photobleaching of the Alexa fluorescent probe (green in Figure 4.8) and any significant leakage effect due to the field exposure of GUVs without magnetic nanoparticles.

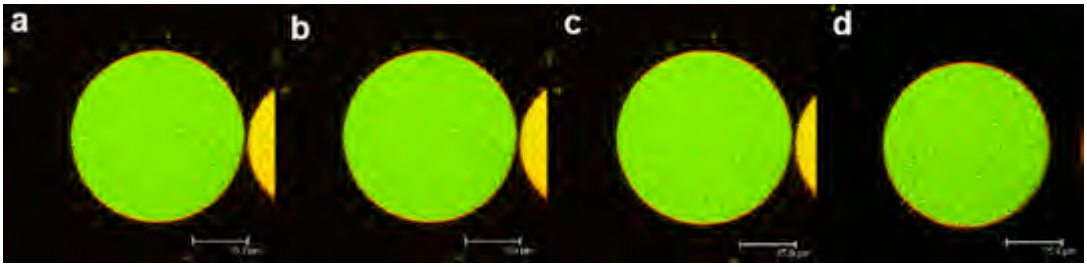

Figure 4.8. CLSM images of Alexa-loaded GUV (control sample) in absence of LF-AMF (a) at time zero and (b) after 30 minutes. Alexa-loaded GUV (c) exposed for 10 minutes to LF-AMF and (d) 10 minutes after the magnetic field application.

On the other hand, some of the Alexa-GUVs loaded with citrate magnetic nanoparticles have shown a strong effect when exposed to LF-AMF, as reported in the time-series pictures in Figure 4.9. In the absence of the field, magnetic GUVs showed no change in fluorescent intensity over the investigated period of time (30 minutes), although the initial fluorescent intensity was strongly lower with respect to the control sample because of the lower concentration of the embedded Alexa dye when nanoparticles were loaded inside the vesicles. In the presence of LF-AMF we have observed a progressive reduction of the fluorescent intensity inside the vesicles during the exposure time, and this trend proceeds even after the field removal, as consequence of an increased Alexa diffusion through the vesicles membrane. The pictures reported in Figure 4.9 show that the lipid bilayer of GUVs labeled with $DiIC_{18}$ (red in Figure 4.9) kept unaltered the membrane integrity, even if a slight reduction of the fluorescent intensity confirms the formation of pore-like structures at the membrane level that promotes Alexa leakage.

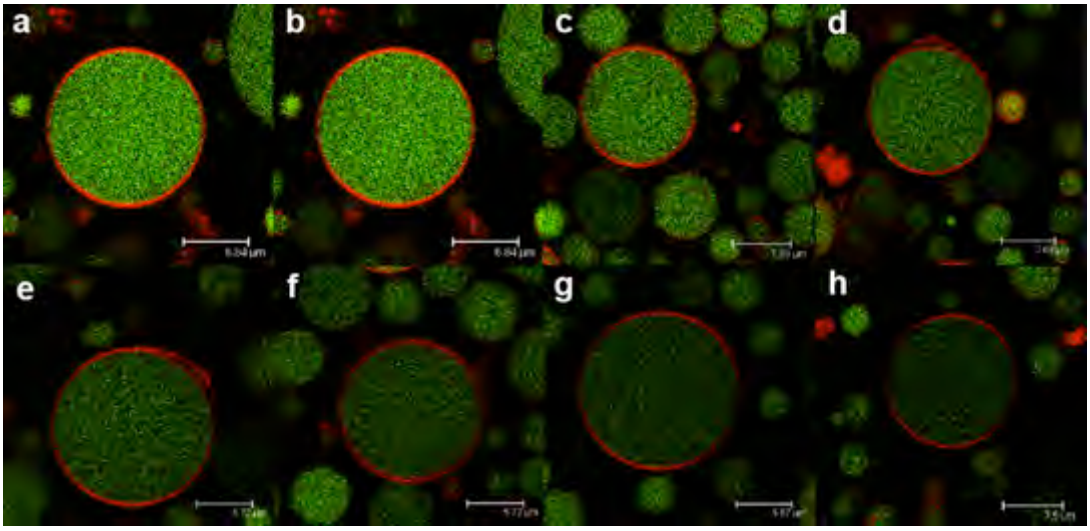

Figure 4.9. CLSM images of Alexa-loaded GUV with citrate magnetic NPs (a) in absence of LF-AMF at time zero and (b) after 30 minutes. Magnetic GUV (c) exposed for 5 minutes and (d) 10 minutes to LF-AMF and (e) 10 minutes after the field application. Magnetic GUV again exposed to LF-

AMF for (f) 5 minutes and (g) 10 minutes and (h) 10 minutes after the last field application.

However, other GUVs from the same samples have shown different behaviour when exposed to the field: some of them strongly decreased the fluorescent intensity, others did not undergo any fluorescent changes. This confirms, as reported in CryoTEM images (see Drug-carriers), that magnetic nanoparticles are not present in all GUVs at the same concentration, so that only the loaded ones have shown Alexa leakage upon LF-AMF exposure. Moreover, GUVs embedded with uncoated and citrate coated NPs have shown a similar leakage behaviour, probably because both nanoparticles (even the uncoated ones) do not form aggregates in sucrose buffer (in fact no precipitate was observed, even after one week). In Figures 4.9 and 4.10 we have reported the best Alexa-release results obtained with GUVs loaded with citrate coated NPs.

The release rates of Alexa dye from untreated and treated magnetic GUVs are shown in Figure 4.10, were the relative fluorescence intensity, calculated as the ratio between the measured fluorescence intensity at time t and the fluorescence intensity of the untreated sample at time zero, has been monitored during time. Magnetic GUVs samples exposed to the field have shown a strong decrease (20-50%) of the fluorescence intensity during the experiments.

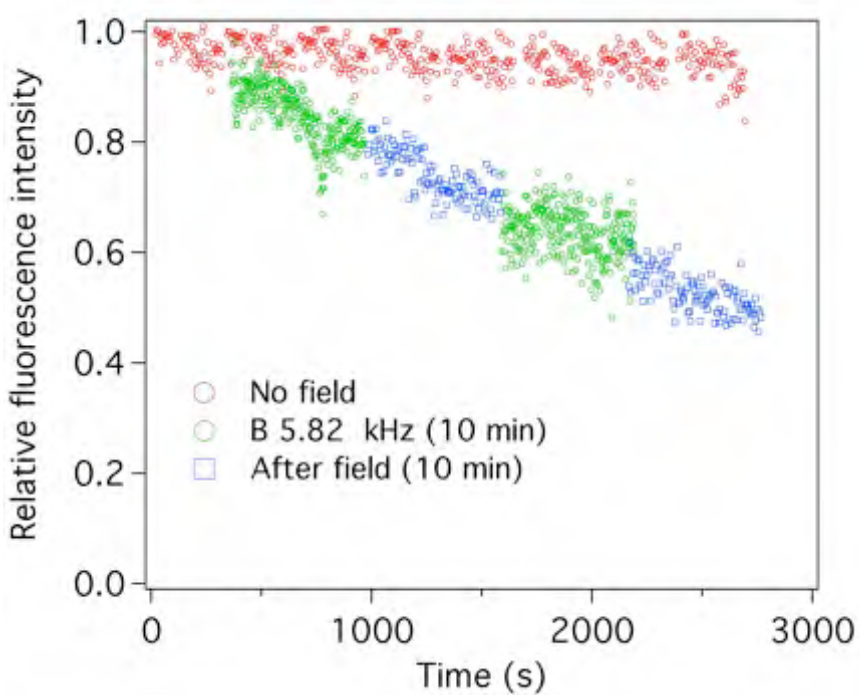

Figure 4.10. Alexa release kinetics from magnetic NPs embedded GUVs before, during and after LF-AMF application.

Therefore, the permeability of GUVs, negligible in absence of LF-AMF, strongly increased after the field exposure. Finally, those experimental results support the assumption that LF-AMF changes GUV permeability in presence of magnetic nanoparticles. However, it is important to highlight that the release rates obtained by CLSM experiments are not comparable with the ones obtained by fluorescence spectroscopy because the systems are different for the vesicles dimensions, the buffers and the fluorescent probes.

4.2 Magnetoliposomes embedded with hydrophobic nanoparticles

The effect of LF-AMF on the stability and release properties of magnetoliposomes loaded with oleic-acid coated Cobalt-ferrite NPs was studied by monitoring the increase of fluorescence emission of CF during time (30 hours). The leakage has been measured as a function of the field frequency (0.2 kHz, 2.84 kHz and 5.82 kHz), the time of exposure (10, 20 and 50 min) to the field and concentration of the magnetic nanoparticles physisorbed on the lipid bilayer of the vesicles.

Magnetoliposomes (sample B in Table 3.7) show no significant increase in their permeability upon LF-AMF exposure for the first 5 hours, in fact during this time the release is not much different with respect to the unexposed sample. However, the CF release from magnetoliposomes shows a sudden increase after 6 hours and reaches high percentage (until 90%) after 20 hours (Figure 4.11 a,b). The blank samples (liposomes without nanoparticles) exposed to LF-AMF at the higher exposure time and field frequency (where the higher release was observed) have also been investigated and compared with magnetic liposomes. The treated blank samples, unlike the treated magnetoliposomes, show no significant release during all the 30 hours of fluorescence monitoring time.

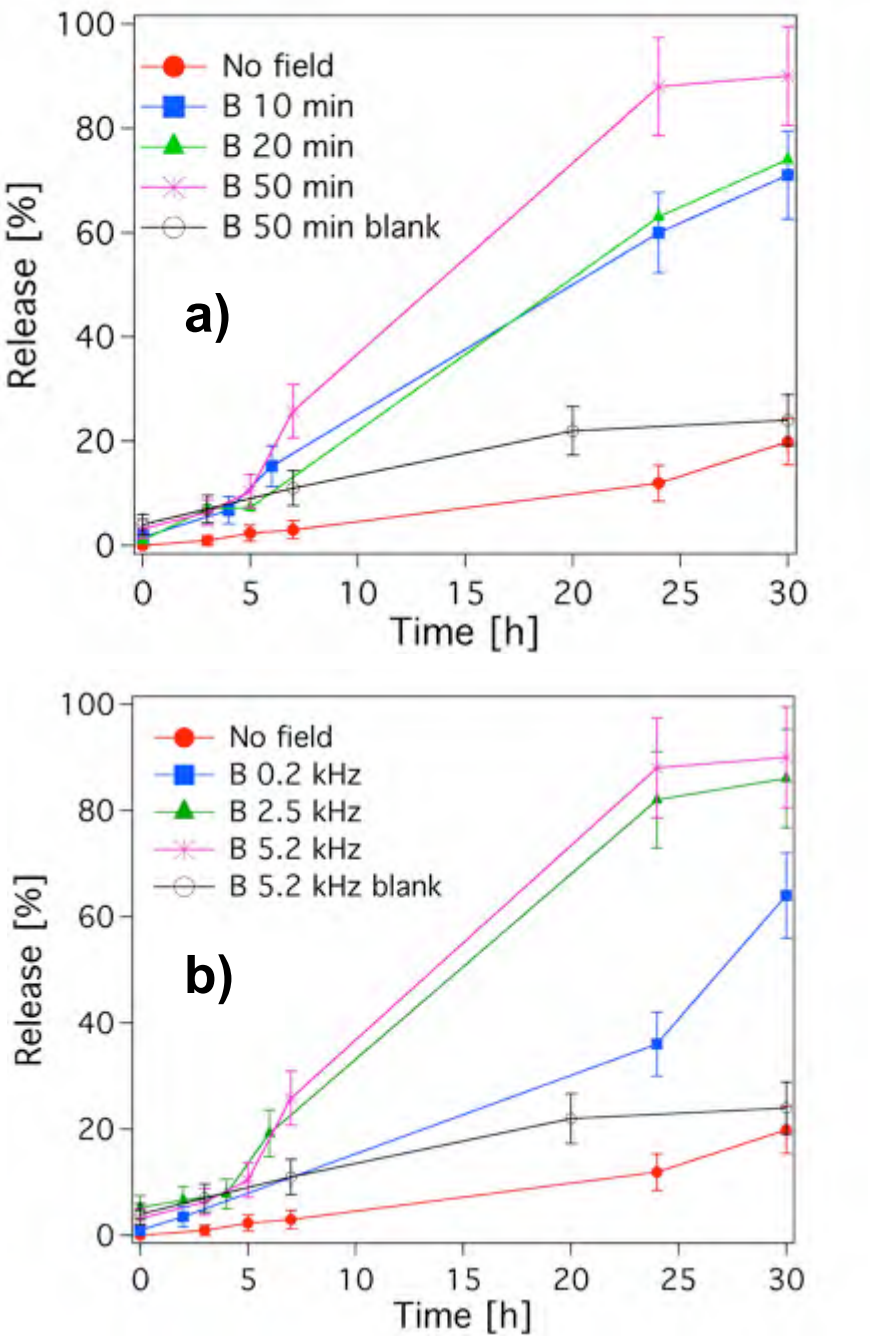

Figure 4.11. Release of CF-loaded magnetoliposomes (sample B in Table 3.7) in the presence of LF-AMF as a function of (a) exposure time at 5.2 kHz and (b) of field frequency for 50 minutes of treatment.

These results indicate that magnetic nanoparticles, entrapped in the lipid bilayer of magnetoliposomes, effectively affect the bilayer permeability subsequently to the LF-AMF exposure as a consequence of their motions due to the applied field frequencies.

The CF release trend of magnetoliposomes reported in Figure 4.11(a,b) suggests a weak perturbation at the lipid bilayer during the first 6 hours, followed by a stronger destabilization of the lipid bilayer, which promotes the sudden CF leakage. The strong increase of CF leakage, until 90% of the total release, can be due to the possible rupture of some vesicles. The results obtained for different exposure time to the LF-AMF are reported in Figure 4.11a and show that field application of 10 or 20 minutes have similar behaviour, while longer field exposure time (50 min) lead to higher release. Figure 4.11b shows the results in function of field frequency, evidencing higher release for frequencies above 2.5 kHz.
During the exposure to the LF-AMF, magnetoliposomes have shown an increase of temperature up to 40°C, due to the coils heat dissipation. Control experiments on magnetoliposomes incubated at the highest temperature produced by the oscillating field for the total exposure time have been performed to take into account the temperature contribution. In Figure 4.12a, CF release experiments on temperature-treated samples (sample B in Table 3.7) are reported. Higher temperatures stronger affect the CF release, however the heating has a lower effect on magnetoliposome permeability compared to the LF-AMF contribution.
The release experiments with magnetoliposomes at different oleic acid-coated $CoFe_2O_4$ nanoparticles concentrations are reported in figure 4.12b. Higher loadings are more effective in the CF release because the presence of high concentrations of magnetic nanoparticles in the lipid bilayer strongly destabilizes the liposomes membrane upon LF-AMF exposure. Nanoparticles oscillations promote the formation of pores at the membrane, favoring the CF leakage through the lipid bilayer.

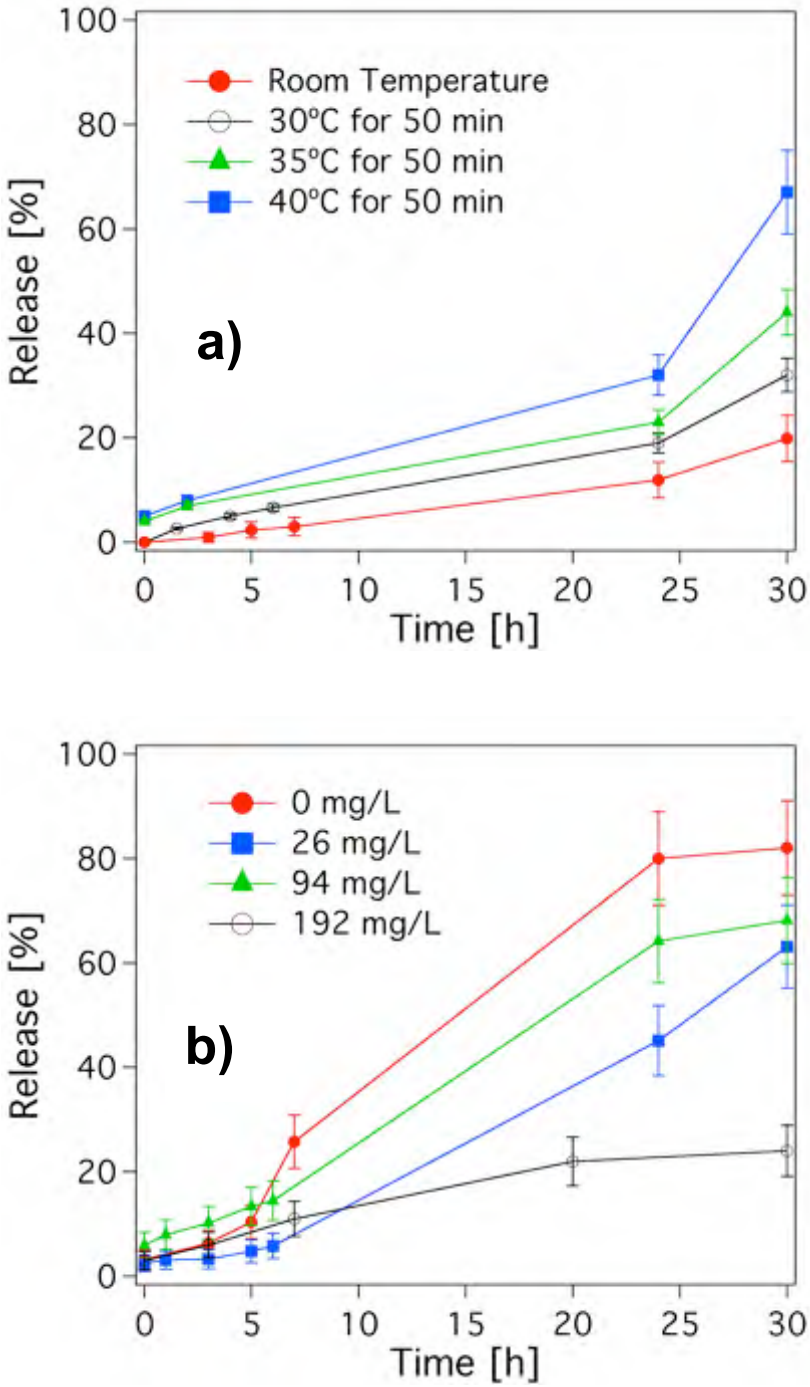

Figure 4.12. (a) Release curves of CF-loaded magnetoliposomes (sample B in Table 3.7) incubated at the temperature indicated in the figure legend. (b) Release curves of CF-loaded magnetoliposomes at different oleic-coated $CoFe_2O_4$ NPs content. These are the samples reported in Table 3.7 where they are labeled as A, B, C, respectively.

CF release results obtained with oleic-coated Cobalt ferrite

nanoparticles entrapped in the lipid bilayer of liposomes have shown some differences with respect to the previous results obtained with naked and citrate-coated cobalt ferrite nanoparticles embedded in the acqueos pool of magnetoliposomes. In Figure 4.13 release curves of magnetoliposomes loaded with oleic acid-coated, citrate-coated and uncoated cobalt ferrite nanoparticles (all prepared at the same concentration of $CoFe_2O_4$ ≈ 200 mg/L) and control liposomes are reported to highlight release differences when they are exposed for 50 minutes to the oscillating field at 5.2 kHz of frequency.

As above mentioned, magnetoliposomes with oleic acid-coated nanoparticles show a very low percentage of CF-release (5%) at the beginning, pointing out no differences with respect to the control sample (liposomes without nanoparticles), and they undergo a sudden increase of leakage only after some hours from LF-AMF exposure. Otherwise, citrate and naked nanoparticles embedded liposomes show a higher initial release (25% and 40% respectively), increasing constantly until 60% of the total leakage after 30 hours. The different release trend of the investigated magnetoliposomes is probably due to the different magnetic nanoparticles location: the lipid bilayer for oleic acid NPs and the aqueous pool of liposomes for hydrophilic NPs. The greater stability of magnetoliposomes with oleic acid-coated NPs during the first 6 hours is related to the presence of hydrophobic NPs within the lipid bilayer, which makes Carboxyfluorescein diffusion through the lipid bilayer slower and more difficult. However, the LF-AMF application causes an initial membrane destabilization, which is followed, about 8 hours later, by the formation of pores at the membrane that promotes the sudden CF leakage. The saturation (90% of the total CF leakage) is quickly reached in less than 30 hours, evidencing the disruption of liposomes during time. Differently, magnetoliposomes loaded with hydrophilic NPs show a stronger initial membrane destabilization

caused by the immediate formation of pores at the lipid bilayer upon the oscillating field exposure, promoting the instantaneous release of CF. However, CF leakage during time is slower and more constant, evidencing no vesicles rupture but only an increased water mobility through the liposome membrane, which is not affected by the presence of nanoparticles entrapped in the lipid bilayer.

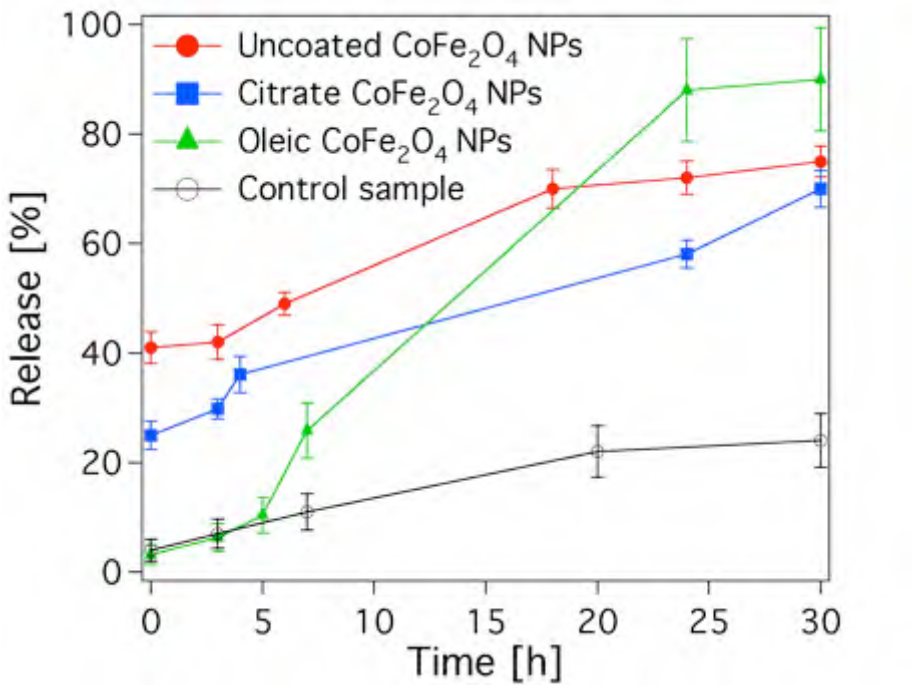

Figure 4.13. Release curves of control sample (liposomes without magnetic nanoparticles) and magnetoliposomes loaded respectively with naked, citrate-coated and oleic acid-coated nanoparticles after LF-AMF exposure at 5.2 kHz for 50 minutes.

4.2.1 Magnetoliposome perturbation: DLS and DSC measurements

Dynamic Light Scattering measurements have been performed on both oleic acid NP-embedded liposomes exposed and unexposed to LF-AMF (B 5.2 kHz for 50 min). Moreover, control experiments on

magnetoliposomes incubated at the highest temperature produced by the oscillating field for the total exposure time have been performed to take into account the temperature contribution. The autocorrelation functions $g_1(\tau)$ of each sample (untreated, LF-AMF exposed and 40°C heated magnetoliposomes) have been monitored every 24 hours during the first three days after the magnetic or thermal treatments. The results, reported in Figure 4.14 show that the normalized autocorrelation functions of treated and untreated solutions coincide, evidencing no perturbation in magnetoliposome population immediately after the field and the thermal exposure.

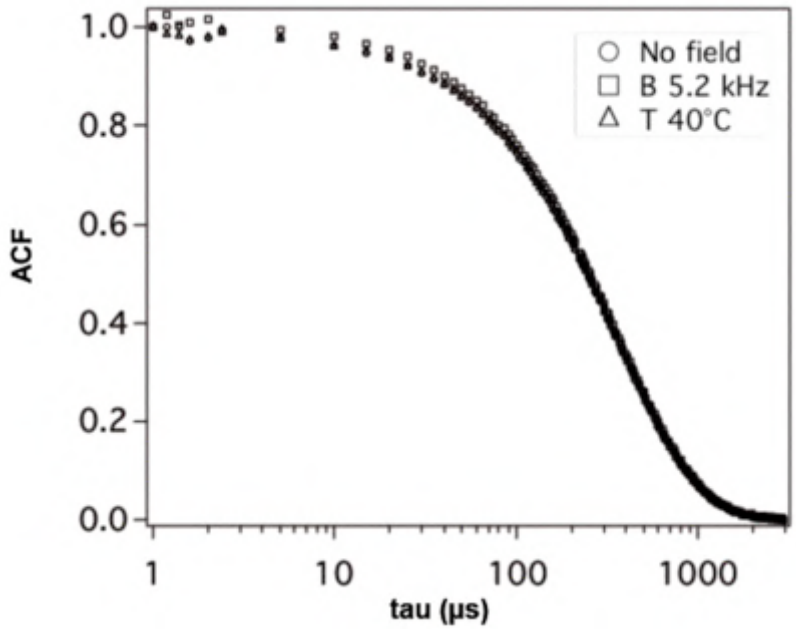

Figure 4.14. DLS normalized autocorrelation functions of fresh magnetoliposome solutions (sample B in Table 3.7): untreated sample at room temperature, sample exposed at 5.2 kHz for 50 min and sample incubated at T=40°C for 50 min.

However the autocorrelation functions of the three investigated samples follow different trends during time: the magnetoliposomes exposed to LF-AMF significantly changes during time, while the untreated and temperature incubated samples undergo only slight changes (Figure 4.15).

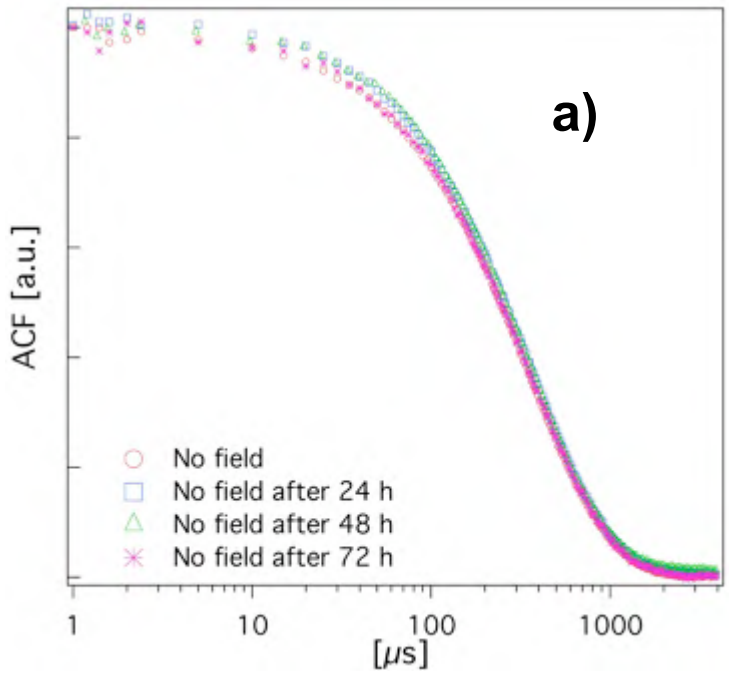
a)
ACF [a.u.]
No field
No field after 24 h
No field after 48 h
No field after 72 h
1
10
100
1000
[μs]

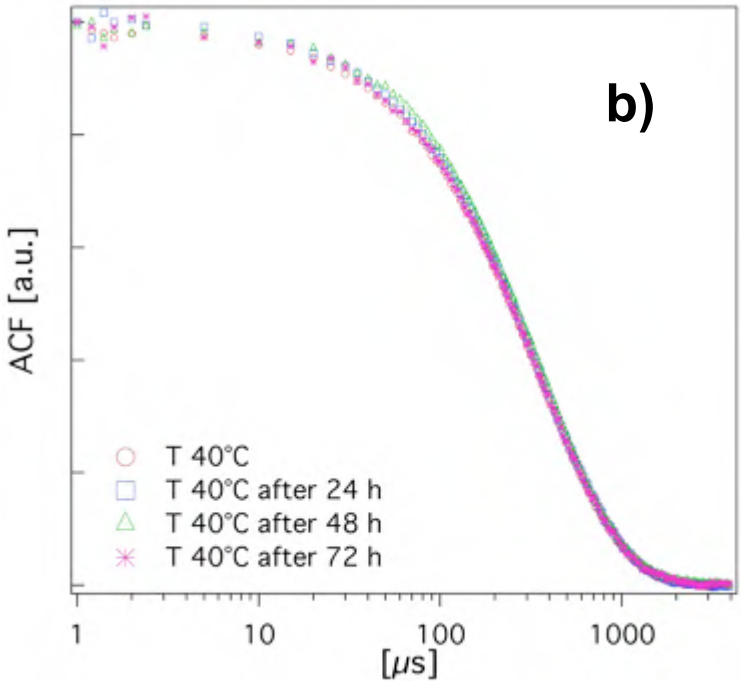
b)
ACF [a.u.]
T 40°C
T 40°C after 24 h
T 40°C after 48 h
T 40°C after 72 h
1
10
100
1000
[μs]

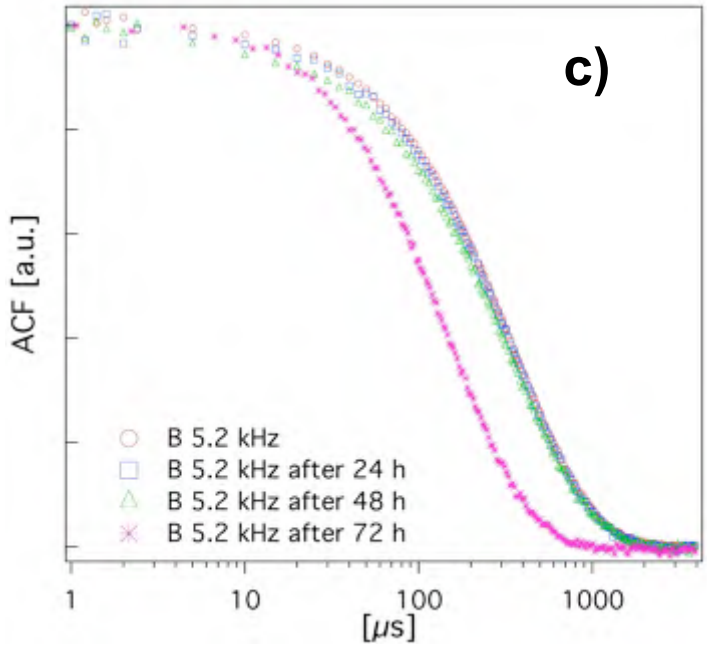

Figure 4.15. DLS normalized autocorrelation functions monitored during time every 24 hours of (a) the untreated sample without field, (b) the sample incubated at T=40°C for 50 min and (c) the sample exposed at 5.2 kHz for 50 min.

These results represent a first evidence of the LF-AMF effect on magnetoliposomes stability, indicating a perturbation of the bilayer structure due to magnetic nanoparticle oscillations, followed by the disruption of some vesicles, which occurs many hours after the field exposure. Moreover, we can state that the temperature weakly affects magnetoliposome stability, as its behaviour is similar to that of the untreated sample.

Differential Scanning Calorimetry measurements have been performed on both liposomes and magnetoliposomes exposed to LF-AMF. The Figure 4.16 shows the thermograms registered on liposomes (a) and magnetoliposomes (b) samples every two hours after the exposure to the magnetic field. The peak, centred around -22°C is due to the transition from the lamellar gel (Lβ) phase to the liquid crystalline (Lα) phase of the PC bilayers. The fact that in the

liposome sample the peak corresponding to this thermal event is narrower than in magnetoliposomes suggests that the presence of the nanoparticles induces a reduction of the cooperativity during the gel/liquid transition of the lipid bilayers. Moreover the application of a magnetic field in the presence of the nanoparticles induces the complete loss of the peak after approximately 8 hours after the treatment, while the bilayer transition doesn't change when the liposome sample is exposed to the field. To highlight this result, the enthalpies of the gel/liquid transition as a function of time for both liposome and magnetoliposome samples are reported in figure 4.16c.
DSC experiments support the CF release results, however it's important to stress that the disappearance of the gel/liquid transition peak does not correspond to the rupture of liposomes, as shown by DLS.

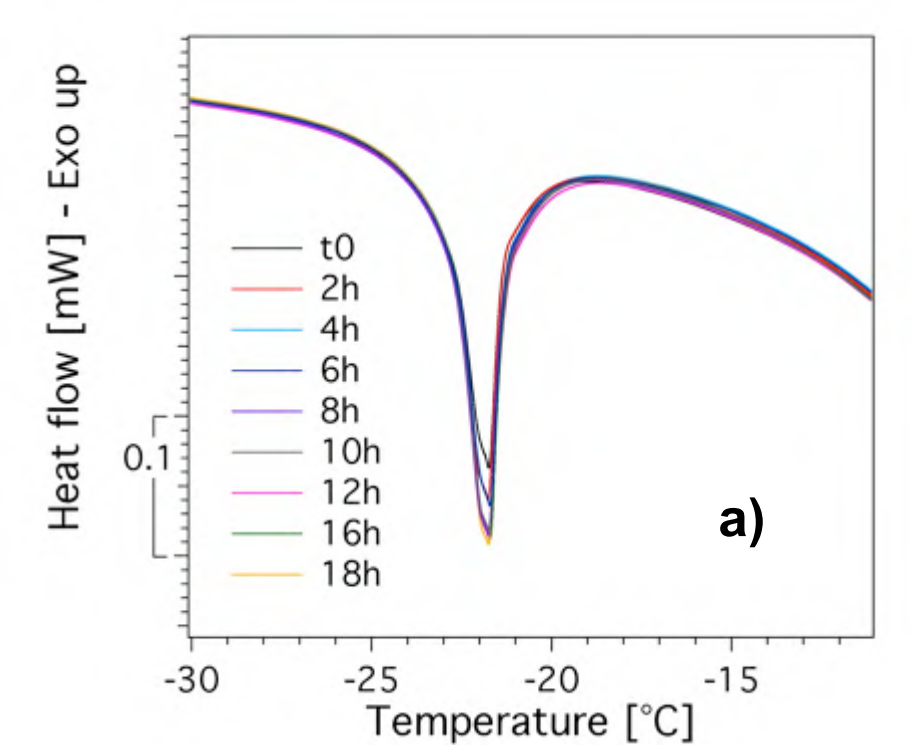

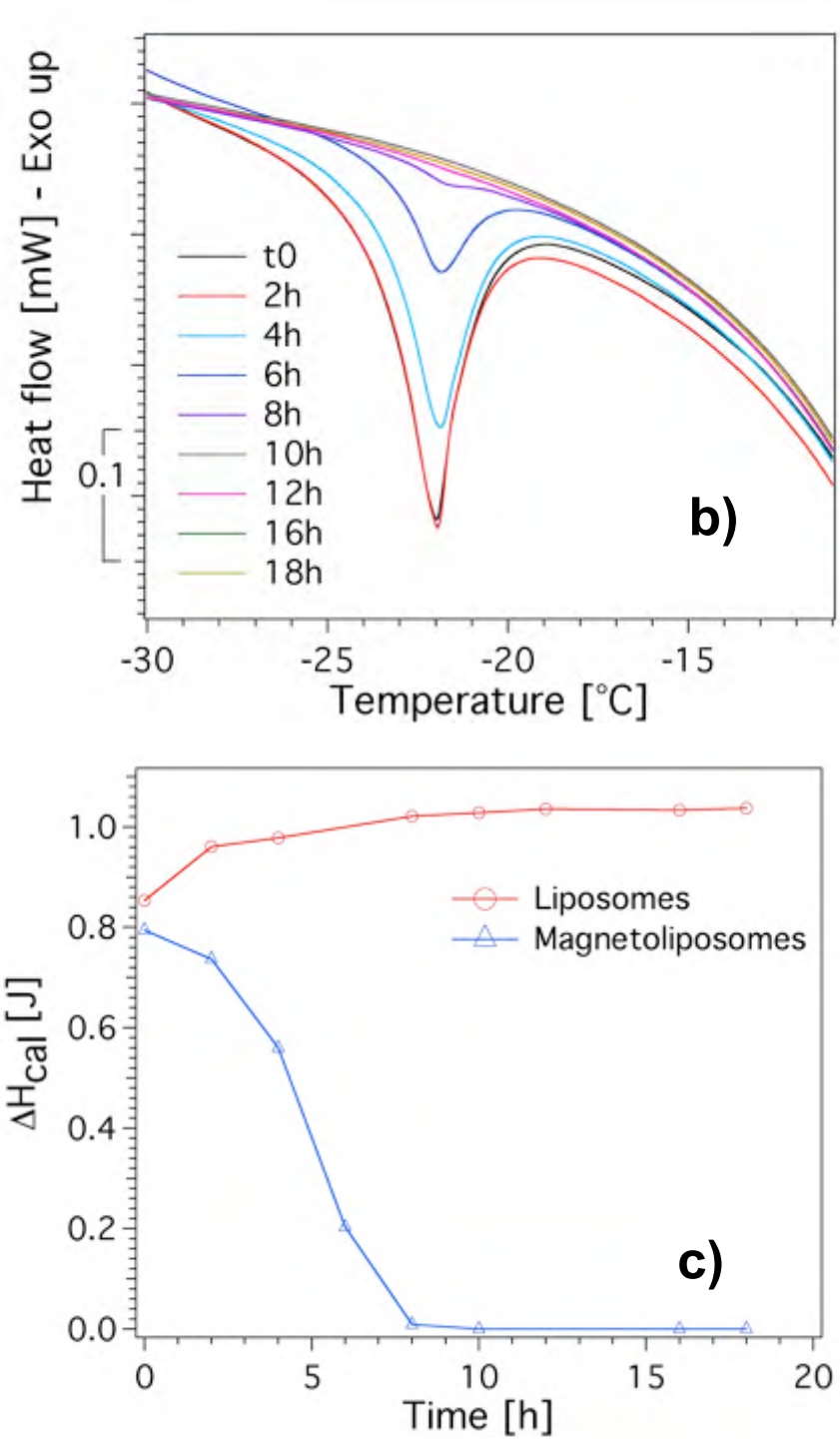

Figure 4.16. DSC heating curves of (a) liposomes and (b) magnetoliposomes (sample D in Table 3.7) exposed to LF-AMF (B 5.2 kHz) for 50 min monitored every two hours during time; (c) enthalpy of gel/liquid transition (ΔH_{cal}) of liposomes and magnetoliposomes exposed to LF-AMF (B 5.2 kHz) for 50 min, monitored every two hours after the treatment.

4.2.2 Drug release kinetics

In order to better understand the mechanism of CF release from magnetoliposomes with magnetic nanoparticles physisorbed on the lipid bilayer, CF fluorescence intensity has been monitored during 1200 minutes. CF release has been investigated for LF-AMF treated and untreated magnetoliposomes and, for the sake of comparison, in heated samples. The experimental kinetic curves and the correspondent fittings obtained from Ritger and Peppas equation are reported in Figure 4.17.

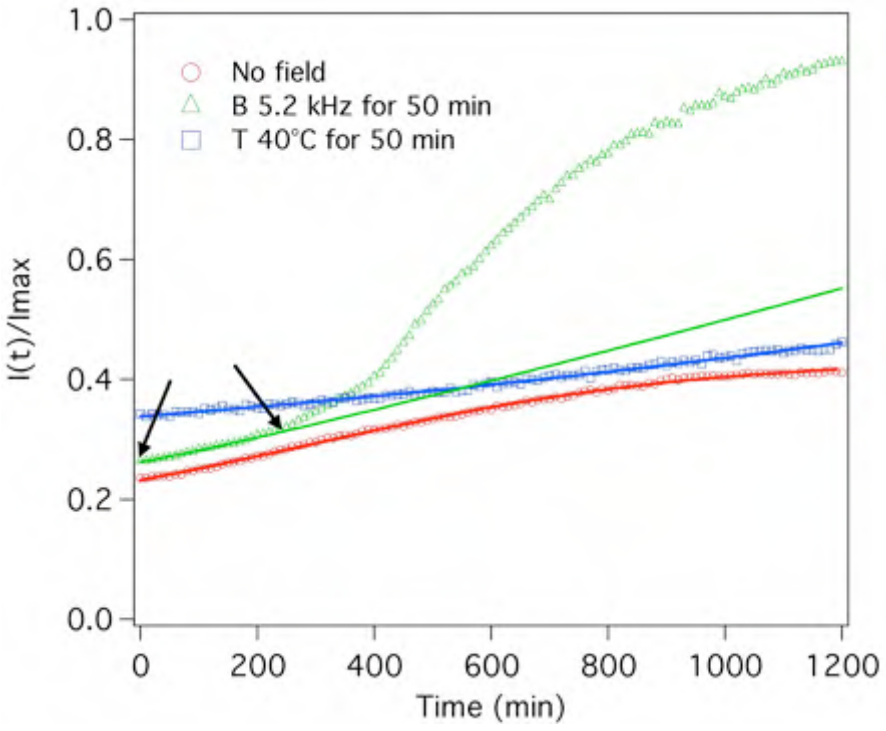

Figure 4.17 Release curves of oleic acid-coated $CoFe_2O_4$ NPs embedded-magnetoliposomes (sample B Table 3.7) in time drive mode. (○) Untreated samples, (□) incubated at 40°C for 50 minutes, (△) samples exposed to LF-AFM for 50 minutes at a frequency of 5.2 kHz, where the arrows indicate the experimental data considered in the curve fitting. Solid curves are the best fitting obtained by means of equation (4.1).

Kinetics parameters obtained from the analysis of the curves with

equation (4.1) are shown in Table 4.2. Untreated samples are well fitted for n equal to 0.69±0.02 indicating that the dominant drug release mechanism is the combination of Fickian diffusion and membrane destabilization due to the presence of hydrophobic NPs within the lipid bilayer. The fitting curves of magnetoliposomes incubated at 40°C gives n=1.16±0.03 typical of a zero order kinetic, indicating membrane erosion or pores formation at the lipid bilayer, however the rate of release is low. LF-AMF treated samples show a particular kinetic profile that indicates the presence of two different release mechanisms: an initial membrane destabilization during the first 230 minutes (corresponding to the lag time, l) followed by an exponential burst release with a sigmoid profile. In this case only the first 230 minutes of CF release data were fitted by equation (4.1), evidencing a zero order kinetic (n= 1.10±0.07) characterized by a low rate of release ($K=1.20\cdot10^{-4}\pm0.44\cdot10^{-4}$). The next burst release, which leads to the complete CF leakage from LF-AMF treated samples, confirms that nanoparticle motions induce, after the initial slow membrane erosion, the formation of large pores at the membrane followed by the vesicles rupture.

K values generally decrease in passing from Fickian diffusion to “anomalous transport” and zero-order release. This behaviour is followed also this time by the investigated untreated and treated samples, indicating a higher rate of release at the beginning, when most of the CF is inside magnetoliposomes and diffuses out by concentration gradient.

For LF-AMF exposed samples the presence of a long lag time, during which the release is very low, before the next burst release of CF occurred, makes this system a good candidate for controlled drug delivery. In fact the lag time would allow magnetoliposomes to reach the target site, avoiding unspecific drug loss during the transport, and the drug release would occur only at the target site.

Table 4.2. Kinetic parameters obtained fitting CF release curves of magnetoliposomes with equation (4.1).

No treatments	
n	0.69±0.02
K	$1.65 \cdot 10^{-3} \pm 0.21 \cdot 10^{-3}$
Temperature	
n	1.16±0.03
K	$3.02 \cdot 10^{-5} \pm 0.63 \cdot 10^{-5}$
LF-AFM	From 0 to 230 minutes
n	1.10±0.07
K	$1.20 \cdot 10^{-4} \pm 0.44 \cdot 10^{-4}$

4.3 Confocal Laser Scanning Microscopy: GUVs embedded with MP@SiO_2(RITC)

The leakage behaviour from Giant Unilamellar Vesicles was studied by means of CLSM, loading GUVs with the water-soluble fluorophore Alexa 488-C5-maleimide. Magnetic GUVs in the presence of MP@SiO_2(RITC) and control samples (GUVs without magnetic particles) were analyzed by measuring the change in fluorescence intensity of the Alexa dye inside the GUVs in a way to check the vesicle permeability changes under LF-AMF. Time-series scans were carried out before, during (15 min) and after (15 min) the LF-AMF application at 200 Hz of oscillating field frequency.

Experiments performed on control samples, Alexa-loaded GUVs (without microparticles) have indicated no changes in the fluorescence intensity during time. Therefore, we can exclude any leakage mechanisms due to the LF-AMF exposure of non-magnetic GUVs and any photobleaching effects of the Alexa dye.

On the other hand, Alexa-loaded GUVs in presence of MP@SiO_2(RITC) have shown a strong release of Alexa due to the LF-AMF exposure, as reported in the time-series pictures in Figure 4.18. During the LF-AMF application we observed a progressive reduction of the fluorescent intensity of Alexa inside the vesicles and this trend proceeded even after the field removal, as consequence of an increased Alexa diffusion through the vesicles membrane. It is interesting to note that, even if the distribution of MP@SiO_2(RITC) onto the membrane is not homogeneous, the Alexa leakage from the GUVs is uniform, evidencing no preferential paths in the membrane. However, as shown in Figure 4.19, the rate of release is not constant during time, but indicates the presence of different processes of

erosion and pore formation at the membrane during the release monitoring.

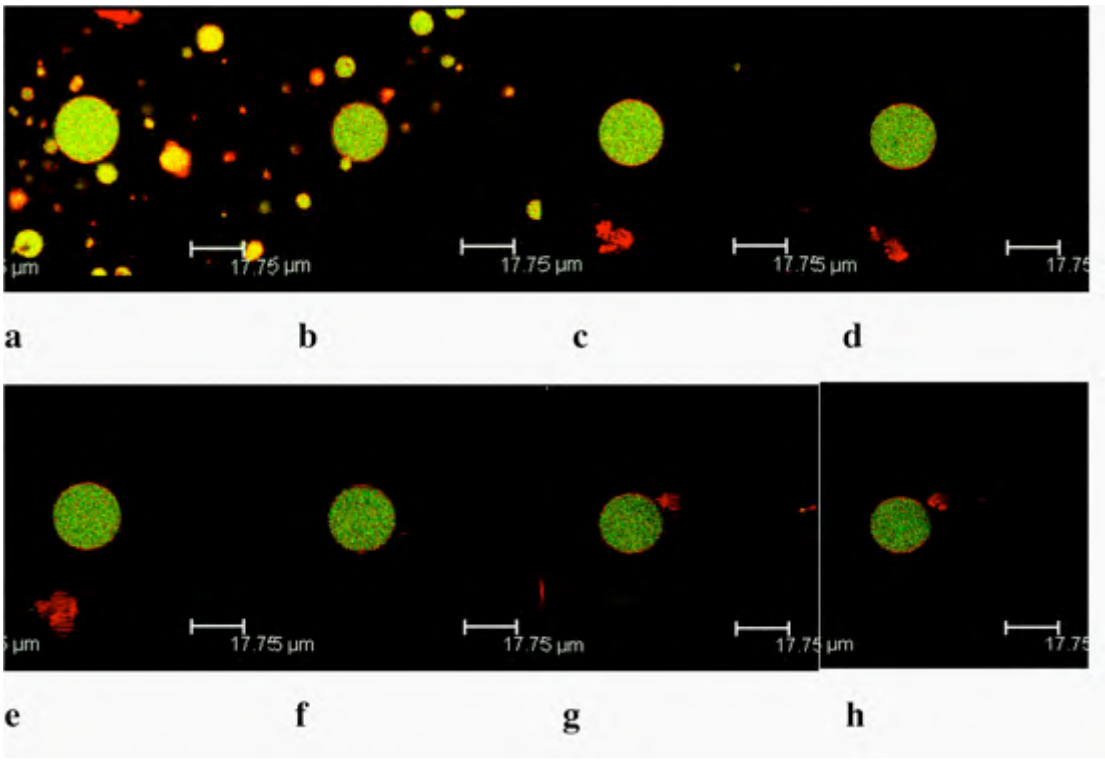

Figure 4.18**.** CLSM images of Alexa-loaded magnetic GUVs (Alexa in green, MP@SiO_2(RITC) in red). Magnetic GUV (a) in absence of AMF at time zero, (b) exposed for 8 minutes and (c) 15 minutes to 200 Hz-AMF and (d) 15 minutes after the field application. Magnetic GUV again exposed to 200 Hz-AMF for (e) 8 minutes and (f) 15 minutes and (g) 15 minutes and 1.5 hour after the last field application.

Figure 4.19 shown the release kinetics of Alexa dye from magnetic and non-magnetic GUVs, where the relative fluorescence intensity, calculated as the ratio between the measured fluorescence intensity at time t and the fluorescence intensity of the untreated sample at time zero, were monitored during time. Magnetic GUV samples exposed to the field have shown a strong decrease (around 50%) of the fluorescence intensity during the experiments. Therefore, the permeability of GUVs, negligible in absence of LF-AMF, strongly increased after the field exposure. These results, similar to what we have previously reported for magnetoliposomes loaded with uncoated

and citrate coated nanoparticles, indicate that the application of LF-AMF induces an alteration of the lipid bilayer structure (promoting the formation of pores) that enhances the Alexa-release, without the rupture of the vesicles.

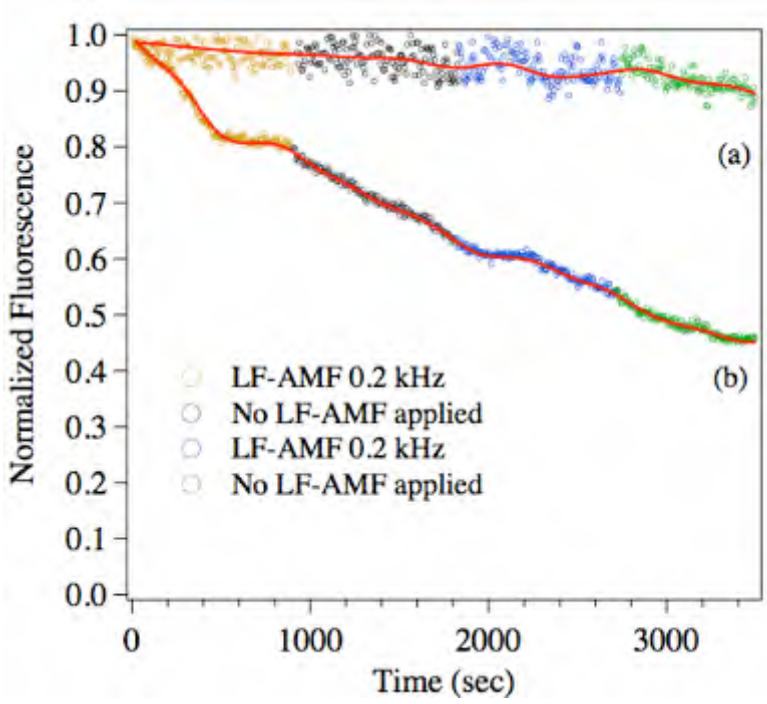

Figure 4.19. Alexa release kinetics from GUVs in absence (a) and presence (b) of MP@SiO_2(RITC) during and after LF-AMF applications.

In order to better understand the mechanism involved in the Alexa leakage, the release kinetic, reported as decrease of the normalized fluorescence intensity of the dye inside GUVs during time, was studied by Ritger and Peppas equation written as:

$$\frac{(I(0)-I(t))}{I(\infty)} = Kt^n \qquad (4.3)$$

where [I(0)-I(t)]/I(∞) is the drug fraction release at time t, K is the kinetic constant and n is the diffusion exponent. The experimental curve and the corresponding fitting obtained with magnetic GUVs exposed to the LF-AMF are reported in Figure 4.20.

The curve is well fitted by equation (4.3) for n equal to 0.67±0.01, indicating an "anomalous transport" mechanism of release, that is the combination of Fickian diffusion and membrane perturbation of GUV. A kinetic constant, K, of $2.37 \cdot 10^{-3} \pm 0.31 \cdot 10^{-3}$ indicates a high rate of release.

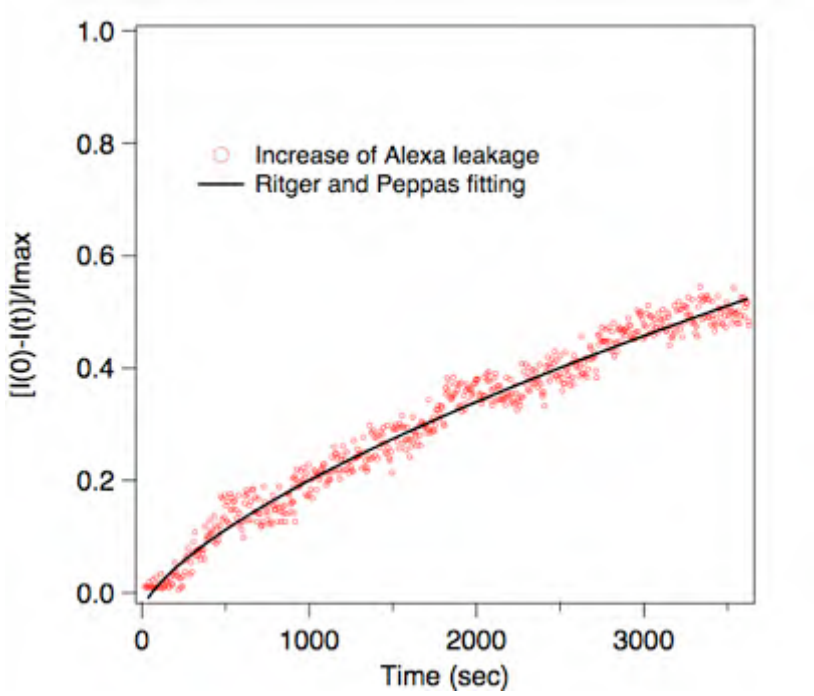

Figure 4.20. Alexa release kinetic from GUVs decorated with MP@SiO_2(RITC) exposed to LF-AMF. The solid curve is the fitting obtained by means of equation (4.3).

4.4 References

(1) Arifin, D. Y.; Lee, L. Y.; Wang, C.-H. *Advanced Drug Delivery Reviews* **2006**, *58*, 1274-1325.

(2) Serra, J.; Doménech, J.; Peppas, N. A. *Biomaterials* **2006**, *27*, 5440-5451.

(3) Ritger, P. L.; A., P. N. *Journal of Controlled Release* **1987**, *5*, 23-36.

(4) Velasco, M. V.; Ford, J. L.; Rowe, P.; Rajabi-Siahboomi, A. R. *Journal of Controlled Release* **1999**, *57*, 75-85.

(5) Sadeghi, F.; Ford, J. L.; Rubinstein, M. H.; Rajabi-Siahboomi, A. R. *Drug Development and Industrial Pharmacy* **2001**, *27*, 419-430.

(6) Sadeghi, F.; Ford, J. L.; Rubinstein, M. H.; Rajabi-Siahboomi, A. R. *Drug Development and Industrial Pharmacy* **2000**, *26*, 651-660.

(7) Ford, J. L.; Mitchell, K.; Sawh, D.; Ramdour, S.; Armstrong, D. J.; Elliott, P. N. C.; Rostron, C.; Hogan, J. E. *International Journal of Pharmaceutics* **1991**, *71*, 213-221.

(8) Ford, J. L.; Mitchell, K.; Rowe, P.; Armstrong, D. J.; Elliott, P. N. C.; Rostron, C.; Hogan, J. E. *International Journal of Pharmaceutics* **1991**, *71*, 95-104.

(9) Ambroggio, E. E.; Separovic, F.; Bowie, J. H.; Fidelio, G. D.; Bagatolli, L. A. *Biophysical Journal* **2005**, *89*, 1874-1881.

5 - Conclusions

5.1 Final remarks

In this work innovative transport vectors for drug delivery based on liposomes were employed and their drug release behaviour was studied.

The ability of liposomes to target a particular tissue or cell, and the control over the release kinetics was enhanced by introducing magnetic nanoparticles (Cobalt ferrite, $CoFe_2O_4$ NPs) inside lipid vesicles (in the liposome pool or in the lipid bilayer depending on nanoparticle properties). The presence of magnetic nanoparticles allows targeting drugs to a specific location using an external magnetic force and allows enhancing the drug leakage by applying an alternating magnetic field (AMF)[1,2]. In this thesis a low-frequency alternating magnetic field (LF-AMF), 0.1-6 kHz, was used to study drug release from magnetoliposomes in order to minimize the temperature contribution. The enhancement of magnetoliposomes' permeability was measured as the self-quenching decrease of the fluorescent hydrophilic molecule (Carboxyfluorescein, CF) entrapped in the aqueous pool of liposomes.

Hydrophilic and hydrophobic Cobalt ferrite NPs were prepared by co-precipitation technique and characterized by SAXS (Small Angle X-Rays Scateering), DLS (Dynamic Light Scattering) and TEM (Transmission Electron Microscopy) (see Drug-carriers).

Hydrophilic nanoparticles, uncoated (positively and negatively charged) and citrate-coated were successfully embedded in the aqueous pool of liposomes, while the hydrophobic ones, coated with oleic acid, were entrapped in the lipid bilayer of liposomes. Magnetoliposomes were prepared by extrusion method and characterized by DLS, moreover giant unilamellar vesicles (GUVs) embedded with hydrophilic Cobalt ferrite nanoparticles and magnetic-fluorescent nanoparticles (MP@SiO_2(RITC)) were prepared by electroformation and analyzed by Confocal Laser Scanning Microscopy (CLSM) (see Drug-carriers).

All magnetoliposome samples have shown an effective response to LF-AMF exposure in terms of CF release. The release kinetics were monitored during time after the magnetic field application and the drug release kinetics were analyzed by Ritger and Peppas equation in order to understand the drug transport mechanism. The results have indicated that, in presence of LF-AMF, both nanoparticles'oscillations and hyperthermic effect due to the magnetic field anisotropy of the magnet effectively alter the bilayer structure promoting CF release. These results were also confirmed by CLSM experiments, which have shown a progressive leakage of Alexa 488 fluorescent dye, loaded inside magnetic GUVs, during the application of LF-AMF as consequence of the formation of pores at the lipid bilayer.

5.1.1 Liposomes loaded with hydrophilic Cobalt Ferrite nanoparticles

In this work two types of hydrophilic Cobalt ferrite NPs were prepared: uncoated and citrate-coated NPs. Concerning the uncoated ones, positively and negatively charged NPs were synthesized, and, in the case of negatively charged Nps, both small NPs (spheres of about 6 nm of radius) and large NPs (characterized by a representative

population of spheres of about 23 nm and a minor population of about 8 nm in radius) were prepared. All these magnetic samples were successfully embedded in the aqueous pool of liposomes, however their loading and their encapsulation efficiency were quite low (see Drug carriers Table 3.5). Furthermore, the stability of magnetoliposomes was strongly affected by the presence of uncoated NPs, as shown by the appearance of a black precipitate after few days. The precipitation, due to the aggregation of nanoparticles is a limit to biomedical applications. For this reason the nanoparticles have been stabilized with a citrate coating.

The stability and the loading of citrate-coated Cobalt ferrite NPs embedded in liposomes were optimized with respect to the uncoated ones (see Drug carriers Table 3.6).

Both magnetoliposome samples (loaded with uncoated and citrate-coated NPs) have shown promising release results upon LF-AMF exposure, indicating higher CF leakage for long field exposure, high field frequency, high Cobalt ferrite NPs concentration, larger and negatively charged embedded NPs. A comparison between the release results obtained with magnetoliposomes embedded with the same concentration of negative-uncoated and citrate-coated NPs have shown that the last ones, although the magnetic properties were the same, have a slower release of CF during time. This different behaviour can be explained by taking into account a higher electrostatic interaction of uncoated NPs with the lipid bilayer of liposomes and their tendency to form larger aggregates; both the effects lead to the formation of larger pores at the liposome membrane during the LF-AMF application. Since the citrate coating of nanoparticles has induced no change in magnetic properties, the presence of an anisotropic magnetic field, as in the case of our homemade apparatus, causes the magnetic nanoparticle oscillations in opposite directions during the alternating magnetic field cycles. Moreover, AC-susceptibility measurements performed on

magnetoliposmes (see Release experiments) have indicated that local hyperthermal effects are operative at the applied field frequencies. Drug release kinetics of both magnetoliposome samples exposed to LF-AMF, analyzed by Ritger and Peppas equation, showed a “zero order kinetic” and an “anomalous transport” mechanism respectively for uncoated and citrate-coated NPs evidencing in both cases a strong membrane perturbation. Finally CLSM images acquisition of magnetic GUVs labeled with $DiIC_{18}$ and filled with Alexa 488 fluorescent dyes during the magnetic field exposure have confirmed the results previously discussed: Alexa diffuses out through the vesicle membrane as consequence of the formation of pore-like structures at the lipid bilayer without disruption of the lipid membrane. These results indicate that both the hyperthermic effect and nanoparticles’ oscillations in the presence of LF-AMF effectively alter the lipid bilayer structure promoting CF release.

5.1.2 Liposomes loaded with hydrophobic Cobalt Ferrite nanoparticles

Hydrophobic Cobalt ferrite NPs coated with a shell of oleic acid (spheres with a core-shell structure of about 10 nm of radius) were synthesized and successfully entrapped on the lipid bilayer of liposomes.

SAXS characterization of magnetoliposomes has indicated a physisorption of aggregates of magnetic NPs onto the lipid bilayer of liposomes. Magnetoliposome perturbation due to the presence of Cobalt ferrite NPs upon LF-AMF exposure has been investigated by DLS and DSC measurements. DLS, DSC and CF release kinetics of magnetic field treated samples suggest that nanoparticles’ oscillations in the presence of LF-AMF effectively alter the bilayer structure promoting a initial weak release of CF during the first

hours, followed by a stronger destabilization of the lipid membrane due to the formation of larger pores and to the rupture of some vesicles approximately 8-10 hours after the LF-AMF application. Also in this case, magnetoliposome response to the oscillating magnetic field is effective and CF leakage is higher for long LF-AMF exposure time, high field frequency and high Cobalt ferrite NP concentration. Drug release kinetics confirmed the presence of an equilibration time, called "lag period", during which the release is very low before the effective burst leakage occurs. The presence of a long "lag period" makes this system a good candidate for controlled drug delivery as the magnetoliposmes could reach the targeting site without unspecific drug loss during the transport.

5.1.3 Giant unilamellar vesicles with MP@SiO_2(RITC)

Magnetic and fluorescent giant unilamellar vesicles (GUVs) in the presence of MP@SiO_2(RITC) were successfully prepared evidencing a no homogeneous physisorption of nanoparticles on the membrane of the vesicles. The preparation of these GUVs open the opportunity for the real observation of membrane perturbations due to an external *stimulus*[3,4] and the possibility to gain understanding of drug release mechanism.

The effect of the LF-AMF on the release properties and GUVs permeability was investigated by acquisition of CLSM images during time, evidencing a progressive reduction of the Alexa fluorescent intensity inside the vesicles. As in the previous cases, the experimental results have indicated an increase of Alexa leakage through the vesicles membrane, as a consequence of the formation of pores induced by the magnetic particles' oscillations during the LF-

AMF exposure. Drug release kinetics, analyzed by Ritger and Peppas equation, have shown an “anomalous transport” mechanism.

5.2 References

(1) Laurent, S.; Forge, D.; Port, M.; Roch, A.; Robic, C.; Elst, L. V.; Muller, R. N. *Chemical Reviews* **2008**, *108*, 2064-2110.
(2) Lesieur, S.; Grabielle-Madelmont, C.; Menager, C.; Cabuil, V.; Dadhi, D.; Pierrot, P.; Edwards, K. *J. Am. Chem. Soc.* **2003**, *125*, 5266-5267.
(3) Tamba, Y.; Yamazaki, M. *Biochemistry* **2005**, *44*, 15823-15833.
(4) Menager, C.; Guemghar, D.; Perzynski, R.; Lesieur, S.; Cabuil, V. *Langmuir* **2008**, *24*, 4968-4974.

List of publications

- *"Magnetoliposomes for controlled drug release in the presence of low-frequency magnetic field."* **S. Nappini,** F. Baldelli Bombelli, M. Bonini, B. Nordèn, P. Baglioni, *Soft Matter,* **2010,** 6, 154.

In press at *Soft Matter:*

- *"Controlled drug release under a low-frequency magnetic field: effect of the citrate coating on the magnetoliposome stability."* **S. Nappini,** M. Bonini, F. Baldelli Bombelli, F. Pineider, C. Sangregorio, B. Nordèn, P. Baglioni. DOI: 10.1039/C0SM00789G.

Submitted to *Soft Matter*:

- *"Magnetic nanoparticles entrapped in lipid bilayers of liposomes and their effect on drug release in the presence of a low-frequency alternating magnetic field."* **S. Nappini,** M. Bonini, F. Ridi, B. Nordèn, P. Baglioni.

Submitted to *Journal of Physical Chemistry Letters*:

- *"Magnetically triggered release from giant unilamellar vesicles: visualization by means of confocal microscopy."* **S. Nappini,** T. Al Kayal, D. Berti, B. Nordèn, P. Baglioni.

Ringraziamenti

Innanzitutto desidero ringraziare il prof. Piero Baglioni per avermi dato l'opportunità di imparare nuovi concetti e di lavorare in un nuovo "mondo", stimolando il mio interesse verso tutto ciò che ha contribuito alla realizzazione di questa Tesi.
Voglio ringraziare tutti coloro che hanno dato il loro prezioso contributo e che mi sono stati vicino durante questi tre anni di dottorato. In questo gruppo ho conosciuto persone eccezionali con cui ho trascorso tre anni intensi e piacevoli, grazie alle quali le giornate sono passate sempre in allegria.
Ringrazio Francesca Baldelli per avermi aiutato all'inizio di questo percorso gettando le basi sulle quali ho poi costruito tutto e per avermi stimolato a migliorare e a considerare ogni cosa con senso critico.
Un ringraziamento speciale va a Massimo Bonini perché da quando è arrivato tutto è diventato più semplice, con i suoi preziosi consigli è riuscito a risolvere mille problemi e ad insegnarmi ogni volta qualcosa di nuovo.
Un grazie a: Francesca Ridi per l'aiuto alla DSC, Debora Berti per i consigli sulla preparazione delle vescicole, Francesco Rugi per le analisi ICP-AES, Francesco Pineider e Claudio Sangregorio per le misure magnetiche allo SQUID.
Un grazie particolare va ai miei due compagni di stanza, che insieme hanno formato una coppia formidabile: a Nicola, un amico con cui ho percorso anni di scuola e università, e che è diventato ormai una presenza costante di cui è difficile fare a meno; a Marco che, anche se

ha occupato la scrivania solo per brevi periodi, mi ha fatto spesso riflettere su molti punti.
Come non poter ringraziare Tamer per avermi fatto sorridere anche quando non ne avevo voglia, la Chiara, il mio braccio destro, per avermi appoggiato in tutte le mie "lotte", la Silvia Milani per averci messo tutti in riga; Martina, Costanza, Mariella e Francesca Bellissima per le pause tè del pomeriggio e le chiacchiere.
Ringrazio inoltre tutti i compagni di questo "viaggio": Giacomo, Michele, Giovanna, Luca, Irene e poi Filippo, Marcia, Lorenza, Lorenzo, Laura, Emiliano, Moira ed anche Ema, Filippo e Manola, indispensabili e sempre presenti.
Un grazie agli amici di sempre con cui ho superato mille difficoltà e che mi hanno saputo dare consigli preziosi, soprattutto Vale, Silvia, Elisa, Alessandra, Andrea e Lisa.
Infine ringrazio i miei genitori che mi hanno sostenuto durante tutto il mio percorso di studi; è a loro che dedico questa Tesi.